Synthesis and Characterization of Ferroelectric Nanomaterials

Dissertation

In partial fulfillment of the requirements
for the academic degree of

Doctor rerum naturalium
(Dr.rer.nat.)

Submitted to

The Faculty of Mathematics and Natural Sciences
Dresden University of Technology

By

M.Sc. Hongchu Du
Born on Oct. 16, 1976 in Xihua (China)

Approved by:	Prof. Dr. Stefan Kaskel Prof. Dr. Michael Ruck Prof. Dr. Stefan Ebbinghaus

Submitted on: January 11, 2008
Date of examination: July 2, 2008

This dissertation is dedicated to my mother Mrs. Bang Li, my father Mr. Jingzhang Du, my brother Hongyi, my sister Ronghua and my beloved fiancée Kai.

This dissertation is also dedicated to the memory of my grandfather Mr. Bingyao Du.

Acknowledgement

This dissertation was carried out at the Technische Universität Dresden from October 2004 to September 2007. It is difficult to list all the people who have helped me directly and indirectly in this dissertation. I therefore apologize in advance for anyone I have not mentioned here.

First, I would especially like to express my sincere and deepest thanks to my supervisor Prof. Dr. Stefan Kaskel, for directing me to the so interesting nanoworld and steering me to the field of ferroelectric nanomaterials. His inspiring guidance, profound knowledge, stimulating suggestions, and constant encouragement are the most important help to me in all the time of my studies, without which it would not have been possible for me to complete this dissertation.

I am also very grateful to all the members of the dissertation defense committee and the reviewers: Prof. Dr. Manfred Stamm, Prof. Dr. Alexander Eychmüller, Prof. Dr. Michael Ruck, Prof. Dr. Hubert Langbein and Prof. Dr. Stefan Ebbinghaus.

Many thanks to all the close scientific collaborators and colleagues:

Ms. Ellen Kern, Dipl. Hannelore Dallmann and Ms. Inge Schubert for their help in SEM, TG/DSC, and FTIR measurements.

Dr. Sebastian Wohlrab for his help and discussions during the two years collaborations.

Dr. Holger Althues for his help and discussions on the polymerization.

Dr. Yufang Zhu, Dr. Krawiec Piotr, Dipl. Emanuel Kockrick, Dipl. Christian Schrage, Dipl. Robert Frind, Mrs. Heidi Fröde and the whole AK Kaskel and AK Ruck for the nice time in Dresden.

Finally, I would like to give special thanks to my parents, brother, sister and Kai for their care, support, and encouragement.

Hongchu Du

November 22, 2007, Dresden

This page is intentionally left blank.

Abstract

In this dissertation, $BaTiO_3$ nanocrystals, $Bi_4Ti_3O_{12}$ nanostructured microspheres, and cosubstituted $Bi_4Ti_3O_{12}$ nanoparticles and ceramics were prepared using solvothermal, hydrothermal and citrate-gel methods. The ferroelectric properties of the prepared cosubstituted $Bi_4Ti_3O_{12}$ ceramics were studied using *P–E* hysteresis loop, leakage, and polarization fatigue measurements.

A two-phase solvothermal synthesis approach for the preparation of hydrophobic $BaTiO_3$ nanocrystals was developed. The two-phase method is based on the growth of nanocrystals at the oil/water interface by the reaction between metal surfactant complexes in the oil phase and a mineralizer in the water phase. Three kind of organic solvents, hexadecene, toluene, and heptane were used as the oil phase and compared to each other with respect to the product quality. The $BaTiO_3$ particles are crystalline with a mean size of 3.7 nm and can be dispersed in a variety of organic solvents forming highly transparent dispersions. A hydrothermal method was developed for the synthesis of $Bi_4Ti_3O_{12}$ nanostructured microspheres consisting of granular nanoparticles and nano-platelets. The precursor powder was prepared using a diethylene glycol mediated coprecipitation method. Tailoring of the morphology was achieved by changing the precursor quantity, sodium hydroxide concentration, and reaction time. The formation mechanism of the nanostructured microspheres probably involves aggregation, followed by dissolution and recrystallization.

$Bi_{3.25}Pr_{0.75}Ti_{2.97}V_{0.03}O_{12}$ (BPTV) and $Bi_{3.25}La_{0.75}Ti_{3-x}M_xO_{12}$, ($BLTM_x$, M = Mo, W, Nb, V, x = 0.0–0.12) ferroelectric nanoparticles and ceramics were synthesized using a modified citrate-gel method that has a crystallization temperature as low as 450 °C. The synthesized nanoparticles were spherical ranging from 30 to 100 nm. Except Nb^{5+}, other donor cations were introduced using the corresponding oxides that have advantages in terms of high purity, low cost, and availability. The $Bi_{3.25}Pr_{0.75}Ti_{2.97}V_{0.03}O_{12}$ ceramic is orthorhombic and its $2P_r$ and $2E_c$ values measured at 300 kV/cm were 35 $\mu C/cm^2$ and 148 kV/cm respectively. The texture, microstructure, and ferroelectric properties of the prepared $Bi_{3.25}La_{0.75}Ti_{3-x}M_xO_{12}$, ($BLTM_x$, M = Mo, W, Nb, V, x = 0.0–0.12) ceramics depend on x. The maximum $2P_r$ (30–32 $\mu C\ cm^{-2}$) was achieved at an optimum cosubstitution level (x = 0.025 for M^{6+}, x = 0.03 for M^{5+}). The high remanent polarization, low leakage current, and low polarization fatigue render the prepared ceramics promising for practical applications.

This page is intentionally left blank.

Contents

1. Objective

Bulk ferroelectrics, including single crystals and ceramics, have wide applications for capacitors, actuators, piezoelectric transducers, pyroelectric detectors, and electrooptic devices using their ferroelectric, pyroelectric, piezoelectric, dielectric, and electrooptic properties, which are still important components in modern instruments and equipments. For a parallel plate capacitor, a large dielectric constant is needed to get a high capacitance per unit volume with a given area and thickness. $BaTiO_3$ based ceramics have high dielectric constants ($\varepsilon_r > 1000$) and have captured billions per year market in capacitors.[1] The piezoelectricity of ferroelectrics can be used in electromechanical devices. These devices include cantilever actuators, probes for atomic force microscopy, ultrasonic micromotors, micropumps, ultrasonic transducers for medical applications, and linear actuators.[2] Based on the pyroelectric effect, ferroelectric materials, such as lead titanate and barium titanate, can be used for infrared (IR) imaging. In comparison to quantum or photon IR detectors based on the photoelectric effect in III–V or II–VI semiconductors, such as gallium arsenide and mercury cadmium telluride, pyroelectric thermal detectors can be operated without cooling. Lang has listed several main advantages of the latter:[3] sensitivity over the entire electromagnetic spectrum, operation temperature range from a few to hundreds degrees Kelvin, and fast response (picoseconds), etc.

Ferroelectric nanomaterials have recently attracted considerable attention because of their promising applications in integrated microelectronic devices, especially in nonvolatile memories and microelectromechanical systems.[1, 4, 5] Used as high dielectric constant gate for dynamic random access memories (high-*k* DRAMs) is one application of ferroelectric materials in memory devices. $(Ba,Sr)TiO_3$ has emerged as the leading contender as a high-*k* dielectric for DRAMs.[6] In nonvolatile ferroelectric random access memories (NvFeRAMs), information is stored by the polarization direction in a ferroelectric film or island and the stored datum is read out by the polarization reversal current.[5] Ferroelectrics with a larger remanent polarization, low dielectric constant, and small coercive field are desired for NvFeRAMs. Furthermore, properties such as low polarization fatigue, long retention time, and small imprint effect are indispensable to guarantee the reliability. Besides the direct use of polarization reversal current, NvFeRAMs can use the polarization state dependent resistivity to sense the binary information, for example in a ferroelectric field transistor.[7]

It is widely accepted that the ferroelectricity in nanoparticles vanishes below a critical size of a few to a few tens nanometers, because the balance between the long-range Coulomb interactions and short-range covalent interactions is altered with respect to the bulk material.[8] Therefore, the development of new feasible methods to synthesize isolated ferroelectric nanoparticles with narrow size distribution will facilitate studies on the size effect of ferroelectricity. Moreover, the synthesis of nanocrystals with dimensions comparable to the electron mean free path, 0.1 to 1.0 nm for an ABO_3 ferroelectric perovskite depending on applied electric field,[9] will promote experimental investigations on quantum confinement in nanoscale ferroelectrics. Furthermore, nanocrystals are promising building blocks for the bottom-up assembly of novel nanostructures with potential applications in integrated dielectric, ferroelectric, and electrooptic devices. Additionally, the use of nanoparticles for the preparation of ceramics may result in a significant lowering of sintering temperatures, improved functional properties, and the increased mechanical strength of ceramic components due to improved homogeneity and controlled particle size distribution in green bodies. The great theoretical and technological interests have been driving the development of preparation of ferroelectric nanoparticles.

$BaTiO_3$ nanocrystals with crystallite size of 9 nm have been early reported by Herrig and Hempelmann using microemulsion method with no calcination.[10, 11] Later an injection hydrolysis method[12] and a solvothermal method[13, 14] have been developed to prepare $BaTiO_3$ nanocrystals with a size around 10 nm. Despite these advances, there is still a need for methods producing $BaTiO_3$ nanocrystals with a size below 5 nm that can be dispersed in organic solvents to form transparent dispersions.

$Bi_4Ti_3O_{12}$ has a lead-free composition, high Curie temperature (675 °C),[15] large spontaneous polarization (50 $\mu C/cm^2$)[16, 17] and low crystallization temperature (500 and 650 °C)[18-20] that make it one of the most promising lead-free ferroelectric materials for high temperature piezoelectric and ferroelectric applications. However, pure $Bi_4Ti_3O_{12}$ shows low remanent polarization (P_r),[21-24] high leakage,[21, 24-26] and polarization fatigue failures,[22] limiting its practical applications. Bismuth vacancies accompanied with oxygen vacancies in the perovskite layers have been suggested to be responsible for the domain-wall pinning, polarization fatigue, and high electrical leakage.[26-29] Lanthanoid cations (La^{3+}, Pr^{3+}, Nd^{3+}, etc.) isovalent substitution for Bi^{3+} at perovskite A-site,[28, 30, 31] donor cations (V^{5+}, Mo^{6+}, W^{6+}, etc.) aliovalent substitution for Ti^{4+} at perovskite B-site,[23, 24] and cosubstitution both at perovskite A- and B-site[25, 32-37] have been found to be effective ways to reduce bismuth vacancies and stabilize oxygen in the perovskite layers, thereby improving the ferroelectric performances. However, most of studies are on the substituted $Bi_4Ti_3O_{12}$ thin films, especially in the case of the cosubstituted $Bi_4Ti_3O_{12}$. Few studies have been reported on the cosubstituted $Bi_4Ti_3O_{12}$ nanoparticles and bulk ceramics.[38-40] The extensive studies in ferroelectric thin films may be attributed to their promising applications in the increasingly miniaturized integrated devices such as nonvolatile ferroelectric random access memories (FeRAM) and microelectromechanical systems (MEMS).[1, 4, 5] In most cases, the ferroelectric thin films have to be prepared on certain substrates. Either the mismatch of lattice constants or the difference of thermal expansion coefficients between the ferroelectric films and the substrates, will cause considerable in-plane stress, under hundreds of MPa to Gpa, in the as-prepared films.[41] These stresses have crucial influences on the ferroelectric properties.[9, 41, 42] Therefore, studies on the bulk ceramics may exclude the effects imposed by the substrates, thereby, clarifying the influences of the cosubstitutions on the microstructures and ferroelectric properties of the concerned ferroelectric materials.

Therefore, the main objective of this dissertation is to develop chemical solution methods to prepare isolated sub-5 nm $BaTiO_3$ nanocrystals that can be dispersed in organic solvents to form transparent dispersions, to prepare A- and B-site cosubstituted $Bi_4Ti_3O_{12}$ nanoparticles, and to study the ferroelectric properties of the cosubstituted $Bi_4Ti_3O_{12}$ ceramics fabricated using the prepared nanoparticles.

2. Introduction

2.1 Ferroelectricity

A ferroelectric is defined as a crystal, which in some accessible range of environmental conditions has two or more equilibrium intrinsic lattice electric polarization states in the absence of an electric field, and in which the spontaneous intrinsic lattice electric polarization can be switched between those orientations by a realizable, appropriately oriented electric field.[1, 4, 9, 41, 43] The spontaneous electric polarization, P_s, in a ferroelectric is an intrinsic lattice polarization resulting from a spontaneously formed electric dipole moment, and its orientations are determined by the crystal structure. On cooling from high temperatures, ferroelectrics usually exhibit a structural phase transition from a paraelectric parental (prototypal) phase into a ferroelectric phase. The symmetry of the ferroelectric phase, is always lower than that of the paraelectric parental phase.[4]

2.1.1 History and Definition

Ferroelectricity is a phenomenon of crystalline materials that was discovered by Joseph Valasek in Rochelle salt (sodium potassium tartrate tetrahydrate, $NaKC_4H_4O_6 \cdot 4H_2O$) in 1920.[44] The horizon for workers in ferroelectrics was significantly broadened in 1935 by Busch and Scherer's report of the ferroelectricity in potassium dihydrogen phosphate (KH_2PO_4, KDP).[45] However, studies on the fragile water-soluble hydrogen bonded ferroelectrics had been academic curiosities until the discovery of the ferroelectricity in a simple perovskite structured oxide $BaTiO_3$ in 1940s.[46-48] Since then, many other robust ferroelectric oxides, including lead titanate ($PbTiO_3$),[49] bismuth titanate ($Bi_4Ti_3O_{12}$),[50, 51] lithium niobate ($LiNbO_3$) and lithium tantalate ($LiTaO_3$),[52] and so forth, have been discovered, rendering that the theoretical and applicational studies on ferroelectrics have been being one of the most active research areas in the field of solid state materials.

Ferroelectricity is a property associated with the switchable spontaneous electric polarization of a ferroelectric in its ferroelectric phase. The spontaneous electric polarization, P_s, in a ferroelectric phase is formed via a lattice distortion with respect to a higher symmetric paraelectric parental phase. As illustrated in Fig 2.1, the displacement of the central Ti^{4+} ion is accompanied with an extension of the unit cell along a [001] direction with respect to the cubic paraelectric structure leading to a spontaneous polarization.

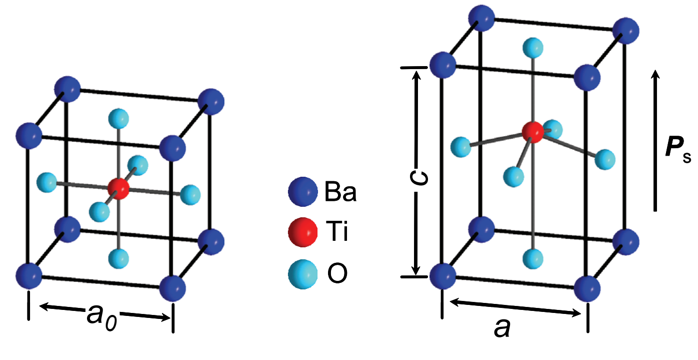

(a) $T>T_c$, Cubic

(b) $T>T_c$, Tetragonal

Fig 2.1 Schematic illustration of the phase transition of barium titanate ($BaTiO_3$) from a cubic paraelectric structure to a tetragonal ferroelectric structure.

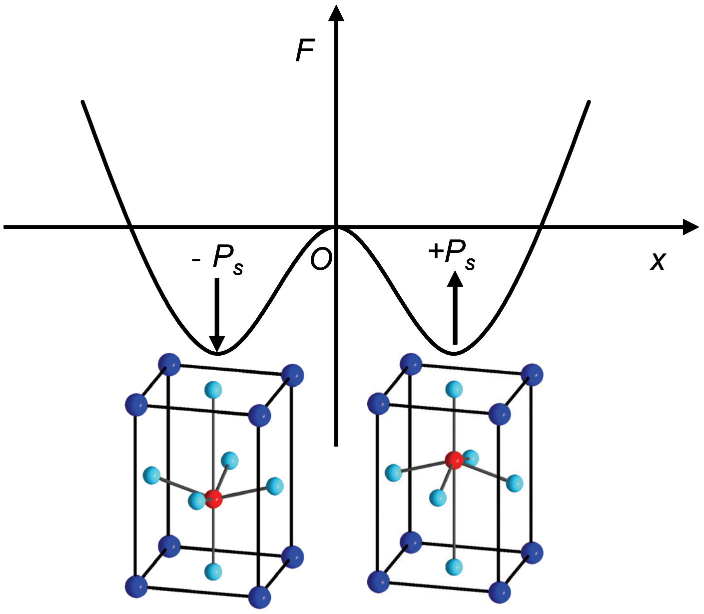

Fig 2.2 Schematic illustration of free energy (*F*) as function of displacement (*x*) of Ti^{4+} ion along a [001] direction with respect to the central site in a BaTiO$_3$ unit cell.

Ferroelectricity is distinguished from electret effect in that the ferroelectric polarization is spontaneously formed thermodynamic stable electric polarization determined by the intrinsic crystal lattice (Fig 2.2).[41] The double-well energy potential implies the two thermodynamically equivalent P_s states. However, an electret is a dielectric that contains a net oriented electric dipoles or space charges resulting from trapped charges.[53] As pointed by Scott et al.,[54] phenomena associated with electrets could be misinterpreted as true ferroelectricity without the knowledge of the crystal structure.

2.1.2 Crystal Symmetry

As seen in Table 2.1,[55] all the crystalline materials can be described by the 32 crystallographic point groups, in which 11 point groups are centrosymmetric and have an inversion center. All other 21 point groups do not possess an inversion center and are noncentrosymmetric, and have one or more crystallographically unique directional axes. Except the '432' point group, all other 20 noncentrosymmetric point groups exhibit piezoelectricity along the unique directional axes. Piezoelectricity depicts the ability of certain crystalline materials to develop an electrical charge proportional to a mechanical stress. It was discovered by the Curie brothers in 1880. The phenomenon of linear change in polarization P to the applied mechanical stress X is referred to as the direct piezoelectric effect (Eq 2.1).

$$\frac{\partial P_i}{\partial X_{jk}} = d_{ijk}^{E} \qquad \textbf{Eq 2.1}$$

Here the piezoelectric coefficient d_{ijk} is a third rank tensor. The effect of the change in mechanical strain S in proportion to the applied electric field E is called the converse piezoelectric effect (Eq 2.2).

$$\frac{\partial S_{jk}}{\partial E_i} = d_{ijk}^{T} \qquad \textbf{Eq 2.2}$$

Table 2.1 Point group symmetry vs. piezoelectricity and pyroelectricity.

Crystal System	Crystallographic Point Groups			
	Centrosymmetric	Noncentrosymmetric		
			Piezoelectricity	Pyroelectricity
Triclinic	$\bar{1}$	1	+	+
Monoclinic	2/m	2	+	+
		m	+	+
Orthorhombic	mmm	222	+	−
		mm2	+	+
Tetragonal	4/m 4/mmm	4	+	+
		$\bar{4}$	+	−
		422	+	−
		4mm	+	+
		$\bar{4}2m$	+	−
Trigonal	$\bar{3}$ $\bar{3}m$	3	+	+
		32	+	−
		3m	+	+
Hexagonal	6/m 6/mmm	6	+	+
		$\bar{6}$	+	−
		622	+	−
		6mm	+	+
		$\bar{6}2m$	+	−
Cubic	$m\bar{3}$ $m\bar{3}m$	23	+	−
		432	−	−
		$\bar{4}3m$	+	−

The converse and direct piezoelectric coefficients *d* are thermodynamically identical.[4] In the 20 point groups which show the piezoelectric effect, 10 point groups have only one unique directional axis. Crystals in such point groups are called polar crystals since they may show spontaneous polarization P_s parallel to the polar axis. The spontaneous polarization is governed by the dipole moment per volume or by the net charge per unit area on the surface perpendicular to the unique polar axis. The change of the spontaneous polarization with temperature is called pyroelectric effect or pyroelectricity. The pyroelectricity can be quantified by the pyroelectric coefficient p_i (C m^{-2} K^{-}):

$$p_i = \left.\frac{\partial P_{s,i}}{\partial T}\right|_{\substack{E=0 \\ X_{ij}=0}} \qquad \textbf{Eq 2.3}$$

Here constrains are zero applied electric field and zero (or constant) stress. Eq 2.3 depicts the primary pyroelectric effect. The secondary pyroelectric effect is a result of the direct piezoelectric effect (Eq 2.1) because in a mechanically clamped sample the change in the temperature will cause stress through thermal expansion. Moreover, the dielectric constant is generally dependent on temperature, a nonpyroelectric material therefore may show a pyroelectric-like response if it is biased by an electric field, as expressed by Eq. 2.4, 2.5.

$$D = \varepsilon_0 \varepsilon_r E \qquad \textbf{Eq 2.4}$$

$$p_i' = \varepsilon_0 E_i \frac{\partial \varepsilon_{r,ij}}{\partial T} \qquad \textbf{Eq 2.5}$$

The relations between mechanical, thermal, and electrical effects in a pyroelectric are shown in Fig 2.3.

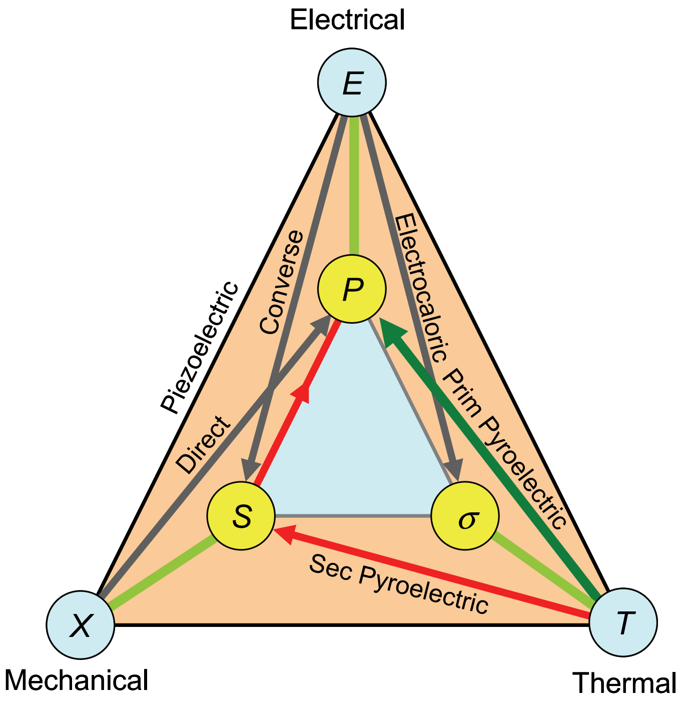

Fig 2.3 Mechanical, thermal and electrical coupling in a pyroelectric.[3]

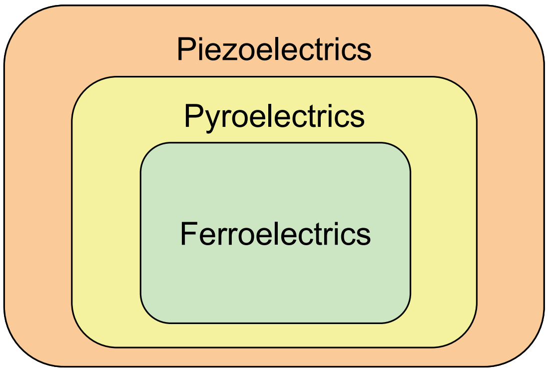

Fig 2.4 Relationship between piezo-, pyro-, and ferroelectrics.

A pyroelectric crystal in which the magnitude and direction of P_s can be reversed by a realizable, appropriate oriented electric field is called a ferroelectric. All ferroelectrics show piezoelectric and pyroelectric effects (Fig 2.4). A large number of applications of ferroelectric materials exploit such properties that are an indirect consequence of ferroelectricity.

2.1.3 Ferroelectric Domains

A ferroelectric domain is a region of a ferroelectric crystal in which the polarization is homogeneous and uniform in magnitude and direction. The dimension of a ferroelectric domain is in the range from 0.1 to 100 µm.[41] In a freshly prepared ferroelectric sample, domains are inclined to form "head-to-tail" configurations thereby reducing the electrostatic energy of the noncompensated polarization charges div(P_s), called depolarization energy.[41, 56] The lamellar and herringbone patterns are common ferroelectric domain patterns (Fig 2.5). The types of ferroelectric domain state in a ferroelectric material are limited by its lattice symmetry (Table 2.2). However, the number and the pattern of domains in a realistic sample is quite complicated because of the differences in electric and elastic boundary conditions, defect structure, and the samples thermal, electrical, and mechanical history.[41]

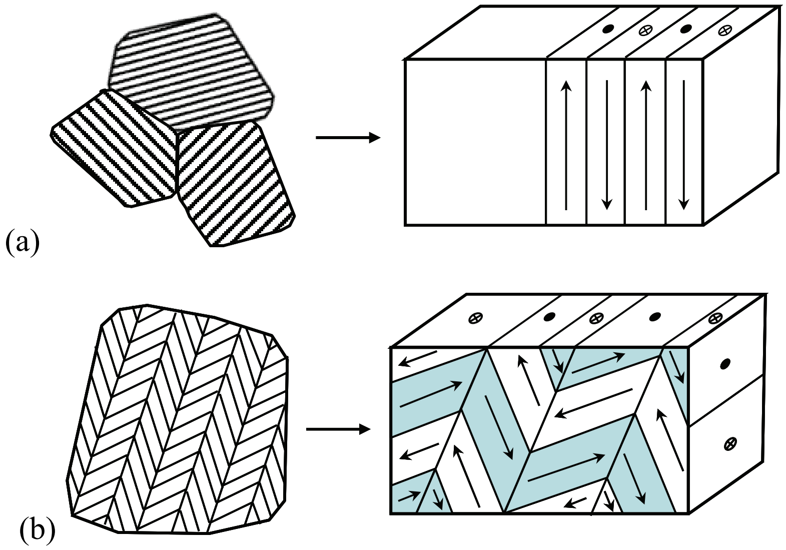

Fig 2.5 Ferroelectric domain patterns (a) lamellar structure, (b) herringbone structure.

Table 2.2 Ferroelectric domain states vs. symmetries of primary ferroelectrics.

Ferroelectrics	Phase Trans. Temp (ºC)*	Point Group Symmetries	Ferroelectric (Ferroelastic) Domain States
$BaTiO_3$	130, 5, –90	m3m→4mm→mm2→3m	6(3), 12(6), 8(4)
$KNbO_3$	435, 225, –90	m3m→4mm→mm2→3m	6(3), 12(6), 8(4)
$PbTiO_3$	490	m3m→4mm	6(3)
$LiNbO_3$	1210	–3m→3m	2(1)
$LiTaO_3$	665	–3m→3m	2(1)
$BiFeO_3$	850	m3m→3m	8(4)
$PbNb_2O_6$	570	4/mmm→m2m	4(2)
$Ba_2NaNb_5O_{15}$	560, 300	4/mmm→4mm→m2m	2(1), 4(2)
$SrBi_2Ta_2O_9$	310	4/mmm→m2m	4(2)
$Bi_4Ti_3O_{12}$	675	4/mmm→m2m	8(4)

*Transition temperatures can be hysteretic, and can dependent on the boundary conditions. Data were selected from Ref[41].

The boundary region between two ferroelectric domains defines a domain-wall, in which the crystalline structure is disturbed and the energy per unit cell is somewhat higher than in the neighboring domains. Its typical thickness is a few lattice constants.[41] A domain-wall is characterized by an angle between the orientation of the polarization in the neighboring domains, by wall orientation, and by wall energy. Only the pairs or assemblies of domains separated by non-180°walls, such as 90°domain-walls in tetragonal structures, 70°and 109° domain-walls in rhombohedral structure, have the potential contributions to the piezoelectric effect and to reduce elastic energy.[57]

The domain patterns can be visualized by polarized-light microscopy, high-resolution electron microscopy (HREM), scanning electron microscopy (SEM), piezoelectric force microscopy (PFM), etc.

2.1.4 *P–E* Hysteresis Loop

A main difference between a pyroelectric and a ferroelectric is that the spontaneous polarization in a ferroelectric can be reoriented by an applied electric field. The ferroelectricity is therefore manifested by a ferroelectric *P–E* hysteresis loop (Fig 2.6).

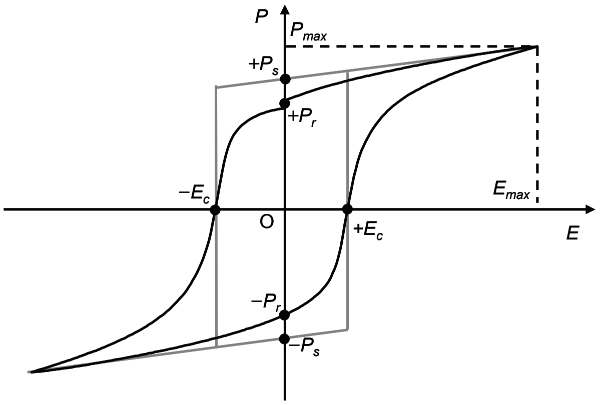

Fig 2.6 Illustration of ferroelectric hysteresis loops of an ideal ferroelectric capacitor (gray) and a polycrystalline bulk ceramic sample (black).

In most cases, a ferroelectric *P–E* hysteresis loop is obtained from a ferroelectric capacitor with a metal-ferroelectric-metal configuration. An ideal ferroelectric capacitor, a single domain single crystal, shows a square *P–E* hysteresis loop (Fig 2.6) defined by the spontaneous polarization P_{s}, the linear dielectric permittivity $\varepsilon_{\mathrm{fe}}$, and the coercive field E_{c}. An applied electric field with amplitude above E_{c} is needed to reverse the ferroelectric polarization. In a real ferroelectric material, a *P–E* hysteresis loop is formed in the switching process through the growth of existing domains antiparallel to the applied field by domain-wall motion, or through the nucleation and growth of new antiparallel domains.[43] Consequently, domains are favorable oriented with respect to the applied electric field. The resulting electric polarization at zero applied electric field is defined as the remanent polarization P_{r}, which is always smaller than P_{s} because of the existence of domains and back-switching. The polarization obtained at the maximum applied field E_{max} is the maximum polarization P_{max}.

The measured *P–E* hysteresis loops of a given material are dependent on the electrodes (materials and configurations), the thickness, the applied field (waveform, amplitude, and frequency), the history (thermal, mechanical and electrical) of the sample, and on the temperature, etc.

2.1.5 Effects of Defects

Defects in the crystal lattice generally cause deformation of the surrounding volume and modification of the local fields,[43] which have considerable influences on the dielectric properties and switching behavior of ferroelectrics. Defects, including oxygen vacancies, space charges, etc., and their distribution in a ferroelectric have been considered to play important roles in the ferroelectric domain-wall pinning, polarization fatigue, etc.

Domain-wall pinning (or clamping) is referred to as the immobilization of domain-walls caused by their interaction with defects.[4, 58] The general scenario of domain-wall pinning is caused by charged defects, such as oxygen vacancies, and/or electrons trapped in the domain-walls or grain boundaries through compensating the depolarization fields generated by discontinuity in polarization div(P).[4] Removal of these fields will decrease the energy of the domain-wall, thereby inhibiting the domain-wall motion.[4, 43] As a result, domain-wall pinning in a ferroelectric will reduce the remanent polarization.

Polarization fatigue manifests itself as the decrease of the remanent polarization with cyclic polarization reversals. The origin of fatigue is still not well understood. One consensus reached is that polarization fatigue is a defects related phenomenon, and is closely related to domain-wall pining. The proposed polarization fatigue mechanisms include domain-wall pinning by defects trapped in domain-walls,[59] [60] domain-wall pinning by oxygen vacancy ordering,[61, 62] suppression of the nucleation of oppositely oriented domains at the surface by nearby-electrode injections,[58] formation of a nonferroelectric surface layer (polarization loss by a voltage drop through this layer),[63] etc. In a practical ferroelectric, two or more polarization fatigue mechanisms often coexist.

2.1.6 Curie–Weiss Law

The concept of a phase transition is crucial to explaining ferroelectricity. The temperature at which the crystal transforms from one phase to another is called the transition temperature. Some ferroelectric materials, such as $BaTiO_3$, $KNbO_3$ have more than one ferroelectric phases and phase transitions. On decreasing the temperature, only a transition temperature at which a ferroelectric crystal transforms from a parental paraelectric phase to the first ferroelectric phase is called Curie point (T_c). Above the T_c, the dielectric susceptibilityχ, for a small electric field applied along the prospective ferroelectric axis, satisfies the Curie–Weiss law:

$$\chi = \frac{C}{T - \Theta} \qquad \textbf{Eq 2.6}$$

Here ε_0 is the dielectric permittivity of vacuum, C is a positive constant, Θ is the Curie–Weiss temperature, which is a formula constant.

The Curie–Weiss temperature Θ is different from the Curie point T_c. As seen in Fig 2.7, for a second order phase transition $\Theta = T_c$, and ε sharply decreases for $T < T_c$. For a first order transition, $\Theta < T_c$ and χ shows discontinuously decrease at T_c. According to Eq 2.7,

$$\chi = \varepsilon_r - 1 \qquad \textbf{Eq 2.7}$$

the dielectric constant goes through a sharp maximum near the transition temperature. This ‘dielectric anomaly’ has been a widely accepted intrinsic feature of a ferroelectric.

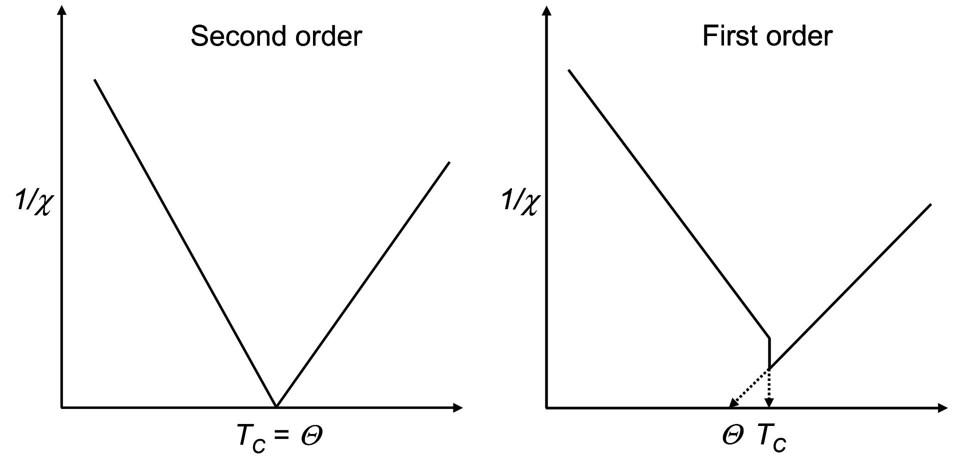

Fig 2.7 Illustration of Curie–Weiss Law

2.2 Types of Ferroelectrics

The majority of technical important ferroelectric materials are complex oxides having a perovskite structure or a variant of the perovskite structure, such as ilmenite structure, bismuth layer structure, tungsten bronze structure, and so forth. These ferroelectric materials include barium titanate ($BaTiO_3$), lead titanate ($PbTiO_3$), lead zirconate titanate (PZT), lead lanthanum zirconate titanate (PLZT), lead magnesium niobate (PMN), potassium niobate ($KNbO_3$), potassium sodium niobate ($K_xNa_{1-x}NbO_3$), and sodium bismuth titanate ($Bi_{0.5}Na_{0.5}TiO_3$), lithium niobate ($LiNbO_3$), lithium tantalate ($LiTaO_3$), bismuth titanate ($Bi_4Ti_3O_{12}$), strontium bismuth tantalate ($SrBi_2Ta_2O_9$), etc.

2.2.1 Perovskite

Perovskite represents a structural family, in addition to being the particular mineral name of calcium titanate ($CaTiO_3$). A perovskite structure has a general formula of ABX_3, in which the smaller B-site cations occupy the octahedral interstices and are 6-fold coordinated with the X-site anions. The dodecahedral space between the corner-shared coordination octahedra of BX_6 are occupied by larger A-site cations, which are 12-fold coordinated with the X-site anions (Fig 2.8). A-site cations can be monovalent ions such as Na^+, K^+, etc., or divalent ions like Ca^{2+}, Sr^{2+}, Ba^{2+}, Pb^{2+}, etc., or trivalent ions such as Bi^{3+}, Y^{3+}, and lanthanoid cations. B-site cations can be tri-, tetra-, penta-, or hexavalent cations such as Fe^{3+}, Ti^{4+}, Nb^{5+}, Ta^{5+}, Mo^{6+}, W^{6+}, etc. Alternatively, the ideal perovskite structure can be depicted by the cubic ABCABC stacking of close-packed AX_3 planes with B–site cations coordinated by six X-site anions in octahedra.[64] In most cases X is oxygen, however fluorine and chlorine, or a mixture of these anions are possible.

The earliest systemic studies on the perovskite-structured compounds can be tracked back to V. M. Goldschmidt's pioneering work in 1920s. A large number of first synthetic perovskites and their variants were presented by Goldschmidt, including important materials still being studied in present day, such as $BaTiO_3$, $SrTiO_3$, $LiNbO_3$, $KNbO_3$, and $NaNbO_3$, etc.[65, 66] The relation between the ionic radii and perovskite structures is given by the Goldschmidt tolerance factor t_G defined by Eq 2.8 where R represents the ionic radius of the subscript-site ion. [67]

$$t_{\mathrm{G}} = \frac{R_{\mathrm{A}} + R_{\mathrm{X}}}{\sqrt{2}(R_{\mathrm{B}} + R_{\mathrm{X}})} \qquad \textbf{Eq 2.8}$$

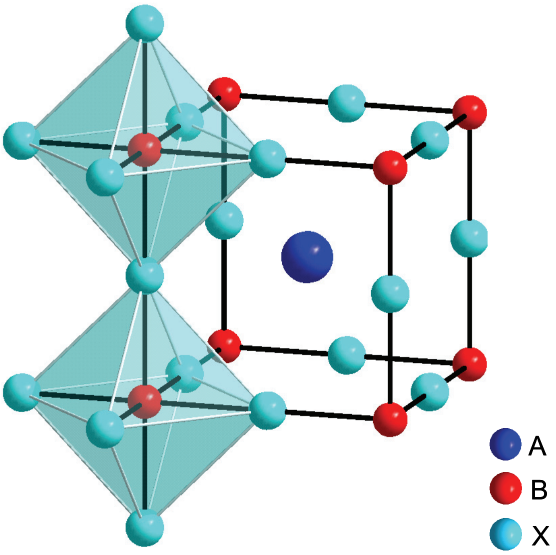

Fig 2.8 Illustration of the cubic ABX_3 perovskite structure.

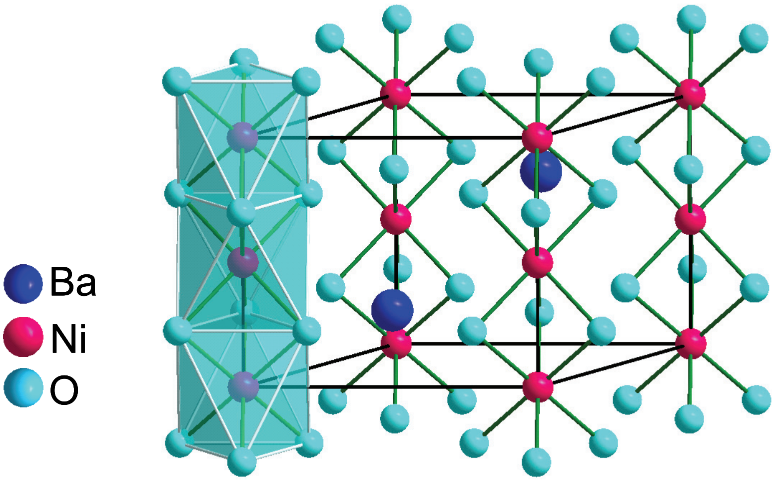

Fig 2.9 Hexagonal structure of $BaNiO_3$ ($t_G = 1.13$, $R_A = 1.61$ Å, $R_B = 0.48$,) containing face sharing NiO_6 octahedra.

A t_G has a value between 0.8 and 1.0.[67] It is worthy of mention that the Eq 2.8 is based on the rigid sphere model where purely or a high degree of ionic bonding is expected.

The perovskite structure is adaptable to a great many of the A–site and B–site cation species with a deviation from the equilibrium t_G and allows for more than one A-site cation and/or B–site cation species, thereby leading to a large number and variety of stoichiometric compounds with perovskite or its variant structures.[66] The perovskite structures derived from the ideal cubic structure are known to be tetragonal, orthorhombic, rhombohedral, or monoclinic symmetry.[68]

The ideal cubic perovskite structure has $t_G = 1$, such as $SrTiO_3$ where $R_A = 1.44$ Å, $R_B = 0.605$, and $R_X = 1.40$ Å with a coordination number of 12, 6, and 6 for A-site, B-site and X-site ions respectively. A $t_G < 1$ causes tension in the A–X bonds and the B–X bonds under compression. The structure may reduce these stresses by tilt of the BX_6 octahedra that lowers the space group symmetry from cubic ($Pm\bar{3}m$) to orthorhombic, rhombohedral, or monoclinic. If $t_G < 0.8$, the ilmenite structure is more stable. A $t_G > 1$ renders the B–X bonds under tension and the A–X bonds under compression. The structure may reduce the stresses by introducing hexagonal ABAB stacking, which results in sharing faces of BX_6 octahedra and a hexagonal structure (Fig 2.9). Alternatively, the stresses may be reduced by the elongation of the unit cell along a [001] direction with respect to the cubic structure (Fig 2.1). In this case, the B–X bond may develop a double-well potential energy that results in ferroelectricity (Fig 2.2).

The Goldschmidt tolerance factor is a rough estimation of the perovskite structure. However, it provides guidelines for tailoring the perovskite structure by substitutions of cations with different ionic radii for A-site and/or B-site cations.

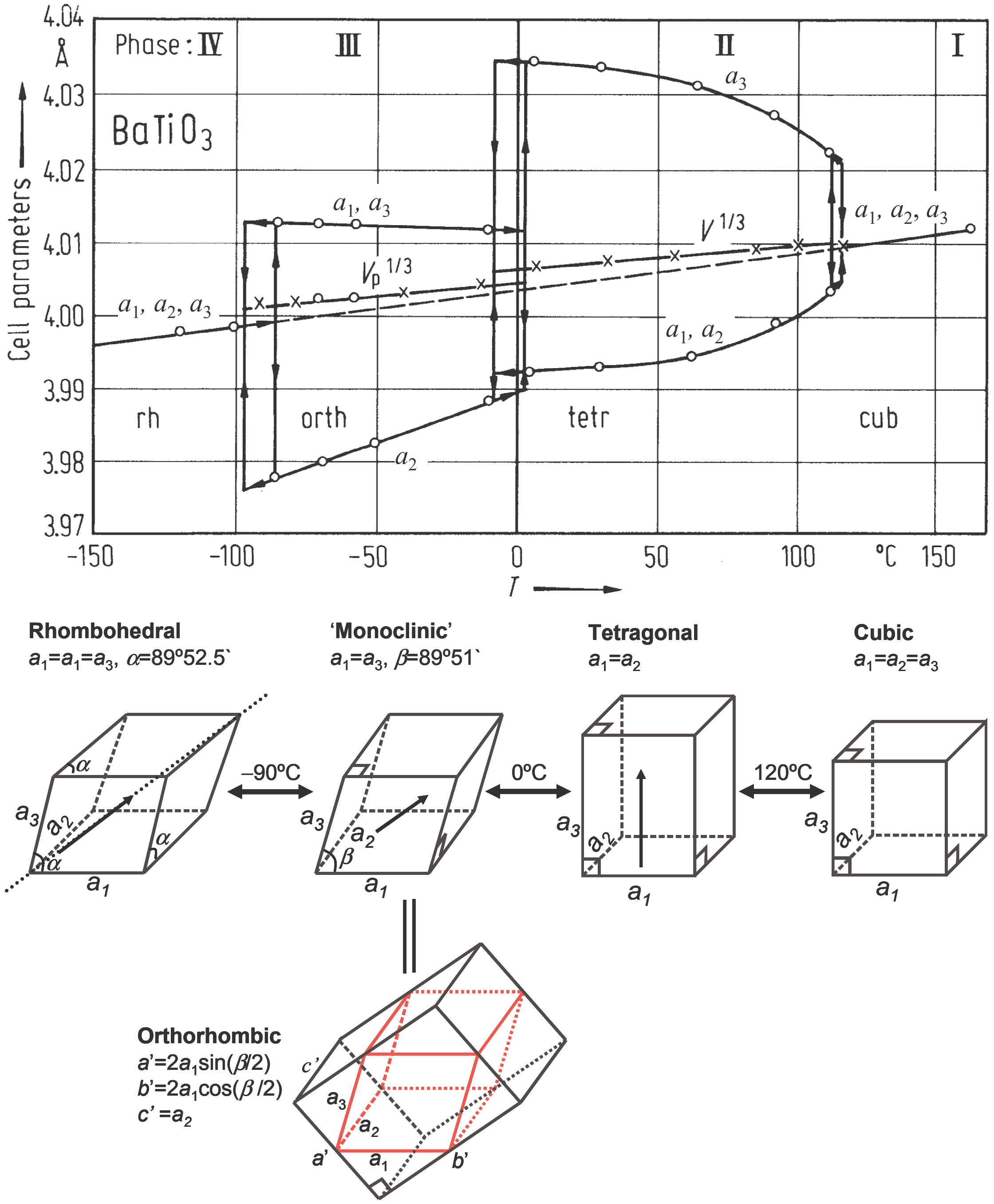

Fig 2.10 Phase transitions, spontaneous polarization vectors, and unit cell dimensions vs. temperature in a $BaTiO_3$ crystal. [71, 72]

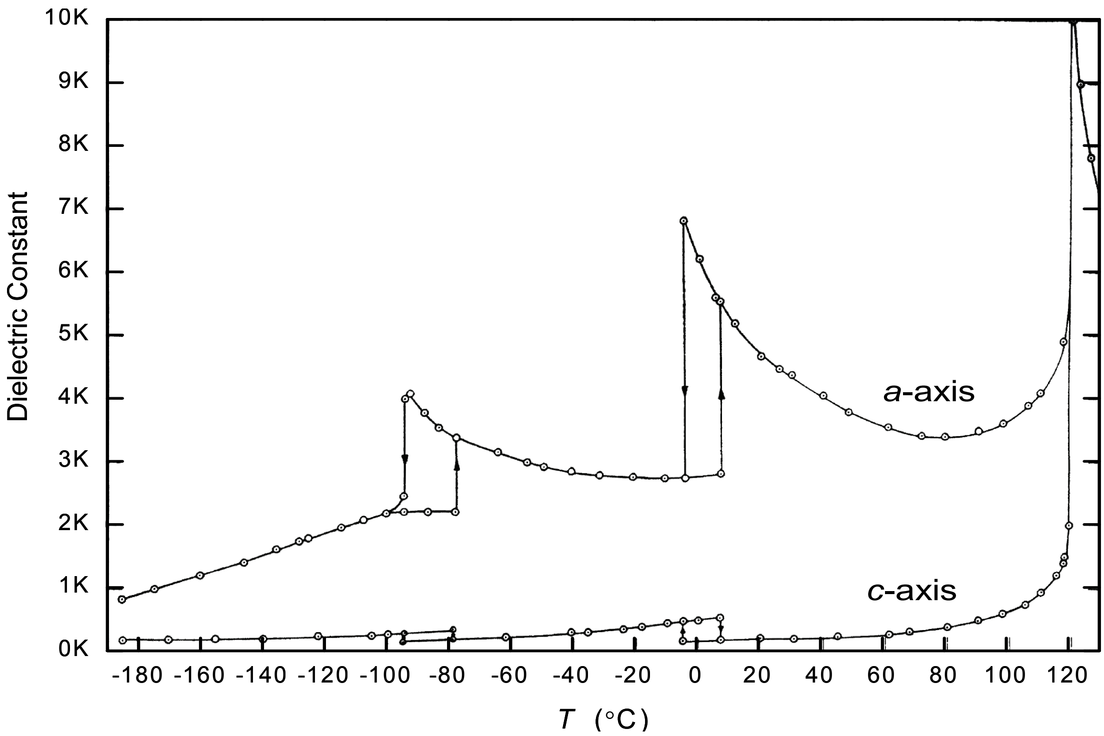

Fig 2.11 Dielectric constant of single domain of $BaTiO_3$ single crystal.[48, 73]

Table 2.3 Effect of solid solution substitutions on the phase transitions of $BaTiO_3$ ceramics.[70]

Additives	Solid Solution Limit (mol %)	Change in transition (°C/mol%)		
		ΔT_c	ΔT_1	ΔT_2
$PbTiO_3$	100	+3.7	−9.5	−6.0
$SrTiO_3$	100	−3.7	−2.0	0
$CaTiO_3$	21	0	−6.7	−6.0
$BaZrO_3$	100	−5.3	+7.0	+18
$BaSnO_3$	100	−8.0	+5.0	+16
$KNbO_3$	100	−9.0	+12	+35
$Ba(Fe_{1/2}Ta_{1/2})O_3$	100	−15	−2	−6
$Ba(Co_{1/2}W_{1/2})O_3$	50	−30		
$(K_{1/2}Nd_{1/2})TiO_3$	15	−10	−8	−6
$(K_{1/2}La_{1/2})TiO_3$	15	−15		
$La_{2/3}TiO_3$	15	−18		
$Ba_{1/2}NbO_3$	14	−26	+12	+6
$Ba_{1/2}TaO_3$	14	−29		

T_c: Curie point, tetragonal / Cubic; T_1: orthorhombic / tetragonal; T_2: rhombohedral / orthorhombic.

2.2.1.1 $BaTiO_3$

$BaTiO_3$ is the first discovered, the most extensively studied and the most widely used simple perovskite ferroelectric oxide. The discovery of ferroelectricity in $BaTiO_3$ is in 1940s by von Hippel (USA), and Wul and Goldman (Russia).[47] $BaTiO_3$ is a member of perovskite family as described much earlier by Goldschmidt in 1920s.[65, 67] The room temperature tetragonal structure of $BaTiO_3$ was first reported by Megaw in 1946.[68] $BaTiO_3$ has an ideal cubic perovskite structure above the Curie point (T_c = 120 ºC) and undergoes a successive phase transitions to three ferroelectric phases as temperature is lowered (Fig 2.10).

At T_c = 120 ºC, $BaTiO_3$ has a paraelectric–ferroelectric phase transition from the cubic to a tetragonal room–temperature ferroelectric phase with $c/a \approx 1.01$, which is stable from −5 to 120 ºC. In the tetragonal ferroelectric phase, the spontaneous polarization aligns along an original [001] direction of the ideal cubic perovskite unit cell as marked by an arrow in Fig 2.10. $BaTiO_3$ has two ferroelectric–ferroelectric phase transitions at −5 ºC from tetragonal to orthorhombic and at −90 ºC from orthorhombic to rhombohedral (Fig 2.10). The orthorhombic distortion of the $BaTiO_3$ structure exists between −90 to −5 ºC.[69] The rhombohedral structure is stable below −90 ºC. The spontaneous polarization vectors are along the original [110] and [111] direction of the ideal cubic perovskite unit cell for the orthorhombic and rhombohedral ferroelectric phases, respectively. The change of unit cell dimensions as function of temperature is given in the upper part of Fig 2.10， in which the orthorhombic structure referred to monoclinic axes is also drawn.

The multi-phase transition feature of $BaTiO_3$ results in exceptionally high dielectric constant ($\varepsilon_r > 1000$) because 'dielectric anomaly' at each of the transition temperature (Fig 2.11). The high dielectric constant makes $BaTiO_3$ an attractive material for dielectric applications. However, the significant temperature dependence of dielectric constant has to be reduced. The phase transition temperatures of $BaTiO_3$ ceramics have been found to be shifted by substitutions.[70, 71] As seen in Table 2.3, except $PbTiO_3$, all other substitutions result in a decrease of the Curie point. $Ba_{1-x}Sr_xTiO_3$ has been one of the most extensively studied systems among these solid solutions. By adjusting the substitution level, the Curie point can be shifted to room temperature with a broad permittivity peak ($\varepsilon_r > 10000$).[71] The permittivity peak broadening has been explained by macroscopic heterogeneity in the composition giving rise to a distribution of Curie points and thus a broadened peak.[71]

The ferroelectric spontaneous polarization for a [001] oriented $BaTiO_3$ single crystal is about 26 $\mu C/cm^2$ at 20 ºC.[71] In polycrystalline ceramics, both maximum and remanent polarizations are much lower than those in single crystals because the existence of grain boundaries and random orientation of grains, which yield much more complex domain structures. The low Curie point and spontaneous polarization make $BaTiO_3$ less competitive than $PbTiO_3$ (T_c = 490 ºC) and other high Curie point ferroelectrics, such as $SrBi_2Ta_2O_9$ (T_c = 310 ºC), $Bi_4Ti_3O_{12}$ (T_c = 675 ºC) for ferroelectric memory applications.

2.2.1.2 $PbTiO_3$

Lead titanate is another important member of ferroelectric perovskites having a structure analogous to $BaTiO_3$. At room temperature, $PbTiO_3$ has a tetragonal phase with $c/a \approx 1.063$.[49, 74] The Curie point of $PbTiO_3$ is 490 °C.[49] Through Curie point on increasing the temperature, the structure changes from the ferroelectric tetragonal phase to the paraelectric parental cubic phase similar to that in $BaTiO_3$.[49, 74] Pure $PbTiO_3$ is difficult to prepare in the bulk ceramic form because a large volume change on cooling below its Curie point results in crack and fracture during preparation.

The solid solution of $PbTiO_3$-$PbZrO_3$ (PZT) is one of the most important ferroelectric and piezoelectric materials. In this solid solution, there is a morphotropic boundary (MPB), which is a nearly temperature-independent boundary in a solid solution phase diagram between ferroelectric phases of different composition, and the two structural states differ only in symmetry and both of them are sub-groups of the parental phase.[41] At the MPB of PZT (a Zr/Ti ratio of ~ 52/48 at room temperature), the tetragonal and the rhombohedral phases co-exist resulting in a high polarization because of the presence of more possible polarization directions (6 of tetragonal phase and 8 of the rhombohedral phase).[57] La^{3+} substitution for Pb^{2+} in the perovskite A-site of PZT forms an important transparent ferroelectric ceramic PLZT, which has been found in electrooptic applications.

The larger remanent polarization and relatively high Curie point make the lead based perovskite ferroelectricsc still be candidates for future electric, electrooptic, and electromechanical applications. Even though the lead content has been considered as a drawback for these ferroelectrics, the main shortage may be the high polarization fatigue, which causes serious reliability problems in practical applications, such as nonvolatile random access memories.

2.2.2 Bismuth Oxide Layered Perovskites

Bismuth (oxide) layered perovskite represents another important family of ferroelectrics. A larger number of bismuth layered perovskites were discovered by Aurivillius,[75-77] which have a generic formula of $(Bi_2O_2)^{2+}(A_{n-1}B_nO_{3n+1})^{2-}$, where A represents mono- (Na^+, K^+), di- (Ca^{2+}, Sr^{2+}, Ba^{2+}, Pb^{2+}), or trivalent (Y^{3+}, Ln^{3+}, Bi^{3+}) ions, B stands for tri- (Fe^{3+}, Ga^{3+}, Cr^{3+}), tetra- (Ti^{4+}), penta- (Nb^{5+}, Ta^{5+}), or hexavalent (W^{6+}, Mo^{6+}) ions, and n equals 1 to 6. The structure is described as a pseudo-perovskite layer $(A_{n-1}B_nO_{3n+1})^{2-}$, containing n perovskite type units, sandwiched between bismuth oxide layers $(Bi_2O_2)^{2+}$ (Fig 2.12).

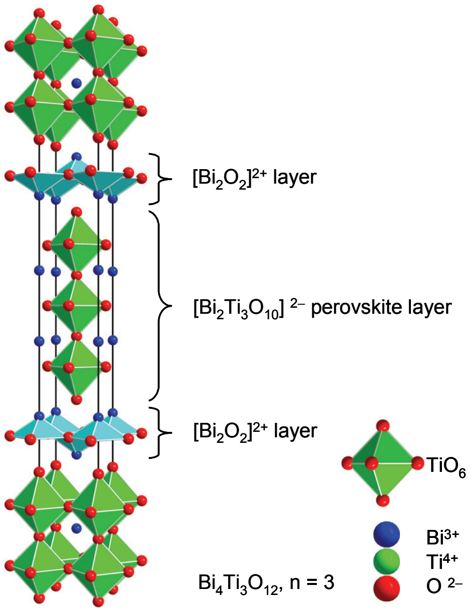

Fig 2.12 Illustration of bismuth layered perovskite structure.

A number of bismuth layered perovskite oxides have been found to show ferroelectricity. The compositions of these bismuth layered perovskites can be presented in a ternary phase diagram of $BiO_{1.5}$–$A^{x+}O_{x/2}$–$B^{y+}O_{y/2}$ according to the generic formula of $(Bi_2O_2)^{2+}(A_{n-1}B_nO_{3n+1})^{2-}$.[15] The perovskite phase ABO_3 is also shown in the phase diagram, which can be considered as the case of $n = +\infty$. It should be mentioned that any Bi^{3+} cations beyond 2 are considered as $A^{x+}O_{x/2}$. As seen in Fig 2.13, all the bismuth layered perovskite phases, from $n = 1$, to $n = +\infty$, are located on the line of Bi_2BO_6–ABO_3. A variety of the number n and possible ionic substitutions in the A-site and B-site of the perovskite units results in a huge number of ferroelectric compounds and solid solutions. Intergrowth between different members further increases the diversity. For example, $Bi_7Ti_4NbO_{21}$ has been reported a structure consisting of two parent phases, Bi_3TiNbO_9 ($m = 2$) and $Bi_4Ti_3O_{12}$ ($m = 3$), by sharing the 'Bi_2O_2' layers.[78, 79]

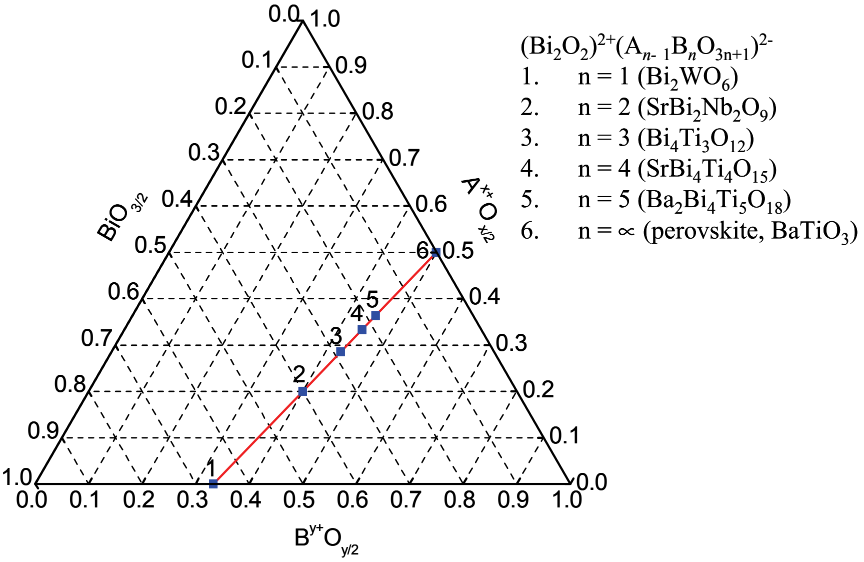

Fig 2.13 Ferroelectric compositions in the $BiO_{1.5}$–$A^{x+}O_{x/2}$–$B^{y+}O_{y/2}$ system.[15]

The Curie point, remanent polarization, and coercive field of the bismuth layered perovskite are listed in Table 2.4. The Curie point for a same material may be varied with heat treatment.[15] In the same series, the Curie point generally decreases with A-site cation in the order of $Ca^{2+} > Pb^{2+} > Sr^{2+} > Ba^{2+}$.[15] As seen in Table 2.4, the Curie point for the bismuth layered perovskites covers the range from 200 to 940 ºC, which renders those ferroelectrics of special interest for high temperature applications. Furthermore, most members of these materials are lead-free, offering another advantage over lead based ferroelectrics because of increasing environmental concern.

The major component of the large spontaneous polarization in bismuth layered perovskites has been attributed to the large displacements of the Bi^{3+} ions in the perovskite A-sites with respect to the chains of corner-sharing TiO_6 octahedra.[80] The displacement of the perovskite B-site octahedral cations (Ti^{4+}, Nb^{5+}, W^{6+}, etc) away from the center of their surrounding octahedron of oxygen atoms is not the predominant contribution to the ferroelectric polarization. This is not the case in the ferroelectric perovskites, where the ferroelectricity is mainly attributed to the displacement of octahedral cations (Ti^{4+}) away from the center of their surrounding octahedron of oxygen atoms.

$SrBi_2Ta_2O_9$ (SBT) is probably the first one of the most intensively studied bismuth layer-structured ferroelectrics (BLSFs) with $n = 2$ characterized by its excellent endurance, long retention time, and low leakage currents.[86] However, SBT has been criticized for its disadvantages of low remanent polarization and high processing temperature restricting practical applications.[23, 24, 28, 36, 87]

Ferroelectricity in $Bi_4Ti_3O_{12}$ (BLSFs, $n = 3$) single crystal and ceramic forms was first reported by Uitert and Egerton,[50] and Subbarao[51] respectively in 1961. The remanent polarization (P_r) of $Bi_4Ti_3O_{12}$ single crystals along the $c(a)$ axis (in *Aea*2, the standard setting of S.G. 41) was about 50 µC/cm^2 at room temperature.[16, 17] Low crystallization temperatures in between 500 and 650 °C were reported by different authors for the preparation of pure and substituted $Bi_4Ti_3O_{12}$ films.[18-20] The large spontaneous polarization and low processing temperature make $Bi_4Ti_3O_{12}$ more competitive than SBT for a lead-free ferroelectric material and has inspired intensive studies in the past decade.

Table 2.4 T_c, P_r, and E_c of bismuth layered perovskites $(Bi_2O_2)^{2+}(A_{n-1}B_nO_{3n+1})^{2-}$.*

n	Compounds	T_c: ºC	P_r: μC·cm^{-2}	E_c: kV·cm^{-1}	E_{max}: kV·cm^{-1}	Temp: ºC	Form
1	Bi_2WO_6	935	50	65	100	RT	S.C.†[81]
2	Bi_3TiNbO_9	940					
	Bi_3TiTaO_9	870					
	$CaBi_2Nb_2O_9$	625‡					
	$CaBi_2Ta_2O_9$	575					
	$PbBi_2Nb_2O_9$	550					
	$SrBi_2(V_xNb_{1-x})_2O_9$	435–456	3–8	40–63	~140		ceramic[82]
	$K_{0.5}Bi_{2.5}Nb_2O_9$	435					
	$PbBi_2Ta_2O_9$	430					
	$SrBi_2Ta_2O_9$	310	4–16				film[28]
	$BaBi_2Nb_2O_9$	200					
3	$Bi_4Ti_3O_{12}$	675	50				S.C.[16]
	$PbBi_3Ti_2NbO_{12}$	290					
	$BaBi_3Ti_2NbO_{12}$	270					
	$SrBi_3Ti_2NbO_{12}$	166	7	19		RT	ceramic[83]
4	$CaBi_4Ti_4O_{15}$	790					
	$Bi_5Ti_3FeO_{15}$	750					
	$Na_{0.5}Bi_{4.5}Ti_4O_{15}$	655					
	$PbBi_4Ti_4O_{15}$	570					
	$K_{0.5}Bi_{4.5}Ti_4O_{15}$	550					
	$SrBi_4Ti_4O_{15}$	530	29	26			S.C.[84]
	$BaBi_4Ti_4O_{15}$	395	15	32			S.C.[17]
5	$Bi_6Ti_3Fe_2O_{18}$	810					
	$(Pr,Bi)Bi_4Ti_3Fe_2O_{18}$	780					
	$Pr_2Bi_4Ti_3Fe_2O_{18}$	630					
	$Ba_2Bi_4Ti_5O_{18}$	329	12	31			S.C.[17]
	$Pb_2Bi_4Ti_5O_{18}$	310					
	$Sr_2Bi_4Ti_5O_{18}$	285					

* Values from Ref.[15] unless otherwise specified; †2 mol % Mn substitution at the W site; S.C.: single crystal; ‡Yan et al.[85] reported the T_c of $CaBi_2Nb_2O_9$ ceramic was 940 °C.

However, pure $Bi_4Ti_3O_{12}$ shows low remanent polarization (P_r),[21-24] high leakage,[21, 24-26] and polarization fatigue,[22] hindering its practical applications. Extensive studies have revealed that charged defects, especially oxygen vacancies, play a crucial role in the domain-wall pinning and polarization fatigue of the perovskite oxide ferroelectrics.[26, 27, 29, 61, 62, 88, 89] In the case of $Bi_4Ti_3O_{12}$, bismuth vacancies accompanied with oxygen vacancies in the perovskite layers have been suggested to be responsible for the domain-wall pinning, polarization fatigue, and high electrical leakage.[26-29]

Several strategies have been developed so far to suppress oxygen vacancies in the perovskite layers for improving the P_r and suppressing the polarization fatigue. Lanthanoid cations (La^{3+}, Pr^{3+}, Nd^{3+}, etc.) isovalent substitution for Bi^{3+} at perovskite A-site have been found to be an effective way to reduce bismuth vacancies and stabilize oxygen in the perovskite layers. The solid solution limit of $Bi_{3-x}Re_xTi_3O_{12}$, Re = La, Pr, Nd, etc. has been studied by Wolfe and Newnham,[90] in which the maximum of x has been found to excess 2 for Re = La, Pr. However, no special attention has been paid to these solid solutions until recently Park et al's report on the La^{3+} substituted $Bi_4Ti_3O_{12}$ thin films without notable polarization fatigue.[28] Shortly after, fatigue-free ferroelectric films with large P_r, above 30 μC/cm^2, have been reported in the oriented La^{3+} and Nd^{3+} substituted $Bi_4Ti_3O_{12}$ thin films.[30, 31]

On the other hand, donor (V^{5+}, Mo^{6+}, W^{6+}, etc.) aliovalent substitution for Ti^{4+} at perovskite B-site provides another strategy for compensation of the oxygen vacancies in $Bi_4Ti_3O_{12}$. The decrease of conductivity and coercive field with Nb^{5+} substitution for Ti^{4+} has been observed by Yi et al. in another member of bismuth layer-structured ferroelectrics, $PbBi_4Ti_4O_{15}$ single crystals.[91] Later Noguchi et al. found that V^{3+} and W^{6+} substitution for Ti^{4+} in $Bi_4Ti_3O_{12}$ ceramics effectively reduces the oxygen vacancies ($V_{\mathrm{O}}^{\cdot\cdot}$) and V_{Bi}'''-$V_{\mathrm{O}}^{\cdot\cdot}$ vacancy complexes that results in large P_r, over 20 μC/cm^2, and low leakage current.[23, 24]

The successful enhancement of P_r by A- or B-site substitution naturally incubates the third strategy, cosubstitution using lanthanoid cation and donor cation for both Bi^{3+} and Ti^{4+} at perovskite A- and B-site, respectively. Because the cosubstitution would be compatible in a $Bi_4Ti_3O_{12}$ structure to balance the charged defects and improve ferroelectric properties. The cosubstitution strategy was firstly reported by Watanabe et al. in La^{3+} and V^{5+} cosubstituted $Bi_4Ti_3O_{12}$ films,[92] which have ferroelectric properties superior to those of either monosubstituted films. Thereafter, a large number of lanthanoid cations (La^{3+}, Pr^{3+}, Nd^{3+}, Sm^{3+}, etc.) and donor (Nb^{5+}, V^{5+}, Mo^{6+}, W^{6+}, etc.) cosubstituted $Bi_4Ti_3O_{12}$ films have been reported by Uchida et al.[25, 35-37] and other authors[32-34].

2.2.3 Ferroelectric Fluorides

In contrast with ferroelectric oxides, ferroelectric fluorides are much less numerous. Proofs of ferroelectricity have been demonstrated only in the six families: $(NH_4)_2BeF_4$, $BaMnF_4$, $SrAlF_5$, Na_2MgAlF_7, $K_3Fe_5F_{15}$ and $Pb_5Cr_3F_{19}$,[93] which are listed Table 2.5.[93]

Table 2.5 Ferroelectric fluorides.[93]

Compound type	T_c (K)	Point Group	Main other compositions
$(NH_4)_2BeF_4$	175	mm2	
$BaMnF_4$		mm2	$BaMF_4$ (M = Mg, Fe, Co, Ni, Zn)
$SrAlF_5$	700	4	$SrMF_5$ (M = Cr, Ga), $BaMF_5$ (M = Ti, V, Fe)
Na_2MgAlF_7	725	4mm	Na_2NiMF_7 (M = Al, Fe)
$K_3Fe_5F_{15}$	490	mm2	
$Pb_5Cr_3F_{19}$	555	4mm	$Pb_5M_3F_{19}$ (M = Al, Ti, V, Fe, Ga)

Table 2.6 Polarization of BMF_4 compounds.[94]

Compounds	Polarization / μC·cm^{-2}	
	Theoretical	Experimental
$BaMgF_4$	8.5	7.7
$BaZnF_4$	11.7	9.7
$BaMnF_4$	13.9	11.5

$BaMgF_4$ is a member of the $BaMF_4$ (M = Mg, Co, Ni, Zn, Mn, Fe) family, which are bidimensional displacive ferroelectric up to their melting temperature with spontaneous polarization to 10 μC·cm^{-2},[93] however reversal of polarization for Mn and Fe has not been achieved.[94] The ferroelectric polarization originates from a shift of the Ba^{2+} cations along the *c*-polar axis of the orthorhombic unit cell through the rotation of corner-sharing octahedrons.[93] A comparison of theoretical and experimental polarization is shown in Table 2.6.[94] The optical constants of $BaMgF_4$ are given in Table 2.7 and Table 2.8.[95]

Bulk crystals of $BaMF_4$ compounds can be prepared by melting of corresponding metal fluorides in fluorine containing atmospheres (such as HF for $BaCoF_4$,[96] and CF_4 for $BaMgF_4$[97]). Preparation of nanoparticles of these compounds has not been reported before. The low refractive indices of $BaMgF_4$ are interesting for the preparation of transparent inorganic/polymer composites by mixing it with polymers of comparable refractive indices. In this case, large size particles can be used without loss of ferroelectricity (section 2.3). One of the main disadvantages of the ferroelectric fluorides may be the low spontaneous polarization.

Table 2.7 Optical properties of $BaMgF_4$.[95]

Transmission (μm)	Refractive indices			Birefringence
	n_x	n_y	n_z	Δn
0.185-10	1.4496	1.4661	1.4738	0.0242

Table 2.8 Dispersion of refractive indices of $BaMgF_4$.[95]

	Dispersion of refractive indices (0.53–1.06 μm)
n_x^2	$2.1462 + 0.00736\lambda^2 / (\lambda^2 - 0.0090)$
n_y^2	$2.007 + 0.0076\lambda^2 / (\lambda^2 - 0.00799)$
n_z^2	$2.1238 + 0.0086\lambda^2 / (\lambda^2 - 0)$

2.3 Nano Ferroelectrics

2.3.1 Quantum Confinement Effect

The quantum confinement effect exists in a system where the electron mean free path exceeds the dimensions of the crystal, which results in a quantum-mechanical increase in energy and the band gap.[9] This usually occurs in a high-mobility semiconductor. The commonly used perovskite structured ferroelectrics are wide-band-gap *p*-type materials ($3.0 < E_g < 4.5$ eV).[98] The typical electron mean free path in a perovskite ferroelectric is 0.1 – 1.0 nm depending on the applied electric field.[9] Therefore, quantum confinement is rarely measurable for a ferroelectric with dimensions above 20 nm.[9]

2.3.2 Size Effect

Ferroelectricity can been considered as a result from a delicate balance between long range Coulomb interaction and short range covalent repulsions.[99] As the grain size decreases into nano scale, the long range Coulomb interaction is altered due to a lack of periodicity. On the other hand, a decrease of grain size will cause an increase of the fraction of ions in the surface layer. Ions in a surface layer may have a different number of nearest neighbors from those in the bulk, thus the short range covalent interaction is modified. Therefore, in nano ferroelectrics, the balance is distorted with respect to the bulk. It is widely accepted that there is a critical size, below which ferroelectricity will vanish.[8]

In another point of view, ferroelectricity requires termination of the electric polarization at surfaces. This results in a discontinuity in the dielectric displacement div(P_s). In bulk ferroelectrics, the depolarization energy is reduced by forming “head-to-tail” domain configurations (Fig 2.14). In a nano ferroelectric, however, grain size may be smaller than a domain size that results in monodomain nanograins. Consequently, the spontaneous polarization must decay to eliminate the depolarization energy div(P_S) if the ferroelectric is an ideal insulator and not connected to an electrode.

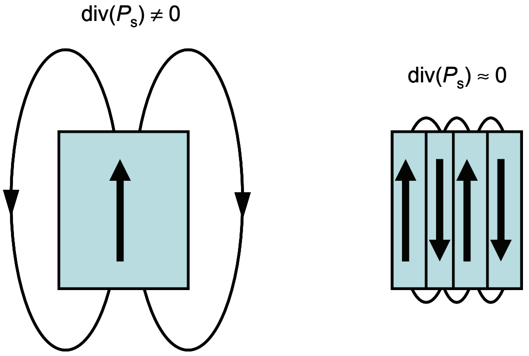

Fig 2.14 Elimination of depolarization energy through formation of "head-to-tail" domain patterns.[57]

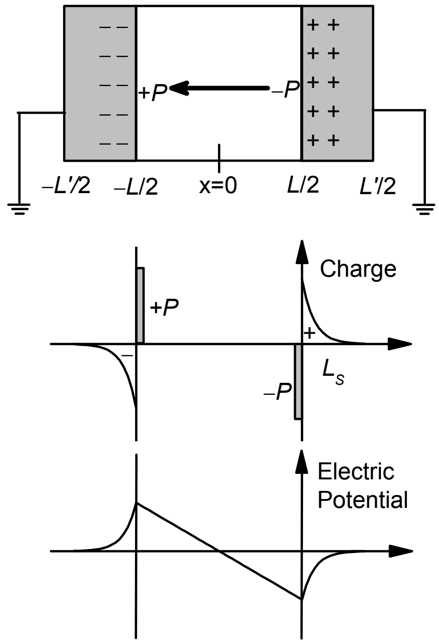

Fig 2.15 Schematic illustration of a short-circuit metal-ferroelectric-metal thin capacitor, and charge and electric potential distribution along the direction perpendicular to its electrodes considering the finite spatial electronic screening length in metal electrodes.[100]

Even if a ferroelectric has metal electrodes, the depolarization field may exist because the electric incomplete compensation of the ferroelectric polarization charge, which results from the finite electronic screening length in metals.[100] In a poled ferroelectric sandwiched between two electrodes as seen in Fig 2.15, Mehta et al.[100] reported that the depolarization field (E_{dep}) or electric field in the ferroelectric ($E_{\mathrm{F,x}}$) has the following relation with the thickness (L) under the short-circuit condition:

$$E_{\mathrm{F,x}} = E_{\mathrm{dep}} = -\frac{P}{\varepsilon_0 \varepsilon_{r,fe}} \cdot \frac{2\varepsilon_{r,\mathrm{fe}} / L}{2\varepsilon_{r,\mathrm{fe}} / L + \varepsilon_{\mathrm{E}} / L_S} \qquad \textbf{Eq 2.9}$$

Here ε_0 is the dielectric permittivity of vacuum, $\varepsilon_{r,fe}$ is the small signal (amplitude is much smaller than that required to switch remanent polarization in a ferroelectric capacitor) dielectric constant of the ferroelectric of interest, d is the thickness of the ferroelectric, and L_S is the screening length of the electrode that characterized the space-charge extent in the electrode. The relative dielectric constant of metal can be considered as unit for a free electron gas.[100, 101]

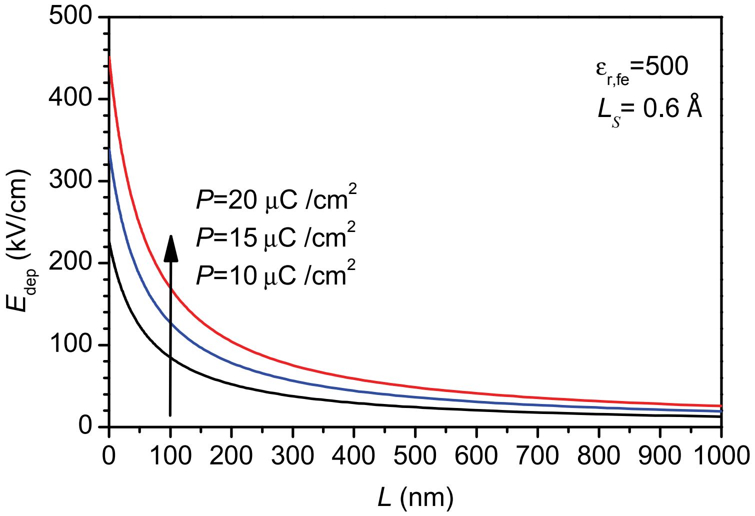

Fig 2.16 Depolarization field as a function of the thickness of a ferroelectric with different polarization.

For a ferroelectric with a small signal dielectric constant $\varepsilon_{r,fe}$ = 500, and screening length equals 0.6 Å as for gold electrodes, the depolarization field as a function of ferroelectric thickness with different polarization values calculated from Eq 2.9 are shown in Fig 2.16. It can be seen that the depolarization field becomes profound at a thickness below 100 nm, which has values above 80 kV/cm. It is worthy to mention that the space charge, as always exists in practical in the ferroelectric, is not considered. Such a high depolarization field may cause back switching of ferroelectric polarization and may destroy the ferroelectricity.[5] This depolarization instability could be a reason for the poor retention observed in thin ferroelectric films.[100]

2.4 Preparation Methods

Various methods have been developed so far for the preparation of different kinds of nanoparticles. However, templates, either soft or hard, are frequently used in almost all bottom-up methods to confine the particle growth (Fig 2.17), to avoid agglomeration, and to give a better control of the balances between nucleation, growth, and crystallization. The soft templates can be surfactants, chelating agents, charges, polymers, etc.,[102] while the hard templates can be a mesoporous matrix, such as mesoporous silica, porous carbon, and porous anodic alumina, etc.[103] The general strategy using templates to confine the particle growth is also applicable to synthesize ferroelectric nanoparticles.

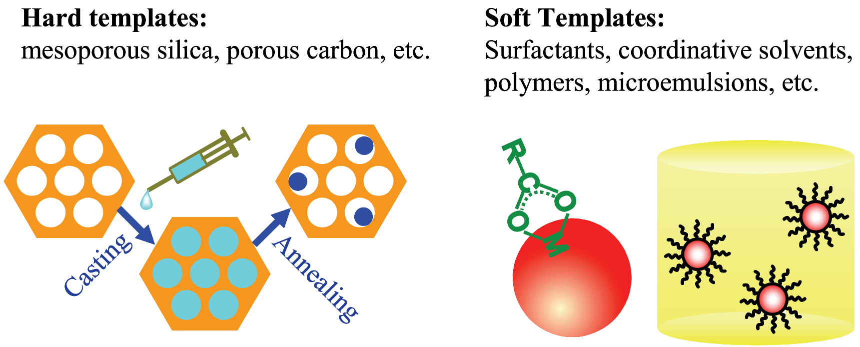

Fig 2.17 A general strategy to synthesize nanoparticles with size below 10 nm is using templates to confine the particle growth.

2.4.1 Coprecipitation

Coprecipitation synthesis is one of the simplest chemical methods in which insoluble compounds (e.g., hydroxides, oxalates, etc.) are precipitated from a solution of metal salts (e.g., nitrates, acetates, or chlorides, etc) with precipitating agents (such as NaOH(aq), NH_3(aq)), and the desired nanoparticles are obtained directly or after calcination of the precipitates.[104]

Flaschen has reported a coprecipitation method in 1955 for the preparation of crystalline $BaTiO_3$ particles with size from 1 to 5 µm, through dropwise adding a dilute propyl alcohol solution of a titanium ester such as tetrapropyltitanate or an ester of a higher alcohol to a degassed water solution of barium hydroxide at a temperature above 80 °C.[105] An analogous method was recently reported by Qi et al. to prepare $Ba_{0.9}Sr_{0.1}TiO_3$ nanoparticles with size about 50 nm.[106] The as-synthesized $Ba_{0.9}Sr_{0.1}TiO_3$ nanoparticles have the cubic structure up to 1000 °C in Qi et al's report. Oxalate coprecipitation has been extensively study for synthesis of $BaTiO_3$ nanoparticles, where mixed barium and titanium oxalates (BaC_2O_4 and $TiOC_2O_4$) are formed by coprecipitation using aqueous, ethanolic, or methanolic solution of oxalic acid as precipitating agent.[107] Upon calcination, the mixed oxalates are subsequently converted into several intermediates, including a barium titanium oxycarbonate ($Ba_2Ti_2O_5CO_3$), the so called BTC phase.[107] The latter decomposes into $BaTiO_3$ and CO_2 above 550 °C. The average size of the primary particles of derived $BaTiO_3$ is about 50–250 nm depending on the calcination temperature.[107]

Besides water, nonaqueous solvents have also been used in coprecipitation methods. An injection-hydrolysis method reported by O'Brien et al. can be considered as a variant of coprecipitation methods,[12] where hydrogen peroxide solution was injected into a diphenyl ether ($(C_5H_5)_2O$) solution containing barium titanium ethyl hexano-isopropoxide and oleic acid at 100 °C to form well isolated monodispersed 4 to 12 nm $BaTiO_3$ nanocrystals. Here the diphenyl ether and oleic acid may function as soft templates to confine the growth and to stabilize the particles. However, in this method the vigorous exothermic reaction may cause explosion as the strong oxidant, H_2O_2, is introduced into the reductive organic solution. Recently, Siemons et al. reported a polyol-mediated coprecipitation method to prepare a large number of nanosized perovskite oxides, including $BaTiO_3$, $SrTiO_3$, and $PbTiO_3$,[108] where coprecipitation occurred in diethylene glycol solution of metal salts and nano perovskite oxides with size from 30 to 80 nm were obtained from calcination of the precipitates at 700 °C. The diethylene glycol serves as both solvent and soft template during the hydrolysis induced precipitation stage.[109]

Du et al.[110] have prepared $Bi_4Ti_3O_{12}$ nanoparticles by a coprecipitation method. In this method, $TiO_2 \cdot xH_2O$ was prepared by hydrolysis of $(C_4H_9O)_4Ti$ with water and dissolved in ammonia water with H_2O_2 to obtain a $(NH_4)_2TiO_4$ solution. The latter was slowly poured into a $Bi(NO_3)_3$ acid solution for coprecipitation. Well-crystalline $Bi_4Ti_3O_{12}$ nanoparticles were obtained from the calcination of the coprecipitates at 500 °C for 1 h.

The advantage of coprecipitation technique over conventional solid-state reaction methods is that intimate mixing of the precursors in the solution phase leads to lower calcination temperatures and the preparation of high purity and fine particle size powders (500 nm, after calcination and milling).[104] Drawbacks are the agglomeration of fine particles formed in the calcination step and the unavoidable contaminations from the coprecipitation process (such as Na^+, chlorides, carbonates, etc.).

2.4.2 Microemulsion Precipitation

The synthesis of multicomponent oxides from reverse micelles is similar in most respects to the coprecipitation in aqueous solutions, which relies on the coprecipitation of one or more metal ions.[109] Typically, precipitation of hydroxides is induced by either direct addition of dilute NH_4OH or by addition of a reverse micelle solution containing dilute NH_4OH to a reverse micelle solution containing aqueous metal ions at the micellar cores. The reverse micelles serve as nanoreactors and the nanoparticle size can be controlled by the water content.[111] A larger number of metal nanoparticles (such as Co, Ni, Cu, etc.) and simple oxides (Fe_3O_4, etc.) can be directly obtained at ambient condition. However, in most cases, further annealing at high temperature are needed for synthesis of multicomponent oxide nanoparticles.[109]

More than ten years ago, Herrig and Hempelmann[10, 11] have developed a microemulsion method, based on the hydrolysis of alcoholic alkoxide solution with a microemulsion containing water (50 µl)/Brij90 (6 g)/cyclohexane (36 ml), to prepare binary metal oxide (TiO_2, ZrO_2) and ternary metal oxide ($BaTiO_3$, $BaZrO_3$, $SrTiO_3$, $SrZrO_3$,) nanoparticle. The average crystallite size is about 9 and 18 nm for $BaTiO_3$ and $SrTiO_3$. The $BaTiO_3$ and $SrTiO_3$ nanoparticles were crystallized without calcination that may be the first low temperature preparation of well crystallized $BaTiO_3$ and $SrTiO_3$ nanoparticles using the microemulsion method. This method has been recently well repeated by Sakabe et al.[112] and Pithan et al.[113] to prepare $BaTiO_3$ nanoparticles with average size of 8–10 nm using other microemulsion systems (water/NP10/octanol/cyclohexane, NP35 is used as surfactant for the latter).

$BaZrO_3$ nanoparticles with a mean size of 17 nm have been reported by Leonard et al.[114] using a microemulsion precipitation method, where an aqueous solution of $Ba(NO_3)_2$ and $ZrO(NO_3)_2$, *n*-octane, cetyltrimethylammonium bromide (CTAB), and 1-butanol were used as the water phase, the continuous oil phase, the surfactant, the cosurfactant, respectively. Precipitation was induced by mixing with another microemulsion of similar composition using NaOH (aq). The precipitates were amorphous products containing $Ba(OH)_2(H_2O)_3$ and $Zr_{0.95}O_2$ phases and were found to crystallize into $BaZrO_3$ phase at 700 °C.

Xie et al.[115] have synthesized $Bi_4Ti_3O_{12}$ nanoparticles by chemical reactions between microemulsions containing bismuth nitrate pentahydrate and titanium sulfate (microemulsion I) and ammonia solution (microemulsion II) using a reverse microemulsion system consisting of water, *P*-octyl polyethylene glycol phenylether (surfactant), *n*-butanol (co-surfactant), and cyclohexane (oil). Precursor hydroxides precipitated in the droplets of water-in-oil microemulsion were calcined at 800 °C for 4 h to form nanoparticles of $Bi_4Ti_3O_{12}$ phase. However, the product calcined at 800 °C for 1 and 2 h contained $Bi_2Ti_2O_7$

and $Bi_{20}TiO_{32}$ impurity phases. The product calcined at 800 °C for 4 h was agglomerated nanoparticles with size of 35 nm as observed by TEM. The agglomeration of the product might be caused by the long time calcination at a high temperature.

The microemulsion precipitation method provides a particular advantage of preventing agglomeration of the particles and simply controlling the particle size by variation of water content. However, the main challenge for the preparation of multicomponent oxides may result from the different precipitation rates of the metal species in the microemulsion system, being problematic for the control of phase purity. Another disadvantage of the microemulsion precipitation method may be the low yield with sacrifice of huge quantity of surfactants and solvents.

2.4.3 Hydrothermal Synthesis

Hydrothermal synthesis is referred to as a synthesis by chemical reactions in a sealed vessel (bomb, autoclave, etc.) using water as solvent at temperatures well above its boiling points by the increase in autogenous pressures resulting from heating.[109] In the case of nonaqueous solvent, it is widely referred to as a solvothermal synthesis. It is worthy to mention that broad meaning of hydrothermal is frequently used in both solvothermal and hydrothermal cases as defined above.[116, 117] At hydrothermal conditions, the physical and chemical properties of water are remarkably different from those at ambient condition. The ion product increases with pressure and temperature, the viscosity decreases with temperature, whereas the dielectric constant decreases with rising temperature and increases with rising presure.[118]

Hydrothermal synthesis of $BaTiO_3$ ferroelectric materials has been extensively studied. Commonly aqueous solutions of $Ba(OH)_2 \cdot 8H_2O$[119-122] or $BaCl_2$[119, 123] are used as Ba-source. Ti-source is typically TiO_2[119-122] or $TiO_2 \cdot xH_2O$ gel. The latter can be prepared by precipitation from solutions containing the corresponding metal salts or alkoxides, such as $TiCl_4$,[122, 123] and Ti-butoxide[120, 121]. An aqueous solution of NaOH or KOH are frequently used as mineralizers.[113] The ferroelectric tetragonal $BaTiO_3$ particles with size about 1 μm were hydrothermal synthesized by Dutta et al.[119] from mixtures of $BaCl_2$, NaOH and TiO_2 in water at 200 °C. The absence of Cl^- ions resulted in only the cubic $BaTiO_3$. Xia et al.[120, 121] attributed the cubic phase of the hydrothermal synthesized $BaTiO_3$ to the presence of internal hydroxyl groups in the $BaTiO_3$ solid. The typical crystallite size of hydrothermal synthesized $BaTiO_3$ is from 20 to several hundreds nanometer. The crystallite size can be decreased by using coordinating solvents or surfactants as soft templates to confine the particles growth. Niederberger et al.[13, 14] have synthesized sub-10 nm sized $BaTiO_3$, $SrTiO_3$, and $(Ba,Sr)TiO_3$ nanoparticles using the alkaline earth metals barium and strontium together with titanium alkoxides in benzyl alcohol under subsolvothermal conditions (200–220 °C). The synthesis involves C-C bond formation between the benzyl alcohol and the isopropanolate of the titanium alkoxide. The small particles size has been attributed to these alcohols of unhydrolyzed Ti-O-R groups covering the surface of as-grown particles.[14] More recently, Wang et al.[102] developed a novel general strategy to synthesize a large variety of nanocrystals based on the phase transfer and separation mechanism occurring at the interfaces of the liquid–solid–solution. Using NaOH, $Ba(NO_3)_2$ and $TiCl_3$ as starting materials, Wang et al.[102] have successfully synthesized $BaTiO_3$ nanocrystals with size of 17 nm.

There are also reports on the hydrothermal synthesis of $Bi_4Ti_3O_{12}$ particles. However, hydrothermal synthesis of isolated $Bi_4Ti_3O_{12}$ nanoparticles with size below 100 nm still remains a challenge. The reported particle size was ranged from 100 nm to micrometers. $Bi(NO_3)_3·5H_2O$ is commonly used for Bi-source, and the typical Ti-source is $TiO_2·xH_2O$ gel precipitated from solutions containing the corresponding metal salts or alkoxides.[124-127]

The advantage of hydrothermal synthesis is that desired crystalline materials can be prepared at a low crystallization temperature without significant agglomeration. The drawbacks may be the difficulty of monitoring the reaction during the synthesis and the formation of unpredicted products.[128]

2.4.4 Aqueous Citrate-Gel Method

The aqueous citrate-gel method uses citric acid and metal salts to form aqueous soluble complexes.[129] Dehydration of the transparent metal complexes solution yields an amorphous gel that can be crystallized to the target compound after high temperature calcination. The citric acid can be substituted with other polyfunctional hydroxy acids, among which ethylenediaminetetraacetic acid (EDTA) is a well known one.[129] The high chelating ability of EDTA can minimize the segregation of precipitates resulting from the low solubility of the starting chemicals or any other intermediate compounds.[129]

The citrate-gel method has been used to synthesize a large number of multicomponent ceramics and ceramic films.[129, 130] Dhage et al. have used a citrate-gel method for the synthesis of $Bi_4Ti_3O_{12}$,[131] in which Bi_2O_3 was dissolved in hydrochloric acid, and was mixed with citric acid and $TiOCl_2$ (formed by hydrolysis of $TiCl_4$) to obtain the precursor solution. An analogous process has been used by authors from the same research group for the synthesis of $(Ba, Ca)_4Bi_4Ti_4O_{15}$,[132, 133] $(Ba, Ca)Bi_2(Nb, Ta)_2O_6$[134, 135] and $BaNb_2O_9$[136]. However, the formation of $Bi_4Ti_3O_{12}$ was observed at a temperature as high as 700 °C, and the remanent polarization P_r of the $Bi_4Ti_3O_{12}$ ceramics sintered at 1000 °C was 4.0 $\mu C/cm^2$.[131] The latter could be a result of the residual chlorine ions, which will form charged defects in the sintered ceramics. Therefore, using other kind of metal salts instead of halides is preferred to avoid halide ion contamination and to obtain a high remanent polarization. Sale[129] has used EDTA in a similar process to the citrate-gel method to prepare lead zirconate titanate (PZT), in which the use of nitrates instead of chlorides as the starting materials are important to obtain pure PZT at a low calcination temperature. The nitrate solutions of Zr and Ti were prepared separately by dissolving zirconium and titanium hydroxides in nitric acid. Using nitrates as starting materials, the XRD peaks belonging to the PZT phase were clearly observed after calcination at a temperature as low as 320 °C. Pure PZT was obtained after calcination at 600 °C. However, the desired PZT phase was not formed even after calcination at 1000 °C for 1 h when the chlorides were used as starting materials.

Simões et al.[137] have prepared pure and Nb^{5+} substituted $Bi_4Ti_3O_{12}$ ceramics using a polymeric precursor method, (so called Pechini method[138]). The precursor solutions of bismuth, titanium, and niobium were prepared by adding titanium isopropoxide, niobium (V) oxide, and bismuth nitrate, respectively, to ethylene glycol and concentrate aqueous citric acid. Solutions of Ti-, Bi- (5 wt% excess) and Nb-precursors were mixed and homogenized by stirring at 90 °C for 3 h and then heated up to 130–140 °C, yielding a highly viscous polyester resin. The latter was decomposed at 400 °C for 3 h and heated at 750 °C for 4 h to obtain powder. However, the P–E hysteresis loops were not saturated for both pure and Nb^{5+} substituted $Bi_4Ti_3O_{12}$ ceramics sintered at 1000 °C for 4 h, in which the remanent polarization was below 0.75 $\mu C/cm^2$.[137] Chu et al.[139] have synthesized $SrBi_4Ti_4O_{15}$ by a citrate-gel method using $Sr(NO_3)_2$, $Bi(NO_3)_3·5H_2O$, $(C_4H_9O)_4Ti$, citric acid, and ammonia water as starting materials. The $SrBi_4Ti_4O_{15}$ phase was formed after calcination of the gel at

550 °C for 2 h. The $2P_r$ and E_c for the $SrBi_4Ti_4O_{15}$ ceramic sintered at 1060 °C for 1 h were 16 μC/cm^2 and 43 kV/cm, respectively, measured at 180 °C with E_{max} of 80 kV/cm.

The citrate-gel method has several advantages over other chemical solution techniques in terms of preparation of multicomponent materials regarding the use of water as solvent, providing more homogeneous mixing, and giving better stoichiometric control (without filtering step), etc. However, in sol-gel[130] and metalorganic decomposition methods,[140] 2-methoxyethanol, a toxic solvent, has been widely used. As far as coprecipitation and hydrothermal methods are concerned, it is more difficult to find suitable conditions for the preparation of the desired products if the number of components with different solubility increases. The main drawback of the citrate-gel method is the agglomeration of particles formed in the high temperature calcination.

3. Characterization Techniques and Experimental Details

This chapter provides various basic principles of characterization techniques and experimental details involved in this dissertation. The characterizations include phase analysis using X-ray diffraction (XRD), pyrolysis analysis using (TG-DSC), morphology characterization using SEM and TEM, composition analysis using EDS, ferroelectric characterization using virtual ground Sawyer-Tower circuit.

3.1. X-ray Diffraction

X-ray diffraction (XRD) is widely used for structure, phase, and texture analysis. Phase identification using XRD mainly based on the diffraction peak positions according to well-known Bragg's law, and to some extent on the relative peak intensities.

The relative peak intensities can be used for texture analysis. Texture effect is referred to as the grains in a polycrystalline material are aligned in a preferred orientation along certain lattice planes. Therefore, the texture of a polycrystalline material is defined by the orientation distribution of the crystalline grains. A textured material can be considered as an intermediate state between a randomly oriented polycrystalline powder and an aligned single crystal. The ratio of diffraction peak intensities may be changed when there is texture effect.

Moreover, the shape of the diffraction peaks may also contain valuable information, about the crystallite size. The relationship between crystallite size and peak broadening can be expressed by the Scherrer equation:

$$L_{\mathrm{vol}} = \frac{K \cdot \lambda}{\beta_{\mathrm{size}} \cdot \cos\theta} \qquad \textbf{Eq 3.1}$$

Here L_{vol} is volume-weighted apparent crystallite size, K is the Scherrer constant, λ is the wavelength of the radiation, β_{size} is the peak broadening in radians due to small crystallite size, and θ is the diffraction angle. The value of K depends on crystallite shape and on the type of breadth used. Both the full-width-at-half-maximum (FWHM) and integral breadth (defined as the total area under the peak (above background) divided by the peak height) have been used for measuring the peak broadening, however, different K values should be considered.[141]

3.2 Electron Microscopy[142, 143]

Electron microscopic techniques, including stationary beam methods: transmission electron microscopy (TEM) and scanning beam methods: scanning electron microscopy (SEM), are the most popular of techniques for the characterization of nanomaterials concerning the morphology (shape, size), crystal structure, microstructure, composition, etc.

3.2.1 Interactions between Electrons and Specimen

In an isolated atom, the positive charged nucleus is surrounded by a number of negative electrons that yields neutralization in charge. In a solid consisting of compacted atoms, inner shell electrons, usually in the K or L shell, are nearest to the nucleus. They are localized and have the lowest energy. Outer electrons in the outermost occupied shell have the highest energy electrons and have the lowest bonding energies. Electrons in the conduction band are shared outer electrons, which are delocalized with a range of possible energies. Outer electrons are readily detached from their atoms since only a small amount of energy is needed. There are various possible interactions between high energy electrons and the atoms in a thin specimen (Fig 3.1).

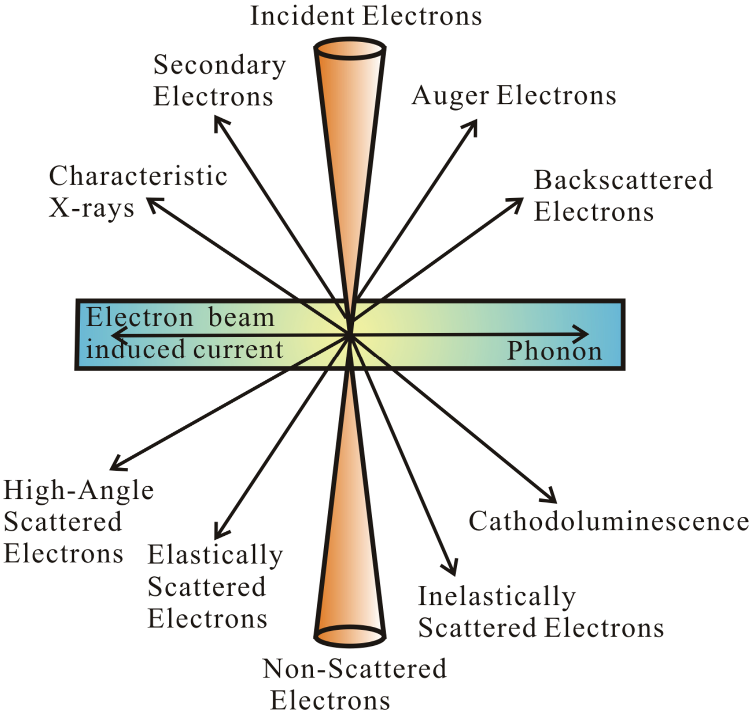

Fig 3.1 Possible interaction between a high-energy electron beam and a thin specimen.[144]

3.2.1.1 Elastic Scattering

Elastic scattering is a process characterized by no detectable change in energy, although the direction of the primary electron might be changed. The elastic scattering results from Columbic interactions between the primary electron and both nucleus and all the surrounding electrons, which is known as Rutherford scattering:[143]

$$p(\theta)\propto\frac{1}{E_0^2\sin^4(\theta)} \qquad \textbf{Eq 3.2}$$

Here $p(\theta)$ is the probability of electron being scattered through an angle θ, E_0 is the energy of the primary electron. Elastic scattering has the main contribution to electron diffraction patterns, since it is a major mechanism by which electrons are deflected.

3.2.1.2 Inelastic Scattering

Inelastic scattering refers to any process where the primary electrons have a detectable loss of energy. In the inelastic scattering, almost all of the lost energy contributes to heat. A small proportion of the energy releases as X-ray, light, or secondary electrons, which are extremely useful for both imaging and elemental analysis.

3.2.1.3 Secondary Electrons

Secondary electrons are referred to as those electrons with energy in the range of 0–50 eV that are emitted from the specimen under electron irradiation. Secondary electrons are commonly used for imaging in SEM, because they carry information about the surface of the specimen, including morphology, chemistry, and both magnetic and electric fields, etc. Moreover, secondary electrons are easy to be collected and the secondary electron images can have a spatial resolution of 1.0 nm or better under properly optimized conditions.

3.2.1.4 Backscattered Electrons

Backscattered electrons are defined as some electrons that are emitted from the specimen with energy in the range from 50 eV to the incident beam energy E_0. Usually backscattered electrons are fewer than secondary electrons. Before they leave the specimen, backscattered electrons have been scattered through angles approaching 180° within the specimen.

The yield of backscattered electrons differs between atoms with different atomic number. Therefore, the backscattered electrons can be used for Z-contrast imaging to qualitatively analyze the chemical distribution of high and low atomic number elements within the specimen of interest. Furthermore, the backscattered electrons emerge from a volume about one third of the incident beam range in depth and radium, where for a first approximation, the range R (in nm) is given by[142]

$$R = \frac{75E_0^{5/3}}{\rho} \qquad \textbf{Eq 3.3}$$

Here E_0 is the incident beam energy in keV and ρ is the density of the specimen in g cm^{-3}. Supposing the energy of incident electrons is 10 keV, the backscattered electrons come from a region in the order of a fraction of one µm or more in both depth and width. Therefore, the backscattered electrons contain information of interior of the specimen and can be used for imaging the buried particles, voids, or cracks.

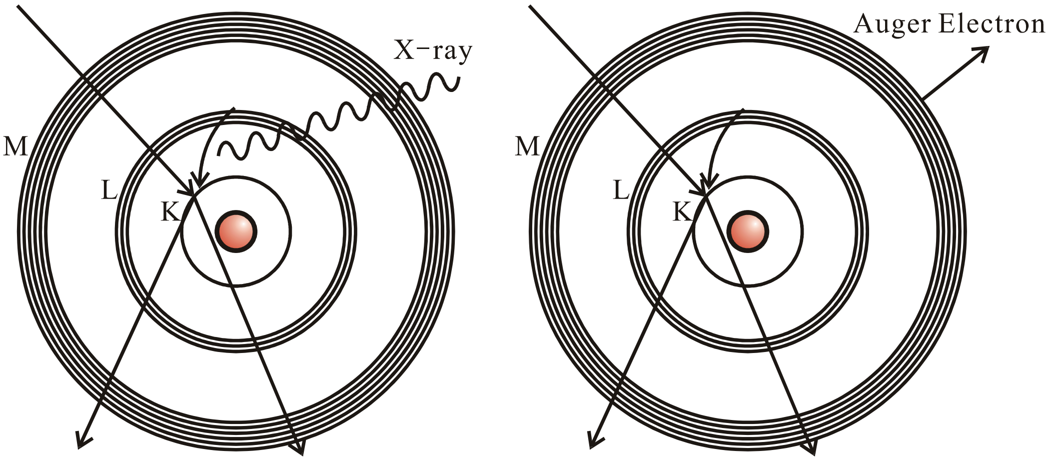

Fig 3.2 Relaxation of inner-shell-excited atom by emission of characteristic X-ray (left) and Auger electron (right).[143]

3.2.1.5 Relaxation Processes

If a shell electron is ejected from an atom of the specimen, the latter is ionized and is in an excited high energy state. The empty electron state formed will be filled by an electron from one of the outer levels via relaxation processes, which are essentially in three ways: cathodoluminescence, X-ray emission, and Auger electron emission. The energy is emitted in the form of a photon that is known as cathodoluminescence if the vacant electron state is an outer state, since the energy to be given off will be small. The energy difference by filling an electron vacancy formed by ionization of an inner shell electron can be emitted either as a characteristic X-ray quantum or as an Auger electron, as illustrated in Fig 3.2. The energy of emitted characteristic X-ray can be depicted by Moseley's law:[145]

$$E = B\,(\mathrm{Z}\text{-}1)^2 \qquad \textbf{Eq 3.4}$$

Here B is constant within K, L, and M series, and Z is the atomic number of the element of interest. This lays the foundation for the energy (or wavelength) dispersive spectroscopy (EDS, or WDS), which can be used for microanalysis and X-ray mapping. The Auger electron can also be used for Scanning Auger microscopy (SAM) for microanalysis.

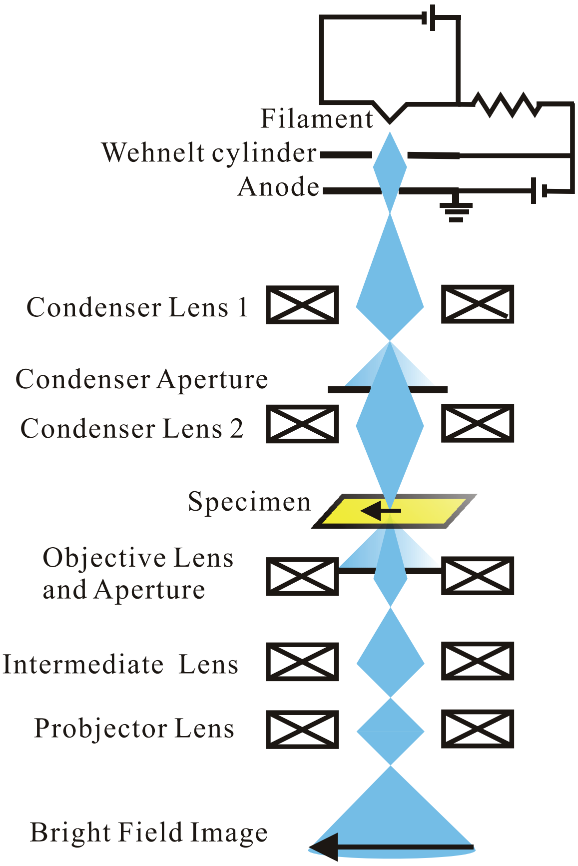

Fig 3.3 Principle of a transmission electron microscope.

3.2.2 Transmission Electron Microscopy

The study of the real structure and morphology evolution of crystalline materials is a prerequisite to understand the processes of crystal growth, thereby clarifying the correlated physical properties. Transmission electron microscopy (TEM), especially high-resolution transmission electron microscopy (HRTEM), is one of the most powerful and indispensable tools used for characterizing nanomaterials.[146] It allows to obtain structural information down to atomic resolution and to correlate it directly to chemical and physical properties.

TEM is an imaging technique where a beam of electrons is focused onto a thin specimen resulting in an enlarged image to be recorded on a fluorescent screen, a layer of photographic film, or a digital camera.[147] The structure of a transmission electron microscope is schematically represented in Fig 3.3. An electron gun, a source of a fine beam of high energy electrons, is prerequisite in every electron microscope. Smallest beam diameter is needed for the best resolution in many applications. Control of the spot size and beam convergence is achieved using condenser lenses and a condenser aperture. An aperture can be inserted into the back focal plane of the objective lens. Therefore, either the direct electrons or some scattered electrons are allowed to go through by moving the aperture. The direct beam results in a bright-field image, and any form of scattered electrons yield a dark-field image.[147]

3.2.3 Scanning Electron Microscopy

As seen in Fig 3.4, a scanning electron microscope is analogous to transmission electron microscope, where a fine beam of high energy electrons is produced by an electron gun. The electron beam is controlled using condenser lenses and a condenser aperture. The main difference to the latter is the electron beam passes through scanning coils in the objective lens that deflect the beam in a raster fashion over a rectangular area of the sample surface. Upon striking the surface of the specimen, the primary electrons are inelastically scattered by atoms. Consequently, the primary electron beam effectively spreads and fills a teardrop-shaped volume that extends less than 100–5000 nm into the surface.[147] Interactions in this region lead to the subsequent emission of secondary electrons, backscattered electrons, Auger electrons, and characteristic X-ray, as discussed in section 3.2.1, which are then detected for SEM imaging, and for EDS, WDS, or SAM microanalysis.

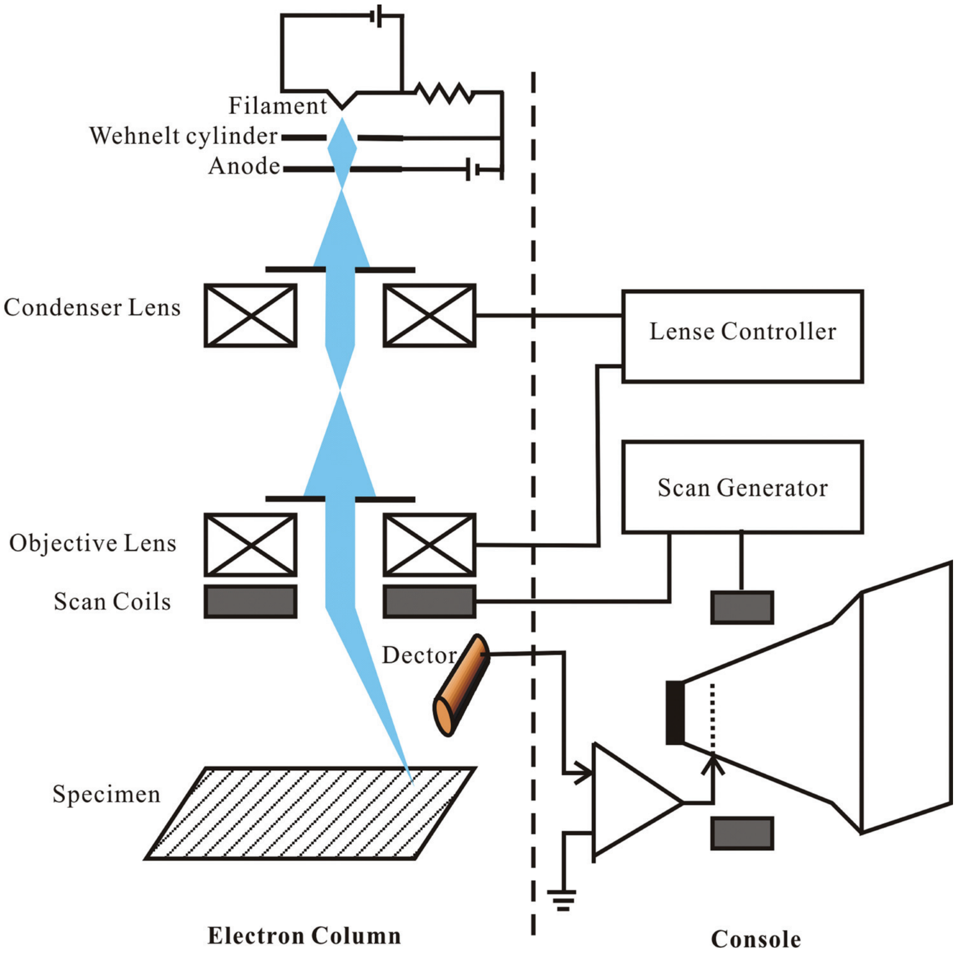

Fig 3.4 Schematic representation of a scanning electron microscope.

3.3 Electrical Characterization

3.3.1 Measurement Methods

Ferroelectric materials are characterized by their switchable spontaneous polarization and *P–E* hysteresis loops. Several techniques have been developed so far to study the polarization reorientation and to observe the hysteresis loop. Shunt, Sawyer–Tower, and virtual ground methods are well known techniques to record hysteresis loops of ferroelectric capacitors by measuring the current response.[148]

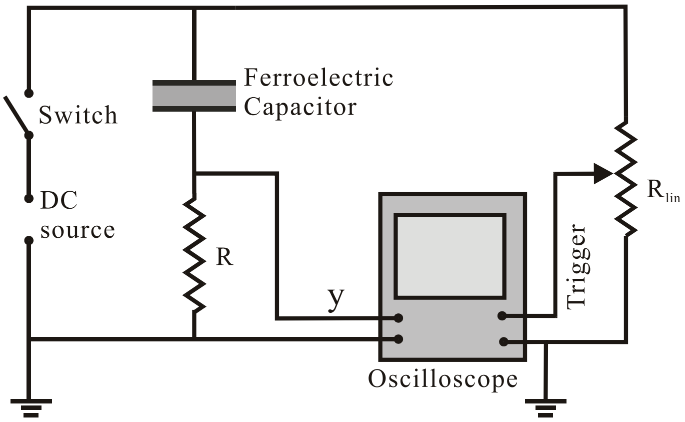

Fig 3.5 Merz circuit for measuring switching current in a ferroelectric capacitor.

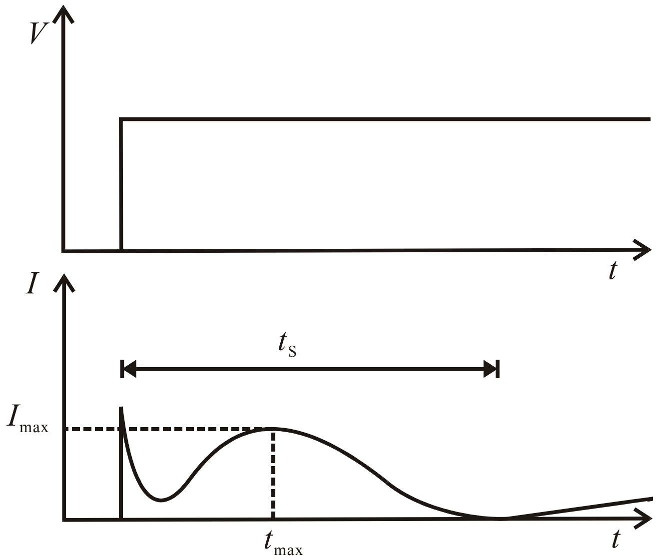

Fig 3.6 Typical voltage and current traces measured using Merz circuit.

3.3.1.1 Shunt Method

The shunt method, using Merz circuit named after the inventor, is a current based method, which allows measuring the switching current as a voltage drop across the shunt resistor ($V = RI$) (seen in Fig 3.5).[41, 148] The polarization is obtained by integration of the antiparallel domain switching current $2P_r = \int I(t)dt$. Assume a dc field pulse with rise time much shorter than the response of the ferroelectric capacitor, the sample first responds as a normal dielectric which has the time constant RC, which is followed by ferroelectric polarization reversal.[148] The typical shape of the switching current is shown in Fig 3.6, which is characterized by $i_{\max}$, $t_{\max}$, and t_S.[41]

It was experimentally found that $i_{\max}$ and $t_{\max}$ depend on the field according Eq 3.5 for low fields.[41]

$$i_{\max} \infty \frac{1}{t_S} = \frac{1}{t_\infty} \exp(\frac{-\alpha}{E}) \qquad \textbf{Eq 3.5}$$

Here t_∞ is a constant, and α is referred to as the activation field.

3.3.1.2 Sawyer–Tower Circuit Method

Sawyer–Tower circuit method is a charge based measurement method using a reference capacitor in series with the ferroelectric capacitor (Fig 3.7),[149] which is based on a law of electrical circuits that for two capacitors in series the charge on both must be equal. The ac drive source is typically a sine or triangular wave form voltage.[41] The shape of hysteresis loops measured by the Sawyer–Tower circuit usually depend on both the frequency and amplitude of the applied drive voltage wave.[41] High saturated hysteresis loops are normally obtained at high voltage wave amplitudes with peak fields at least three times the coercive field, $3E_c$.[41]

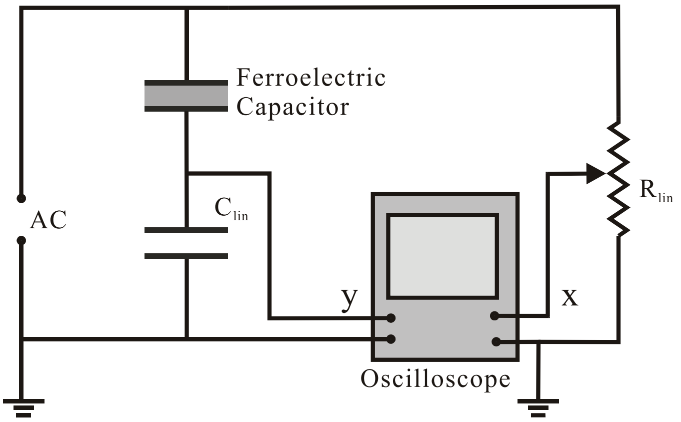

Fig 3.7 Sawyer–Tower circuit for measuring *P–E* hysteresis loops in a ferroelectric capacitor.

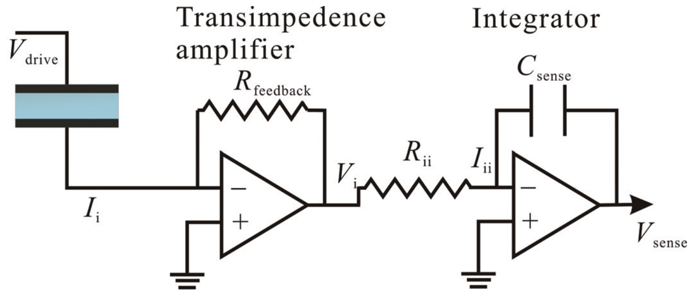

Fig 3.8 Radiant virtual ground circuit.

3.3.1.3 Virtual Ground Method

The virtual ground method uses a transimpedence amplifier converting a current to voltage, which is based on current measurement using a feedback resistor across an operational amplifier (Fig 3.8).

The output voltage of the transimpedence amplifier has linear relationship with the input current (Eq 3.6).

$$I_{\mathrm{i}} = \frac{-V_{\mathrm{i}}}{R_{\mathrm{feedback}}} \qquad \textbf{Eq 3.6}$$

The output voltage (V_{sense}) of the integrator is expressed as

$$V_{\mathrm{sense}} = -\frac{1}{R_{\mathrm{ii}} C_{\mathrm{sense}}} \int V_{\mathrm{i}} dt \qquad \textbf{Eq 3.7}$$

Combination of Eq 3.6 and 3.7 yields

$$V_{\mathrm{sense}} = \frac{R_{\mathrm{feedback}}}{R_{\mathrm{ii}} C_{\mathrm{sense}}} \int I_{\mathrm{i}} dt = \frac{R_{\mathrm{feedback}}}{R_{\mathrm{ii}} C_{\mathrm{sense}}} Q(t) \qquad \textbf{Eq 3.8}$$

When R_{feedback} equals R_{ii}, Eq 3.8 can be simplified as

$$V_{\mathrm{sense}} = \frac{1}{C_{\mathrm{sense}}} Q(t) \qquad \textbf{Eq 3.9}$$

Therefore, the polarization during the switching of a ferroelectric capacitor with high resistivity can be derived as Eq 3.10, where P is the polarization and A is the area of the ferroelectric capacitor.

$$P(t) = \frac{Q(t)}{A} = \frac{V_{\mathrm{sense}} C_{\mathrm{sense}}}{A} \qquad \textbf{Eq 3.10}$$

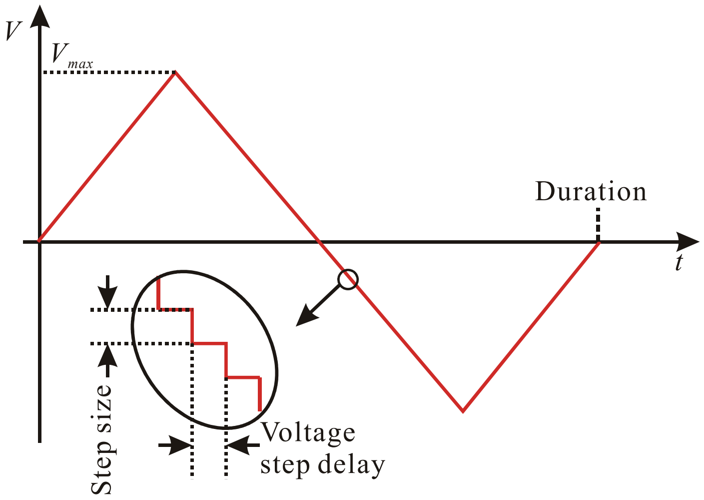

Fig 3.9 Standard bipolar triangular drive voltage waveform for *P–E* hysteresis loop measurement.

3.3.2 Measurement Types

3.3.2.1 *P–E* Hysteresis Loop

The *P–E* hysteresis loop measurement is a direct way to characterize ferroelectric properties. The drive voltage waveform is normally a standard bipolar triangular waveform that is simply defined by the maximum voltage (V_{max}) and the entire duration of the waveform (or frequency). The drive waveform contains a series of voltage steps (Fig 3.9). At each voltage step, the current induced in the sample by the voltage step is integrated and converted into polarization according Eq 3.10.

3.3.2.2 *I*/*V* Measurement

Current vs. voltage (*I*/*V*) measurements provide a series of leakage current values as a function of the voltage, which is stepped from point to point along a voltage profile (Fig 3.10). The *I*/*V* measurements can be performed in a switching or non-switching type, which can be defined using a preset pulse. Non-switching type is used to exclude the possible contribution of domain switching to the leakage current.

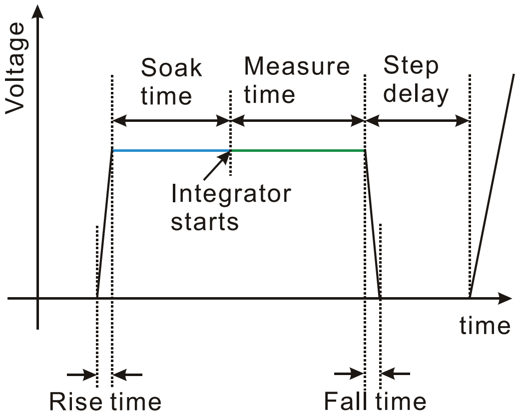

Fig 3.10 Single step in an *I*/*V* measurement profile.

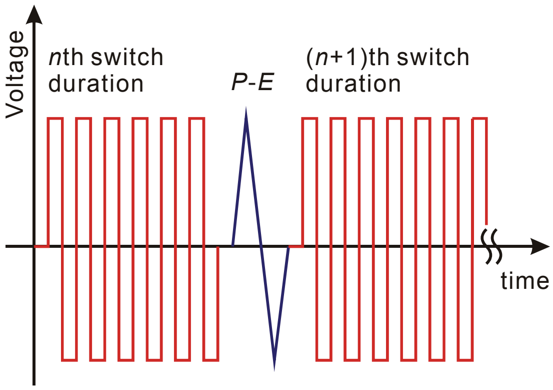

Fig 3.11 Polarization fatigue measurement profile using square fatigue stress waveform and standard bipolar triangular drive waveform for *P-E* hysteresis loop measurement.

3.3.2.3 Polarization Fatigue Measurement

Polarization fatigue is referred to as the decrease of the remanent polarization with cyclic polarization reversals. For a polarization fatigue measurement, a measurement is performed to give the initial values of $\pm P_r$, $\pm E_c$, and P_{max}. Then a drive voltage waveform (such as square, pulse, or bipolar triangular waveforms) is stressed on the sample, in which $2P_r$, $2E_c$, and P_{max} is measured at increasing intervals (Fig 3.11). The results of polarization fatigue measurements are typically represented by plotting $\pm P_r$, $\pm E_c$, and P_{max} vs. the logarithm scale of the number of switching cycles.

3.4 Synthesis Details

3.4.1 Chemicals

Chemical Name	Formula	Purity	Supplier
Barium acetate	$Ba(OAc)_2$	99 %	Riedel
Barium Nitrate	$Ba(NO_3)_2$	99 %	Fluka
Bismuth (III) citrate	$BiO_7C_6H_5$	99.99 %	Aldrich
Bismuth (III) nitrate pentahydrate	$Bi(NO_3)_3 \cdot 5H_2O$	98 %	Aldrich
Lanthanum (III) acetate hydrate	$La(OAc)_3 \cdot 1.5H_2O$	99.9 %	Alfa Aesar
Praseodymium (III) acetate hydrate	$Pr(OAc)_3 \cdot xH_2O$	99.9 %	Aldrich
Titanium(IV) *n*-butoxide	$Ti(O\text{-}n\text{-}Bu)_4$	99 %	Acros
Titanium tetraethoxide	$Ti(OEt)_4$	85 %	Aldrich
Magnesium nitrate hexahydrate	$Mg(NO_3)_2 \cdot 6H_2O$	98 %	Aldrich
Ammonium niobium (V) oxalate	$C_4H_4NNbO_9$	99.99 %	Aldrich
Vanadium (V) pentaoxide	V_2O_5	99.99 %	Alfa Aesar
Molybdenum (VI) oxide	MoO_3	99.998 %	ABCR
Tungsten (VI) oxide	WO_3	99.99 %	ABCR
Ammonium fluoride	NH_4F	98 %	Merck
Hydrogen peroxide	H_2O_2	30 %	Baker
Sodium hydroxide	NaOH	99 %	Merck
Ammonia water	$NH_3 \cdot H_2O$	25 %, p.a.	VWR
Acetylacetone	Hacac	99 %	Acros
Citric acid	$C_6H_8O_7$	99.5 %	Grüssing
Glacial acetic acid	CH_3CO_2H, HOAc	99.8 %	Acros
Diethylene glycol (DEG)	$C_4H_{10}O_3$	99 %	Aldrich
Dimethyl sulfoxide (DMSO)	C_2H_6OS	99.7 %	Acros
Diphenyl ether	$C_{12}H_{10}O$	99 %	Acros
Oleic acid	$C_{17}H_{33}COOH$	90 %	Alfa Aesar
1-hexadecene	$C_{16}H_{32}$	92 %	Acros
n-heptane	C_7H_{16}	99 %	VWR
Toluene	$CH_3C_6H_5$	99.5 %	Acros
Cetyltrimethylammonium bromide (CTAB)		99 %	Acros
Butandiolmonoacrylate (BDMA)	$C_7O_3H_{12}$	94 %	BASF
Trimethylolpropane triacrylate (TMPTA)		95 %	BASF
2,4,6-Trimethylbenzoyldiphenylphosphine oxide (TPO)		95 %	BASF
Lauryl acrylate (Laromer® LA)	$C_{15}O_2H_{28}$	95 %	BASF
Polyvinylpyrrolidone K 30	M_r 40000		Fluka

3.4.2 $BaTiO_3$ Nanocrystals

For a typical synthesis, 1.0 mmol of barium acetate (or barium hydroxide) was dissolved in 6 mmol oleic acid by gradually heating up to reflux with magnetic agitation in argon atmosphere. After cooling down in argon flow, 1 mmol of titanium (IV) butoxide and 15 mL hexadecene (or toluene and heptane) were added to obtain the oil phase. The aqueous phase was NaOH aqueous solution prepared by dissolving an appropriate amount of NaOH in freshly refluxed deionized water. The NaOH solution in a mixture of water and ethanol was prepared by adding appropriate amounts of ethanol into the NaOH aqueous solution and stirring for 5 minutes in a closed vial. The NaOH solution and the oil phase were placed into a 50 mL Teflon cup subsequently. Thereafter, the Teflon cup was sealed tightly into a stainless steel autoclave, and placed into a preheated furnace at 180 °C for 12 h.

3.4.2.1 Separation and Dispersion

Synthesis using hexadecene and NaOH aqueous solution

The crude solution was transferred into a glass bottle when the reaction was finished. a) The crude solution in the glass bottle was sealed and aged overnight for settling of the by-products. The by-products of sodium oleate in the upper oil phase were collected by centrifugation. Then, the $BaTiO_3$ nanocrystals in the supernatant were precipitated using the fivefold amount of ethanol and collected by centrifugation; b) 10 mL of ethanol were added to the crude solution in the bottle and kept under sealed conditions to achieve phase separation. After 1–2 days, two clear phases were obtained. The $BaTiO_3$ nanocrystals were obtained from the upper transparent phase, and precipitated using the fivefold amount of ethanol and collected by centrifugation. The precipitated $BaTiO_3$ nanocrystals from both routes of a) and b) can be dispersed into about 5–10 mL of dichloromethane, and reprecipitated with 20–30 mL amount of ethanol. After collection by centrifugation, the $BaTiO_3$ nanocrystals can be dispersed in organic solvents, such as chloromethane, dichloromethane, hexane, toluene etc. to form transparent dispersions.

Synthesis using hexadecene and NaOH water and ethanol solution

The by-product of sodium oleate was in the lower water/ethanol phase, and the $BaTiO_3$ nanocrystals in the upper milk-like phase were precipitated using the fivefold amount of ethanol and collected by centrifugation. The synthesized $BaTiO_3$ nanocrystals can be dispersed in the organic solvents mentioned above to form opalescent dispersions.

Synthesis using toluene and heptane

The crude solution was transferred into a glass bottle and kept overnight under sealed conditions. The by-products of sodium oleate in the upper oil phase were collected by centrifugation. Then, the $BaTiO_3$ nanocrystals in the upper supernatant were collected by rotary vacuum evaporation, or by precipitation using ethanol and collected by centrifugation. The $BaTiO_3$ nanocrystals were dispersed in 5–10 mL of dichloromethane, and reprecipitated with 20–30 mL of ethanol. The $BaTiO_3$ nanocrystals can also be dispersed in organic solvents as mentioned above.

3.4.2.1 Polymer Nanocomposites

0.1 g of fresh precipitated $BaTiO_3$ nanocrystals were mixed with 4.8 g of lauryl acrylate under ultrasonic agitation for 5 min, and 50 mg of TPO was added and dissolved by agitation. The resulting mixture was injected between two pieces of glass sandwiched with a 2.1 mm thick spacer. After photo-polymerization in a UV box (UVA Cube, Hoenle) for ten minutes, the $BaTiO_3$/poly (lauryl acrylate) composite was obtained.

3.4.3 $Bi_4Ti_3O_{12}$ Nanostructured Microspheres

The synthesis procedure includes two steps: a) DEG-mediated coprecipitation of the amorphous precursor powder, and b) hydrothermal treatment of the precursor powder producing crystalline $Bi_4Ti_3O_{12}$ particles.

3.4.3.1 Coprecipitation in DEG

2 mmol titanium tetraethoxide ($Ti(OC_2H_5)_4$) and 2 mmol acetylacetone were dissolved in 50 ml DEG under magnetic stirring at room temperature, yielding a transparent yellow solution. Subsequently, 2.667 mmol $Bi(NO_3)_3 \cdot 5H_2O$ were added (Bi^{3+}:Ti^{4+} ratio = 4:3). A clear reddish solution was formed when the solution was heated up to 70 °C for 30 minutes under magnetic stirring. 5 ml aqueous ammonia solution (25 wt. %) were injected drop by drop. The solution was heated up to 100 °C and maintained for 30 min for precipitation. The yellowish dispersion was destabilized using acetone and the particles were isolated by centrifugation. After thorough washing with acetone and water, the product was dried at 80 °C for 24 h resulting in a brownish gel-like substance. The gel-like substance was ground in an agate mortar with a pestle and collected as precursor powder for further hydrothermal treatment.

3.4.3.2 Coprecipitation in Ethanol

For comparison, an ethanol-mediated coprecipitation was carried out as follows: 2.667 mmol $Bi(NO_3)_3 \cdot 5H_2O$ were dissolved in 5 ml glacial acetic acid under magnetic stirring at 50 °C, then 2 mmol titanium tetraethoxide ($Ti(OC_2H_5)_4$) were added. Subsequently, the solution was mixed with 50 ml ethanol and heated up to 70 °C. 10 ml aqueous ammonia (25 wt%) were injected into the solution drop by drop. The solution was kept at 70 °C for 30 min for precipitation. The white precipitates were collected by centrifugation and thoroughly washed with acetone and deionized water, the precipitate was dried at 80 °C for 24 h resulting in a white precursor powder.

3.4.3.3 Hydrothermal Treatment

The hydrothermal treatment was carried out in a stainless steel autoclave with a 50 ml Teflon liner. The precursor (0.1–0.4 g) was mixed with 25 ml of 0.8–1.0 mol/L aqueous NaOH solution, placed in the Teflon liner, and sealed tightly in the stainless steel autoclave. Subsequently the autoclave was placed in an oven and heated to 180 °C for 3–24 h. The autoclave was then cooled down to room temperature. The product was collected by centrifugation and thoroughly washed with deionized water. After drying at 80 °C overnight crystalline $Bi_4Ti_3O_{12}$ products were obtained.

3.4.4 $Bi_{3.25}Pr_{0.75}Ti_{2.97}V_{0.03}O_{12}$ Nanoparticles and Ceramics

3.4.4.1 Synthesis of Gels

3.41 mmol of bismuth citrate (5 % excess), 0.75 mmol of praseodymium acetate hydrate and 5.3 g of citric acid hydrate were dissolved in a solution of 15 mL aqueous ammonium hydroxide (25 %) and 15 mL deionized water at room temperature with magnetic stirring, giving a clear solution (solution 1#). Vanadium citrate aqueous solution was prepared by dissolving 0.015 mmol of V_2O_5 and 2 g citric acid hydrate in 5 mL of deionized water above 90 °C (solution 2#). 2.97 mmol of $Ti(O\text{-}n\text{-}Bu)_4$ was mixed with 0.5 mL of Hacac, then 5 mL of ethanol were added to yield a yellowish transparent solution (solution #3). The solution 2# and 3# were subsequently added to the solution 1# at room temperature with magnetic stirring and rinsing with 5 mL of deionized water and ethanol respectively. A light yellowish transparent precursor solution was obtained. The precursor solution was gradually heated up to 70 °C and maintained over night with mild magnetic agitation for gelation.

3.4.4.2 Synthesis of BPTV Nanoparticles and Ceramics

The gels obtained were further dehydrated at 105 °C for 24 h, and heated up to 320 °C (2 h, 1 °C/min) in air for carbonization. The carbonized precursor was calcined at 450–700 °C (5 °C/min) for 1 h to get porous powders. The powders were then ground with ethanol for 30 min using an agate pestle and mortar, and dried at 90 °C over night. For the preparation of ceramics, the powders obtained at 550 °C for 1 h were uniaxially pressed into pellets of 8.0 mm in diameter and about 1.0 mm in thickness under a pressure of 800 MPa. Thereafter, the green pellets were sintered in air at 900 °C (5 °C/min) for 4 h, and cooled down.

3.4.5 $Bi_{3.25}La_{0.75}Ti_{3-x}M_xO_{12}$ (M = Mo, W, Nb, V) Nanoparticles and Ceramics

3.4.5.1 Synthesis of the $BLTM_x$ Gels

6.825 mmol of bismuth citrate (5 % excess), 1.50 mmol of lanthanum acetate and 12 g of citric acid hydrate were dissolved in a solution of 30 mL aqueous ammonium hydroxide (25 %) and 30 mL deionized water at room temperature with magnetic stirring, giving a clear solution (solution 1#). Peroxy niobium citrate aqueous solution was prepared according to Narendar and Messing's report.[150] Ammonium metal (V, Mo, and W) citrate aqueous solution was prepared by dissolving the corresponding metal oxide and 2 g citric acid hydrate in 4 mL of aqueous ammonium hydroxide at 70 °C and maintained with magnetic agitation for 2–12 h (solution 2#). A stoichiometric amount of $Ti(O\text{-}n\text{-}Bu)_4$ was mixed with 1.0 mL of Hacac and 5 mL of ethanol to yield a yellowish transparent solution (solution #3). The solution 2# and 3# were subsequently added to the solution 1# at room temperature with magnetic stirring and rinsing with 5 mL of deionized water and 15 mL of ethanol respectively, which yielded a red ($BLTNb_x$) or yellowish (the other $BLTM_x$) transparent precursor solution. The precursor solution was gradually heated up to 70 °C and agitated for 2–3 h, and maintained at 70 °C over night for gelation without agitation.

3.4.5.2 Synthesis of the $BLTM_x$ Nanoparticles and Ceramics

The gel obtained was further dehydrated at 105 °C for 24 h, and heated up to 320 °C (2 h, 1 °C/min) in air for carbonization. The carbonized precursor was calcined at 450–700 °C (5 °C/min) for 1 h to get porous powder products. The powders were then ground with ethanol for 30 min using an agate pestle and mortar, and dried at 90 °C over night. For preparation of ceramics, the powders obtained at 550 °C for 1 h were mixed with 2.0 wt% of PVP and uniaxially pressed into pellets of 8.0 mm in diameter and about 1.0 mm in thickness under a pressure of 800 MPa. Thereafter, the pellets were sintered in air at 900 °C (5 °C/min) for 4 h, and naturally cooled down.

3.4.6 $BaMgF_4$ Nanoparticles

3.4.6.1 Hydrothermal Synthesis

1.0 mmol of $Ba(NO_3)_2$ and 1.0 mmol of $Mg(NO_3)_2$ were dissolved in 20 mL of diethylene glycol (DEG) or water (solution *a*). 4.0 mmol of NaF were dissolved in 2.0 mL water (solution *b*). Solution *b* was added into solution *a* and then transferred into an autoclave with a 25 mL Teflon cup, heated at 130 °C for 17 h. The nanoparticles were collected by centrifugation and thoroughly washed with deionized water, and dried at 80 °C over night.

3.4.6.2 High Temperature Surfactant Method

A stock water solution containing 0.25 M of $Ba(NO_3)_2$ and 0.25 M of $Mg(NO_3)_2 \cdot 6H_2O$ was prepared. 4.0 mL of stock solution was mixed with 14.0 g of diphenyl ether, 6.0 g of CTAB, 4.0 g of n-butanol, and heated up to 80–150 °C (*a*), the stock solution was replaced with 4.0 mL of 1.0 M NH_4F aqueous solution for another precursor *b*. *b* was added into *a* with intense magnetic stirring and the mixture was heated at 150 °C for 24 h. After the reaction was finished, about 100 mL acetone was added. The product was collected by centrifugation and washed with acetone and ethanol, then dried at 80 °C over night.

3.4.6.3 DMSO Mediated Coprecipitation Method

1.0 mmol of $Ba(NO_3)_2$ and 1.0 mmol of $Mg(NO_3)_2 \cdot 6H_2O$ were dissolved in 40–50 mL DMSO by heating up to 120–160 °C under magnetic agitation (solution *a*). 4.0 mmol NH_4F was dissolved in mixture of 5–30 mL H_2O and 0–20 mL acetic acid (solution *b*). Precipitation was produced by pouring solution *b* into solution *a*, and the reaction was maintained at 120–160 °C for 1–30 min. The product was collected by centrifugation and thoroughly washed with deionized water, and dried at 80 °C over night.

3.4.6.4 Preparation of $BaMgF_4$/Polymer Composites

$BaMgF_4$/TMPTA composite

50–80 mg of as-synthesized $BaMgF_4$ was mixed with 4.0 g of TMPTA, and 4.0 mg of TPO. The mixture was injected between tow glass slides with a spacer of 1.5 mm in thickness. After polymerized in a UV box (UVA Cube, Hoenle) for 10 min, the $BaMgF_4$/TMPTA composites were obtained.

$BaMgF_4$/BDMA composite

0.2 g of the synthesized $BaMgF_4$ particles were mixed with 2.0 mL oleic acid, and refluxed for 10 min with magnetic stirring. The particles in the supernatant liquid from centrifugation was precipitated by adding acetone and collected by further centrifugation, then, mixed with 3.0 g of BDMA and 1.0 g of TMPTA, with 4.0 mg TPO. The mixture was injected between two glass slides with a spacer of 1.5 mm in thickness, and polymerized in a UV box (UVA Cube, Hoenle) for 10 min.

3.5 Characterization Details

3.5.1 X-ray Diffraction (XRD)

Powder XRD patterns were recorded on a Stoe Stadi P powder diffractometer equipped with a curved germanium (111) monochromator using Cu $K_{\alpha 1}$ radiation. For calculations using the Scherrer equation, the diffraction peaks were fitted using WinXPOW Fit 2.06, and the volume-average particle size, D_v, was calculated using WinXPOW Size/Strain 2.02 (STOE&Cie, GmbH). The nanocrystal size is defined as the diameter assuming the nanocrystals are spherical in shape ($d = 4/3D_v$).[151]

The XRD patterns of $BLTM_x$ nanoparticles and ceramics were recorded using Cu K_α radiation in Bragg-Brentano geometry on a Siemens D5000 X-ray powder diffractometer.

3.5.2 Thermogravimetry and Differential Scanning Calorimetry (TG-DSC)

TG-DSC data were reordered using a Netzsch STA 409 system in air atmosphere with a heating rate of 5 °C/min.

3.5.3 FT-IR and UV/Vis Spectroscopy

The Fourier transform infrared (FT-IR) spectrum was record on a Bio-Rad Excalibur FTS 3000 spectrometer. UV/Vis spectra were recorded using a Shimadzu UV-1650PC spectrophotometer.

3.5.4 SEM and EDS

The SEM images and EDS were recorded using a Zeiss DMS 982 Gemini field emission scanning electron microscope equipped with a Noran Voyager energy-dispersive spectroscopy system.

3.5.5 TEM

TEM images and SAED patterns were obtained using a Philips CM200FEG ST/Lorentz transmission electron microscope (acceleration voltage: 200kV) equipped with 1 k Slow-Scan CCD-Camera (Gatan).

3.5.6 Ferroelectric Properties

For ferroelectric characterization, the sintered pellets were polished with abrasive paper to a thickness of about 0.10 mm. Electrodes were prepared on both sides of a polished pellet, using silver paste (AG-500, Conductive Compounds, Inc.) and annealing at 720 °C for 10 min. The diameter of the electrodes was above 1.50 mm. The thickness and the electrode area of the samples were measured using a digital vernier caliper.

The ferroelectric properties were measured on a Radiant Precision LC Tester equipped with a Radiant Precision High Voltage Interface and a Trek 610E high voltage amplifier. P-E hysteresis loops were measured using a standard bipolar triangular drive waveform. The switching current density was obtained as the first derivative of the polarization vs. time. The leakage current densities were measured in an unswitched linear type. For BPTV ceramic, the fatigue properties were measured using a 1 kHz square waveform with switching electric field of 100 kV/cm. P-E hysteresis loops with $E_{\max}$ of 200 kV/cm were performed after several switching cycles as indicated in the section. For $\mathrm{BLTW}_{0.025}$ ceramic, the fatigue properties were measured at 1.6 kHz with electric field of 125 kV/cm, and P–E hysteresis loops with $E_{\max}$ of 125 kV/cm were performed after several switching cycles.

3.5.7 Rietveld Refinement

For the Rietveld refinement, the ceramic was moderately ground. XRD powder pattern from the as-ground powder was measured with a 2-theta step size of 0.01° and a scan speed of 60 seconds per step. The XRD Rietveld refinement was carried out using the GSAS-EXPGUI program.[152, 153] LaB_6 was used as a standard to determine the shift of the zero point.

4. Results and Discussion

4.1 Synthesis of $BaTiO_3$ Nanocrystals

This section presents a two-phase solvothermal synthesis approach for the preparation of hydrophobic $BaTiO_3$ nanocrystals. The two-phase method is based on the growth of nanocrystals at the oil/water interface by the reaction between metal surfactant complexes in the oil phase and a mineralizer in the water phase. Three kind of organic solvents, hexadecene, toluene, and heptane were used as the oil phase and compared to each other with respect to the product quality. The $BaTiO_3$ particles are crystalline with a mean size of 3.7 nm and can be dispersed in a variety of organic solvents forming highly transparent dispersions.

4.1.1 Synthesis Strategy

Brust et al.[154] reported the synthesis of thiol-coated gold nanoparticles with size of 1–3 nm by reduction of an Au source in toluene (oil phase) with an aqueous solution of sodium borohydride (water phase) in the presence of dodecanethiol, which might be the first report on the oil/water two-phase synthesis method. Recently, Pan et al. successfully synthesized anatase type TiO_2 nanocrystals via reaction between a toluene solution of titanium (IV) *n*-propoxide and oleic acid (or stearic acid), and an aqueous solution of tert-butylamine at 180 °C.[155] In this work, a two-phase solvothermal synthesis approach was used for the preparation of hydrophobic $BaTiO_3$ nanocrystals.

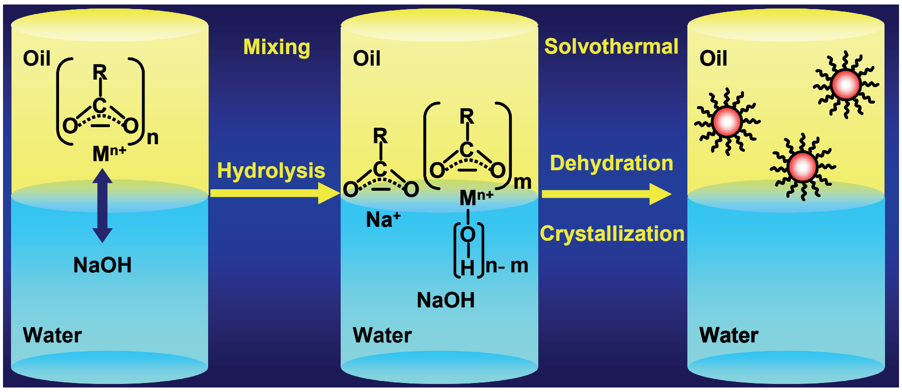

Fig 4.1 Schematic diagram of the oil/water two-phase solvothermal method.

Fig 4.1 shows a schematic synthesis diagram of the oil/water solvothermal method, which is based on the growth of nanocrystals at the oil/water interface via the reaction between metal surfactant molecules (in the oil phase) and a mineralizer (in the water phase).

1. The metal surfactant salts are used in dual function acting as a metal source and a surfactant.

2. The metal surfactant salts are expected to be partially hydrolyzed to form metal surfactant hydroxides in the mixing stage.

3. Nucleation and crystallization are accompanied by dehydration and further hydrolysis of the metal surfactant hydroxides in the solvothermal stage.

4. The as-grown nanocrystals are capped by the surfactants and then extracted from the oil/water interface into the oil phase driving the crystallization forward.

5. The crystal growth in the oil phase is suppressed by the surfactant cap and the lack of mineralizers in the hydrophobic phase.

4.1.2 Precursors and Reactions

Barium oleate was formed by the reaction of barium acetate or barium hydroxide and oleic acid under inert atmosphere reflux conditions (Eq 4.1).

$$\mathrm{Ba(OAc)_2 + 2RCOOH \rightarrow Ba(O_2CR)_2 + 2AcOH} \qquad \textbf{Eq 4.1}$$

To avoid the formation of barium carbonate impurities, the use of barium acetate is beneficial due to the lower sensitivity towards CO_2 as compared to barium hydroxide. The released by-product, acetic acid or water, was removed by the carrier gas. Titanium butoxide oleate ($Ti(OR)_{4-x}(RCOO)_x$) was formed by the reaction of titanium butoxide and oleic acid to yield a yellowish solution, a process comparable to the formation of metal alkoxide acetate complexes (Eq 4.2).[156, 157]

$$\mathrm{Ti(O\text{-}n\text{-}Bu)_4} + x\mathrm{RCOOH} \rightarrow \mathrm{Ti(O_2CR)}_x\mathrm{(O\text{-}n\text{-}Bu)}_{4-x} + x\mathrm{n\text{-}Bu\text{-}OH} \qquad \textbf{Eq 4.2}$$

The water phase used was NaOH aqueous solution. The complete reaction in the synthesis can be expressed as:

$$\begin{aligned}&\mathrm{Ba(O_2CR)_2 + Ti(O\text{-}n\text{-}Bu)_4 + 2\,NaOH + H_2O \rightarrow}\\&\mathrm{BaTiO_3 + 2NaO_2CR + 4n\text{-}Bu\text{-}OH}\end{aligned} \qquad \textbf{Eq 4.3}$$

4.1.3 Variation of Synthesis Conditions and Product Analysis

Three kind of organic solvents, hexadecene, toluene, and heptane were used and compared to each other with respect to the product quality. After the reaction, white solids were found in the oil phase for all the three solvents. The white solids are by-products as identified by XRD measurements (Fig 4.2). The synthesized $BaTiO_3$ nanocrystals were only found in the supernatant clear solution. The $BaTiO_3$ nanocrystals in the supernatant oil phase can be precipitated using ethanol or isolated by vacuum evaporation of the organic solvent. The isolated $BaTiO_3$ nanocrystals can be redispersed in various organic solvents, such as chloromethane, dichloromethane, hexane, toluene etc. to form transparent dispersions. The synthesis conditions are summarized in Table 4.1.

Table 4.1 Conditions for the two-phase synthesis of $BaTiO_3$ nanocrystals.[a]

No.	Solvent (mL)	NaOH (aq) (M, mL)	Size[b] (nm)
BTO-1	hexadecene: 15	4, 5	3.7
BTO-2	hexadecene: 10	4, 10	5.9
BTO-3	hexadecene: 10	2, 10[c]	8.1
BTO-4	hexadecene: 10	2, 10	amorphous
BTO-5	toluene: 15	4, 5	4.1
BTO-6	heptane: 15	4, 5	6.7

a all the syntheses were performed at 180 °C for 12 h; *b* diameter assuming the nanocrystals are spherical in shape: $d = (4/3)L_{\mathrm{vol}}$,[151] where L_{vol} is the volume-average particle size calculated by Scherrer equation, *c* in water and ethanol (1 : 1 in volume).

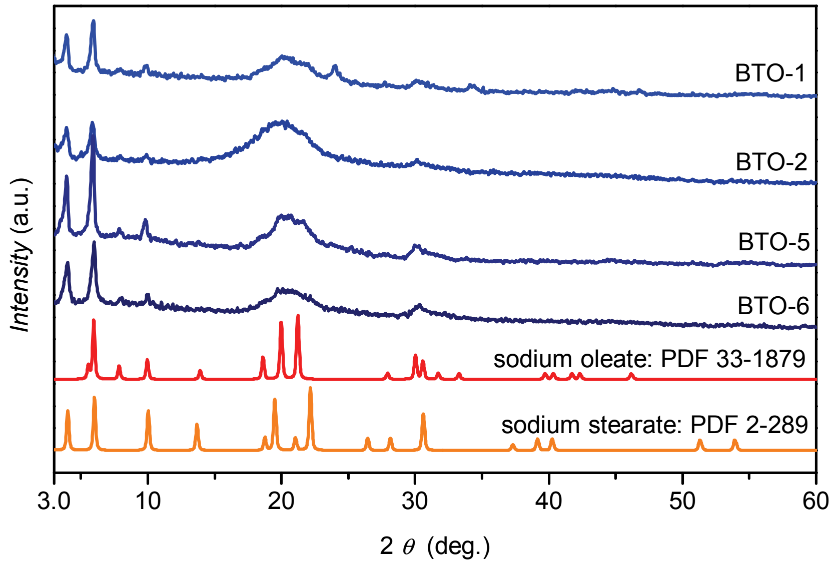

Fig 4.2 XRD patterns of by-products collected from the upper crude oil phases.

4.1.4 Interaction between the $BaTiO_3$ Nanocrystals and the Surfactants

The interaction between the $BaTiO_3$ nanocrystals and the surfactants was studied by FTIR spectroscopy. As seen in Fig 4.3, the strong absorbance at 1408 and 1553 cm^{-1} are attributed to the CO symmetric and asymmetric stretching vibrations of the deprotonated carboxyl group, respectively.[158, 159] The strongest peaks at 2853 and 2924 cm^{-1} are from the C-H symmetric and asymmetric stretching vibrations of the $-CH_2-$ and $-CH_3$ groups in the hydrophobic chains of the oleic acid molecules.[158, 159] These evidences support the assumption that the carboxyl groups of the oleic acid molecules were chemically bound to the surface of the $BaTiO_3$ nanocrystals, directing the hydrophobic tails of the surfactants outward, thereby causing the hydrophobicity of the formed $BaTiO_3$ nanocrystals. The hydrophobicity provided by the surfactant molecules is expected to play a crucial role in the stabilization of the $BaTiO_3$ nanocrystals in different organic solvents, as well as in the modulation of the crystallization and the crystal growth to yield small nanocrystals.

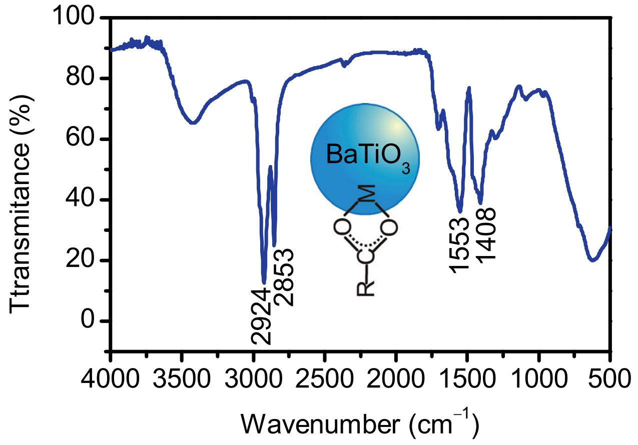

Fig 4.3 The FTIR spectrum of the $BaTiO_3$ nanocrystals synthesized from the oil/water solvothermal method.

4.1.5 Morphology of the $BaTiO_3$ Nanocrystals

The morphology of the $BaTiO_3$ nanocrystals was characterized by TEM including HRTEM. Fig 4.4a gives the typical transmission electron microscopy (TEM) image of $BaTiO_3$ nanocrystals prepared from the two-phase solvothermal synthesis at 180 °C for 12 h using 15 ml hexadecene, and 5 mL of 4 mol/L NaOH aqueous solution (BTO-1). The sample for TEM observation was directly prepared from the crude oil phase containing $BaTiO_3$ nanocrystals without size selection. The rather low contrast in the bright-field TEM image is due to the presence of a surfactant layer around the particle surface.[160]

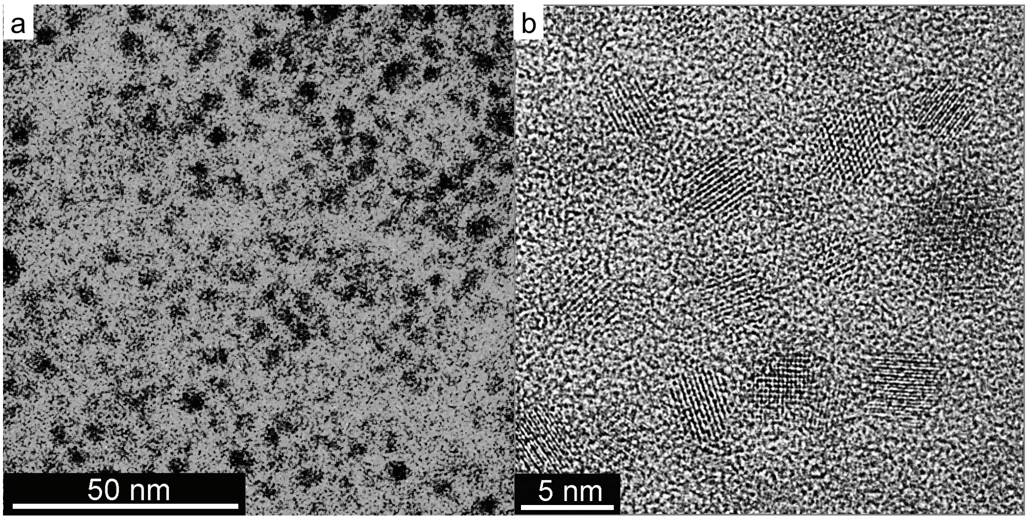

Fig 4.4 (a) Typical TEM overview of $BaTiO_3$ nanocrystals, (b) HRTEM image of $BaTiO_3$ nanocrystals.

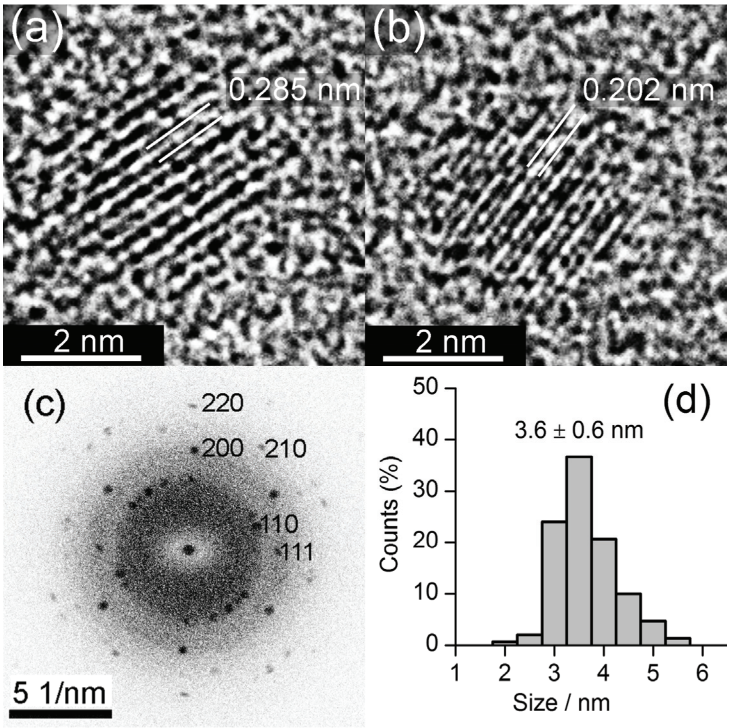

Fig 4.5 (a) and (b) isolated $BaTiO_3$ nanocrystals, (c) SAED pattern indexed with general indices, (d) size distribution of the $BaTiO_3$ nanocrystals obtained by TEM.

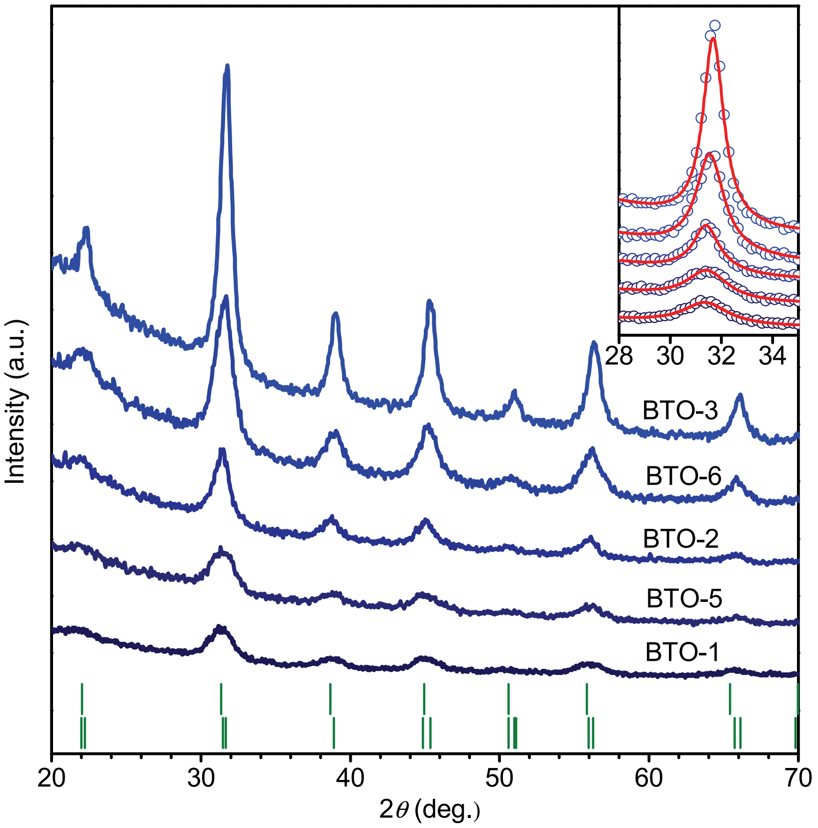

Fig 4.6 XRD patterns of $BaTiO_3$ nanocrystals; vertical bars: reflections of cubic (upper, PDF No. 31–174) and tetragonal (lower, PDF No. 5–626) $BaTiO_3$, inset: circles show the corresponding experimental (110) peaks, solid lines show the fitting.

A high resolution TEM (HRTEM) image is shown in Fig 4.4b, which presents isolated spherical nanocrystals with clear lattice fringes. Thus, the synthesized $BaTiO_3$ nanocrystals are crystalline and well dispersed. Fig 4.5a and 4.5b give the HRTEM images of two individual $BaTiO_3$ nanocrystals. Fig 4.5a shows a $BaTiO_3$ nanocrystal with size around 3.5 nm. The observed lattice spacing of 0.285 nm can be assigned to the (011) series. Fig 4.5b gives the HRTEM image of a $BaTiO_3$ nanocrystal of about 3.0 nm in diameter. A lattice spacing of 0.202 nm was observed, which could be assigned to the (002) series. Thus a unit cell with $a = 0.404$ nm can be deduced, which is in good agreement with $a = 0.4031$ nm of the cubic cell given by the PDF No. 31-174. Fig 4.5c gives a selected area electron diffraction (SAED) pattern. The SAED spot pattern can be assigned to several $BaTiO_3$ nanocrystals of different orientations, and can be well indexed to the cubic $BaTiO_3$ crystal structure. The diffraction spots are indexed according to the cubic $BaTiO_3$ crystal structure (PDF No. 31-174). The SAED pattern further indicates a high phase purity and crystallinity of as-synthesized $BaTiO_3$ nanocrystals. The statistical size distribution is shown in Fig 4.5d, which was obtained from a TEM measurement by counting over hundred of individual nanocrystals. The size of the as-synthesized $BaTiO_3$ nanocrystals covers a range from 2.0 to 6.0 nm with an average size of 3.6 ± 0.6 nm.

The X-ray diffraction (XRD) patterns of $BaTiO_3$ nanocrystals synthesized under different conditions are shown in Fig 4.6. All XRD patterns have broad diffraction peaks and can be indexed to the $BaTiO_3$ phase without any crystalline impurities such as $BaCO_3$ or TiO_2. Such broad diffraction peaks do not allow a differentiation between the cubic and tetragonal phase of $BaTiO_3$. The average crystallite sizes determined using the Scherrer equation by fitting the line broadening of the (110) XRD peaks (inset of Fig 4.6) are listed in Table 4.1.The calculated size for sample BTO-1 is 3.7 nm, which is close to the average size of 3.6 ± 0.6 nm obtained from TEM measurements. This result is in agreement with the size of single $BaTiO_3$ nanocrystals observed in the HRTEM images.

The ratio of oil to water, concentration and quantity of mineralizer, introduction of ethanol, and organic solvents were found to influence the crystallization and crystal growth in the developed method. As seen in Table 4.1, a decrease of the volume ratio of oil to water from 3 : 1 to 1 : 1, caused a slight increase of crystallite size from 3.7 nm (BTO-1) to 5.9 nm (BTO-2). Decreasing the volume ratio of the oil phase to the aqueous phase will result in an increase of the mineralizer present and metal concentrations in the oil phase, therefore the crystal growth rate may be increased. On the other hand, the concentration of NaOH in the aqueous solution was found to be very important for the crystallization. An X-ray amorphous sample (BTO-4) was obtained using 10 mL of 2 M NaOH aqueous solution, even though the amount of NaOH was the same as for BTO-1. However, introducing ethanol in the aqueous solution resulted in a substantial increase of crystallite size to 8.1 nm (BTO-4). Introduction of ethanol can extract sodium oleate molecules from the oil phase into the water/ethanol phase, which will cause a decrease of the surfactant concentration in the oil phase. As a result, crystal growth is facilitated. Another reason might be the increase of miscibility of the oil/water phases by the addition of ethanol under solvothermal conditions. Thereby, the mass transfer between the oil and water phase is improved resulting in an increase of the crystallization rate. Additionally, the increase of pressure caused by ethanol might be another reason for the increase of crystal size. The nanocrystals synthesized using toluene and heptane were 4.1 nm and 6.7 nm respectively.

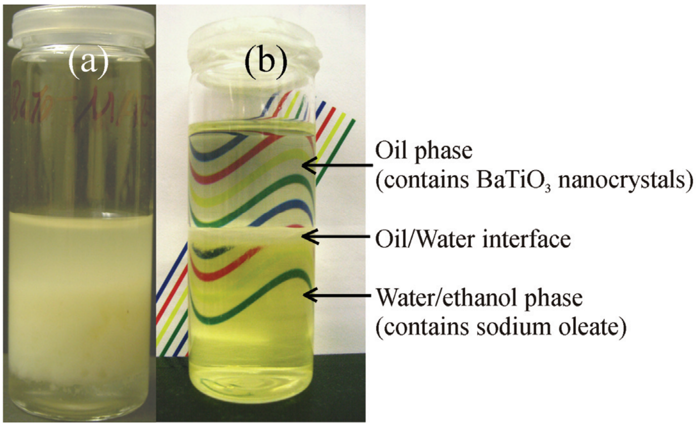

Fig 4.7 Photographs of phase separation for synthesis using hexadecene and NaOH aqueous solution: (a) Crude reaction solution before (left), (b) after using ethanol for phase separation.

A phase separation was observed after addition of ethanol into the crude product solution using hexadecene and aqueous NaOH solution. As seen in Fig 4.7, the milk-like crude reaction solution transformed into two clear phases after adding ethanol. X-ray powder diffraction confirmed the extraction of $BaTiO_3$ nanocrystals into the upper oil phase, and the by-product, sodium oleate, was extracted into the lower water/ethanol phase. The phase separation observed may be used as an alternative way for nanocrystal separation and purification.

The dispersions of $BaTiO_3$ nanocrystals in organic solvents are colorless or light yellowish in color, depending on the concentration. Careful preparation can yield transparent dispersions containing nanocrystals up to 5.0 wt%. Fig 4.8a gives the UV/Vis spectrum of 3.0 wt% dispersion of $BaTiO_3$ nanocrystals dispersed in chloromethane. The transmission of the dispersion is above 80 % within the range of wavelength from 400–700 nm. The UV/Vis spectrum of $BaTiO_3$/poly(lauryl acrylate) nanocomposite containing 1.0 wt% $BaTiO_3$ nanocrystals is given in the Fig 4.8b. The transmission of the $BaTiO_3$/poly(lauryl acrylate) nanocomposite is above 70 % in the visible range.

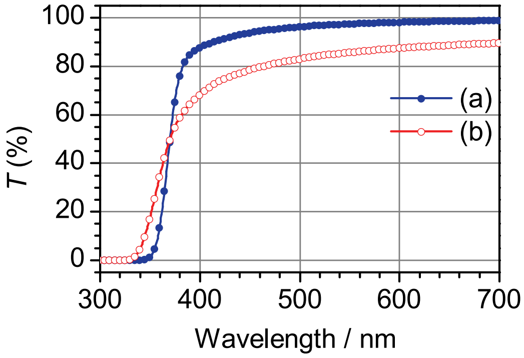

Fig 4.8 UV/Vis spectra of 3.0 wt% dispersion of $BaTiO_3$ nanocrystals in dichloromethane, and (b) $BaTiO_3$/poly (lauryl acrylate) nanocomposite with a thickness of 2.0 mm, containing 1.0 wt% $BaTiO_3$ nanocrystals.

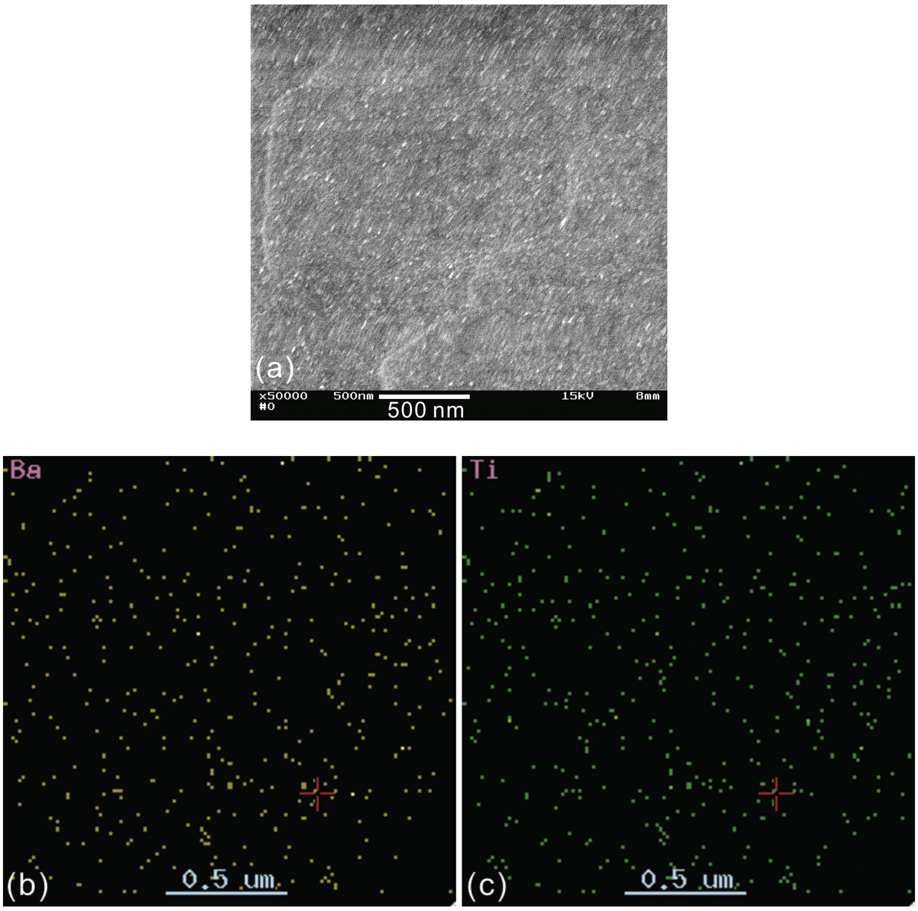

Fig 4.9 SEM image (a) and (b) Ba, and (c) Ti element maps of the $BaTiO_3$/poly (lauryl acrylate) nanocomposite (1.0 wt%).

Lauryl acrylate was used as the monomer because hydrophobic backbone makes it compatible with the hydrophobic $BaTiO_3$ nanocrystals, thereby avoiding the agglomeration of the nanocrystals. The SEM image of the polymer nanocomposite shows a uniform morphology (Fig 4.9a). However, it is not possible to determine the particle size distribution of the $BaTiO_3$ nanocrystals because of the low resolution. The EDS technique provides an alternative way to obtain the distribution of the nanocrystals in the nanocomposite, which allows for mapping the element distribution. As seen in Fig 4.9b and 4.9c, the Ba- and Ti-maps show homogeneous and almost identical element distribution. The maps indicate a low degree of agglomeration of the $BaTiO_3$ nanocrystals in the polymer matrix. The homogeneous distribution of the nanocrystals in the polymer matrix is apparently important for the high transparency of the final nanocomposites. These transparent dispersions and nanocomposites are of interest for transparent dielectric and optical applications.

The broad diffraction peaks observed from the synthesized $BaTiO_3$ nanocrystals make it difficult to distinguish the tetragonal $BaTiO_3$ phase from the cubic one. The as-synthesized $BaTiO_3$ nanocrystals were calcined at 800 °C for 3 h and characterized by XRD. No splitting was found for the (002) diffraction peak centered around 45° (Fig 4.10, inset), thus the calcined material has the cubic structure.

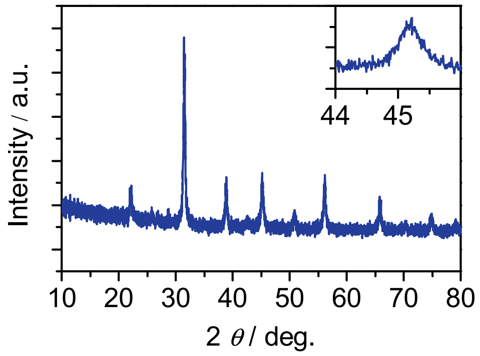

Fig 4.10 XRD Pattern from $BaTiO_3$ nanocrystals calcined at 800 °C for 3 h, inset: detail of (002) diffraction peak centered around $2\theta = 45.0°$.

4.1.6 Summary

This section provides a new approach for the preparation of oil soluble $BaTiO_3$ nanocrystals with a mean size of 3.7 nm. They are among the smallest isolated $BaTiO_3$ nanocrystals reported so far. The $BaTiO_3$ nanocrystals were synthesized using a mild oil/water two-phase solvothermal method. The influence of solvents and concentration of NaOH on the crystallization and size of nanocrystals were discussed. According to XRD and TEM studies, the materials have a high phase purity, crystallinity, and uniform crystallite size below 5 nm. More important, $BaTiO_3$ nanocrystals synthesized by the two-phase approach can be dispersed in conventional organic solvents, such as chloromethane, dichloromethane, hexane, toluene etc. to form highly transparent dispersions. The high hydrophobicity and dispersibility resulted from the grafted surfactant molecules on the surface of the $BaTiO_3$ nanocrystals. The latter is crucial for the formation of the uniform nanocrystals with small size, the highly transparent dispersions, and the homogeneous transparent nanocomposites. Even though cubic $BaTiO_3$ is not ferroelectric, the synthesized $BaTiO_3$ nanocrystals are interesting candidates for the investigation of size effects in nanoscale dielectrics, and in the fabrication of novel nanostructures using spin-coating methods for integrated electrooptic and high dielectric applications.

4.2 Synthesis of $Bi_4Ti_3O_{12}$ Nanostructured Microspheres

In this section, a hydrothermal method was developed for the synthesis of $Bi_4Ti_3O_{12}$ nanostructured microspheres consisting of granular nanoparticles in the core and nano-platelets on the shell. The precursor powder was prepared using a diethylene glycol mediated coprecipitation method. Tailoring of the morphology was achieved by changing the precursor quantity, sodium hydroxide concentration, and reaction time. The formation mechanism of the nanostructured microspheres probably involves aggregation, followed by dissolution and recrystallization.

4.2.1 Synthesis and Phase Characterization

The DEG-mediated coprecipitation has been used by Siemons et al.[108] to prepare precursors for various perovskite oxides, including $BaTiO_3$, $CaTiO_3$, $SrTiO_3$, and $PbTiO_3$. Titanium (IV) isopropoxide was used as titanium source. Since titanium (IV) alkoxides are moisture sensitive, protective atmosphere is required to avoid the hydrolysis of titanium (IV) alkoxides during the precursor preparation. Acetylacetone was used to stabilize titanium (IV) alkoxide. Thus, a precursor solution stable against moisture is obtained and the precipitation can be carried out without the need of a vacuum line and dry nitrogen. Chelating ligands such as acetic acid, and acetylacetone have been widely used to experimentally control the rate and extent of hydrolysis of highly aqueous reactive titanium (IV) alkoxides.[161, 162]

Table 4.2 Summarized synthesis conditions.

No.	Precursor^a (g)	NaOH(aq, mol/l)	Time (h)^b
HT1	0.4	0.8	3
HT2	0.4	0.8	24
HT3	0.1	0.8	16
HT4	0.1	1	16
HT5	0.1	1	24

a precursor powder prepared by DEG-mediated coprecipitation; *b* duration of the hydrothermal treatment at 180 °C.

The hydrothermal synthesis conditions are summarized in Table 4.2. Fig 4.11 shows the XRD patterns of the products obtained from the hydrothermal synthesis and the precursor. As shown in Fig 4.11a–e, all the XRD patterns of the products obtained from hydrothermal synthesis show broad peaks. Only one broad peak centered at about 29° (2 theta) was observed in the XRD pattern of the precursor obtained from DEG-mediated coprecipitation (Fig 4.11f), indicating the presence of an X-ray amorphous phase. The XRD powder patterns of the products obtained from hydrothermal synthesis clearly indicate the presence of crystalline $Bi_4Ti_3O_{12}$ (ICSD card No. 87808, Fig 4.11g). However, one reflection close to the (171) diffraction peak marked by an arrow (Fig 4.11) could not be indexed to any bismuth and/or titanium compounds. The latter is caused by the presence of an impurity or poorly crystallized particles and will be discussed below.

Comparing X-ray diffraction patterns of products obtained from treatment in 1 M of aqueous NaOH solution with that of 0.8 M (Fig 4.11b and 4.11c), it was found that the relative intensities of the (111), (171) and (200) peaks increase with the concentration of aqueous NaOH solution. The opposite is true for the peak marked by the arrow, between the peaks (171) and (200). The (151) and ($0\underline{10}0$) reflections are only observed in the XRD patterns of the products from 1 M of aqueous NaOH solution (Fig 4.11a and 4.11b), but not detected in the products from 0.8M of aqueous NaOH solution (Fig 4.11c–e). These results indicate that the NaOH accelerates the crystallization.

The amount of the precursor powder for the hydrothermal synthesis also plays a role for the crystallization of the products. The (111) and (200) reflections are discerned in the XRD pattern of the product synthesized from 0.1 g precursor powder after the hydrothermal treatment with 25 ml of 0.8 M NaOH at 180 °C for 16 h (Fig 4.11c). However, these peaks are not observed in the XRD patterns of the products synthesized from 0.4 g precursor, in spite of a longer reaction time (Fig 4.11d). The lower precursor concentration causes a lower supersaturation favoring the formation of larger crystals, and vice versa. On the other hand, the lower concentration of the precursor powder also causes a higher relative amount of NaOH, favoring crystallization as discussed above due to a higher mineralizer concentration. Another factor clearly affecting the crystallinity of the product is the duration of the hydrothermal treatment. An increase of crystallinity is observed with the duration of the hydrothermal treatment. Comparing Fig 4.11a with 4.11b, and 4.11d with 4.11e, the relative intensity of the (171) reflection increases with the reaction time.

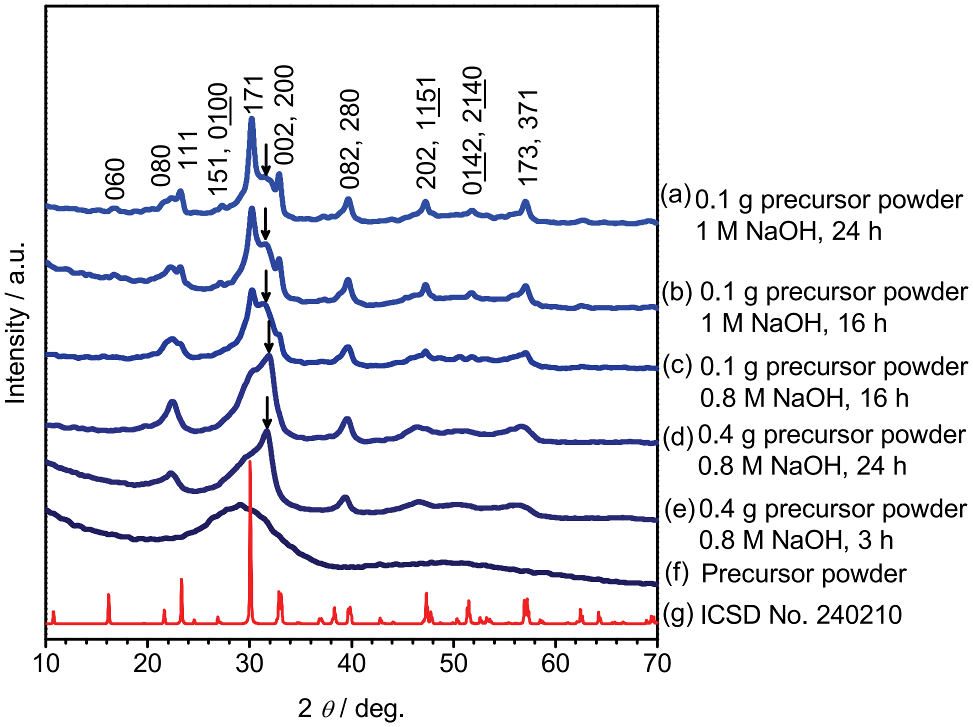

Fig 4.11 XRD patterns of products prepared using precursor powder from DEG-mediated coprecipitation by hydrothermal synthesis at 180 °C, Miller indices were assigned using the standard setting of S.G. No.41 (*Aea2*, former *Aba2*).

4.2.2 Morphology Evolution of the Nanostructured Microspheres

The SEM images show the morphologies and structures of the $Bi_4Ti_3O_{12}$ nanostructured microspheres. Fig 4.12 and 4.13 are representative SEM images of the products synthesized using the hydrothermal method. All the products show a spherical morphology. The insets display higher magnification SEM images providing a more detailed insight into the microstructural characteristics of the corresponding microspheres respectively.

Fig 4.12 shows the SEM images of products synthesized from 0.8 M NaOH. As seen in Fig 4.12a, the nanostructured microspheres synthesized from 0.4 g precursor powder for 3 h were 2–4 µm in diameter. The high magnification SEM images reveal a hierarchical substructure consisting of granular particles about 20 nm in size (insets of Fig 4.12a). Increasing the duration of the hydrothermal treatment to 24 h led to the formation of flowerlike nanostructured microspheres consisting of nano-platelets with a thickness of 15–20 nm (Fig 4.12b). The nanostructured microspheres synthesized from 0.1 g precursor powder for 16 h consisted of nano-platelets 20–30 nm in thickness (Fig 4.12c). The slight increase of the primary crystal thickness with decreasing precursor concentration corresponds to an increasing crystallinity observed in the X-ray powder patterns (above). The composition of the products shown in Fig 4.12b was examined by EDS (Fig 4.12d). The atomic Bi : Ti ratio was 3.908 : 2.552, which is close to the expected ratio for $Bi_4Ti_3O_{12}$. However, some sodium and carbon impurities were also detected in the sample. The sodium impurity is caused by the unavoidable surface contamination by NaOH used in the hydrothermal treatment. Carbon impurities are from the conductive rubber support.

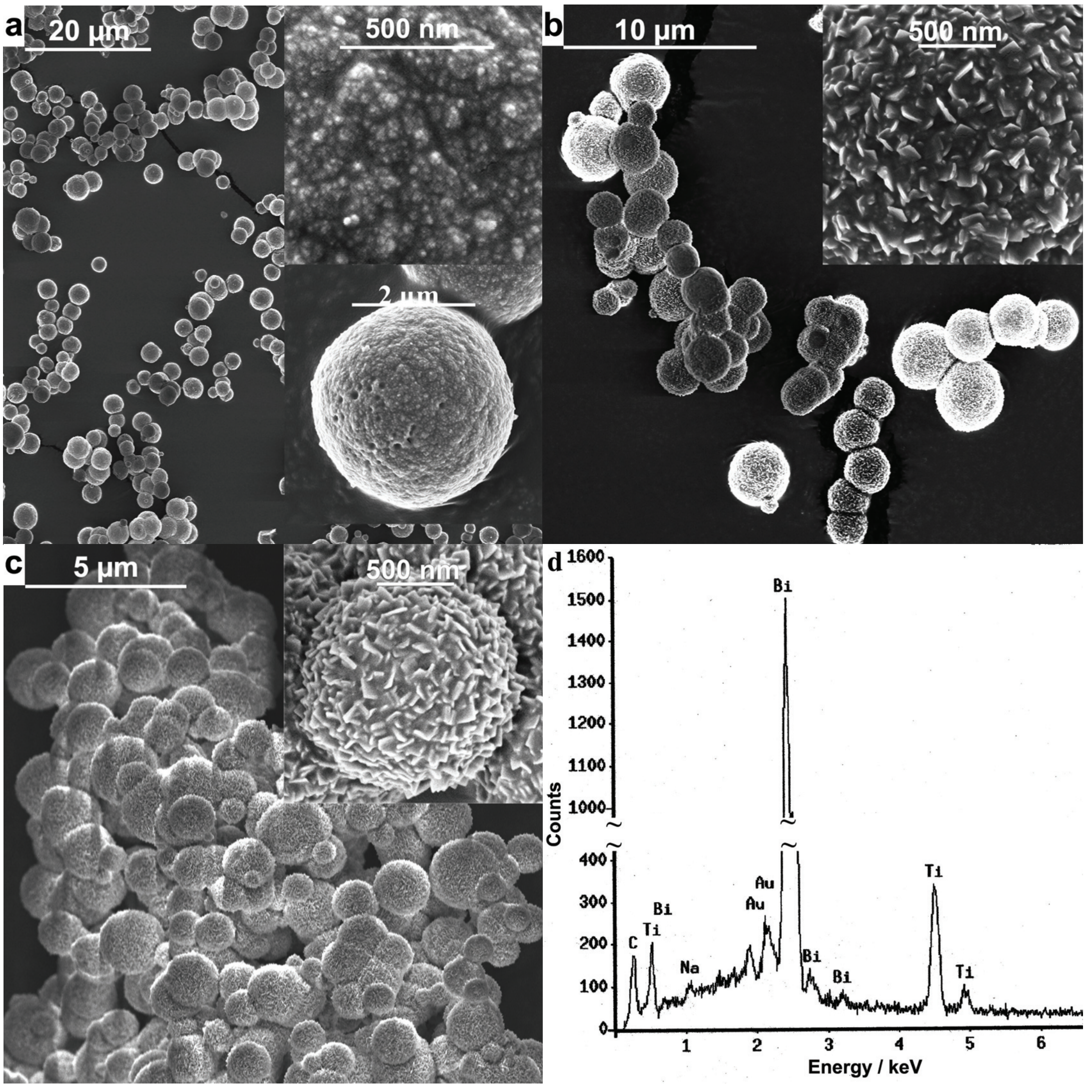

Fig 4.12 SEM images of products from hydrothermal synthesis at 180 °C, 0.8 M NaOH: (a) 0.4 g precursor powder, 3 h, (b) 0.4 g precursor powder, 24 h, (c) 0.1 g precursor powder, 16 h, and (d) EDS analysis of (b), (Insets are the higher magnification images taken from single particle or its surface).

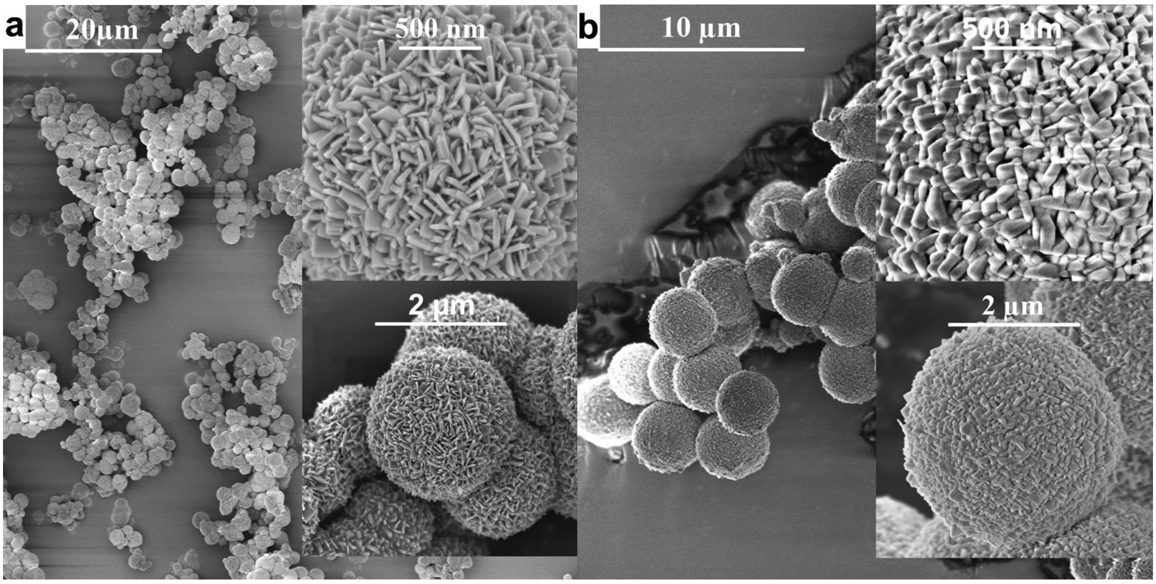

Fig 4.13 SEM images of products from hydrothermal synthesis at 180 °C, 1.0 M NaOH: (a) 0.1 g precursor powder, 16 h, (b) 0.1 g precursor powder, 24 h, (Insets are higher magnification SEM images).

SEM images of products, synthesized using a higher mineralizer concentration (1.0 M NaOH), are presented in Fig 4.13. As seen in Fig 4.13a, the nanostructured microspheres synthesized from 0.1 g precursor powder for 16 h are 1–3 μm in diameter and consist of nano-platelets with a thickness of 15–50 nm (insets of Fig 4.13a). Compared with the product synthesized from 0.8 M NaOH for the same reaction time (Fig 4.12c), the nanostructured microspheres synthesized from 1.0 M NaOH have a more tightly arranged structure and the thickness of the nano-platelets is slightly increased (insets of Fig 4.13a), demonstrating that NaOH accelerates the crystallization process. The latter observation is consistent with the XRD results.

The reaction time also has a profound effect on the structure. Extending the duration of the hydrothermal treatment to 24 h led to the formation of nanostructured microspheres consisting of dense arranged nano-platelets with a thickness of 40–90 nm, seen in the insets of Fig 4.13b. The nano-platelets (upper inset of Fig 4.13b) have round edges that are different from other samples. The latter is caused by the longer hydrothermal treatment.

Comparing Fig 4.12 and 4.13 demonstrates a gradual change from granular particles 20 nm in diameter, via lose arranged nano-platelets with a thickness of 20 nm, to tightly arranged nano-platelets with a thickness up to 90 nm by variation of synthesis conditions, such as precursor quantity, concentration of NaOH solution, and reaction time.

4.2.3 Formation Mechanism of the Nanostructured Microspheres

The precursor powder was also found to be important for the formation of products with well-defined spherical morphology. The SEM image of a product synthesized from 0.1 g ethanol-mediated coprecipitated precursor powder with 1.0 M NaOH aqueous solution at 180 °C for 24 h is shown in Fig 4.14a. Spherical as well as random aggregates are observed. However, the dried precursor powder synthesized from the DEG-mediated coprecipitation has a gel-like appearance. To understand how the nanostructured microspheres formed, the dried precursor powder from DEG-mediated coprecipitation was moderately ground and examined by SEM. As shown in Fig 4.14b, the broken section observed is a glassy substance.

No spherical morphologies are observed in the precursor. Thus, sphere formation must take place during the hydrothermal treatment.

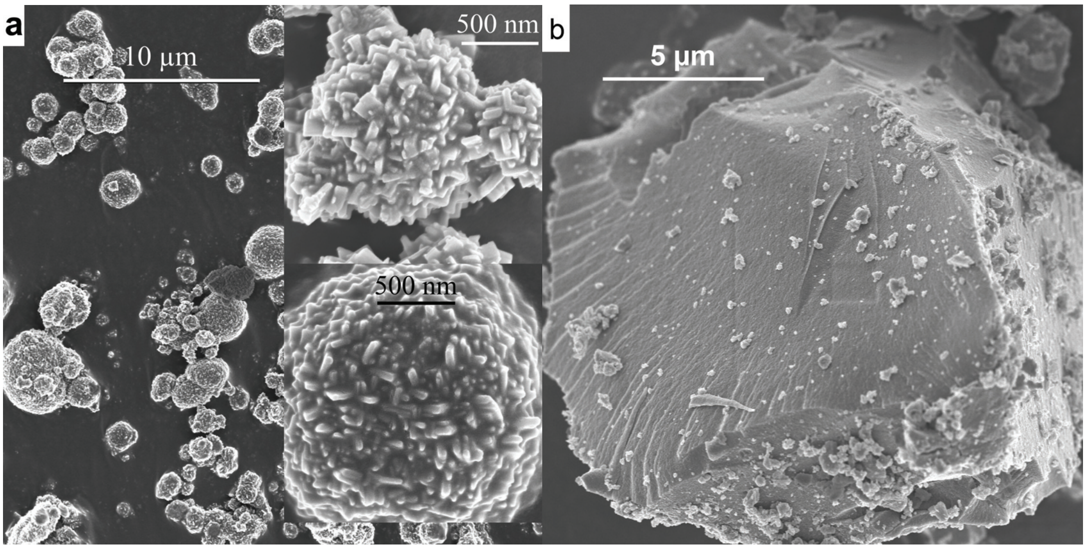

Fig 4.14 SEM images of (a) products from ethanol-mediated coprecipitates: 0.1 g precursor powder, NaOH 1 M, 180 °C 24 h (insets upper: random aggregates, lower: nanostructured microspheres) and (b) precursor powder from DEG-mediated coprecipitation.

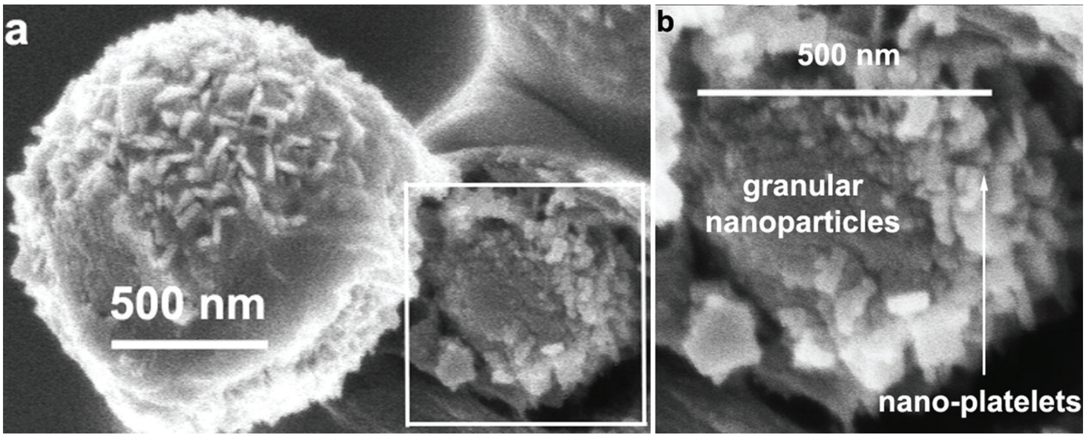

Fig 4.15 SEM images of (a) a broken nanostructured microsphere consisting of nano-platelets from 0.1 g precursor powder, 0.8 M NaOH, 16 h, (b) high magnification image of the broken section confined by the white quadrangle in (a).

SEM images of a broken nanostructured microsphere consisting of nano-platelets shed light on the formation mechanism of the nanostructured microspheres (Fig 4.15). The nanostructured microspheres consisting of nano-platelets (Fig 4.12c) were broken by grinding for 30 min and further ultrasonic agitation for 1 h. Fig 4.15a shows the SEM image of a broken microsphere. It can be seen that the nanostructured microsphere is solid and not hollow. The high magnification image of the broken section confined by the white square (Fig 4.15b), shows granular smaller particles in the core of the sphere and nano-platelets only in the outer shell.

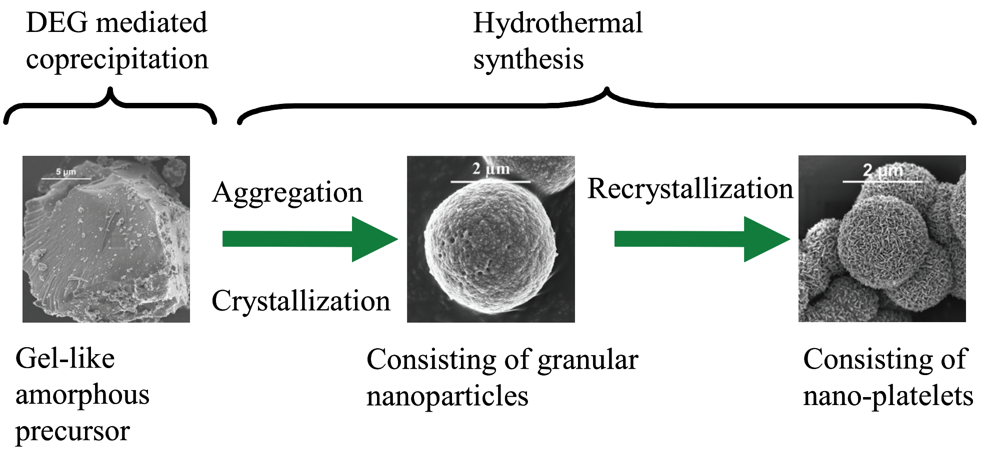

Fig 4.16 Proposed formation mechanism for $Bi_4Ti_3O_{12}$ nanostructured microspheres.

Based on the SEM results, an aggregation and recrystallization process can be proposed causing the formation of the nanostructured microspheres (Fig 4.16). In the beginning of the hydrothermal treatment primary particles of the gel-like amorphous precursor powder from DEG-mediated coprecipitation aggregate to form microspheres consisting of granular particles. In the course of the hydrothermal treatment, the granular particles forming the microspheres crystallize via a dissolution and reprecipitation mechanism forming nanosized crystalline $Bi_4Ti_3O_{12}$ particles on the outer shell of the spherical agglomerates. The latter is supported by the observation of the core-shell structure in a broken microsphere (Fig 4.15) with a nano-crystalline shell and a poorly crystallized core. This is why all the products from hydrothermal synthesis show a uniform spherical shape. A direct formation of crystalline nano-platelets and subsequent self-assembly into 3D nanostructured microspheres seems unlikely. Therefore, the proposed mechanism of formation differs from the dendritic growth mechanism proposed for nanostructured $Cu(OH)_2 \cdot H_2O$.[163] Since the granular particles forming the inner core of the spherical $Bi_4Ti_3O_{12}$ aggregates are not in contact with the NaOH solution used for the hydrothermal treatment, a poor degree of crystallinity may be expected for particles in the core of the microspheres. The XRD peaks marked by arrows may be attributed to such poorly crystallized particles in the core of the microspheres.

4.2.4 Summary

A hydrothermal synthesis method was successfully developed for the synthesis of nanostructured microspheres consisting of crystalline $Bi_4Ti_3O_{12}$. By changing the synthesis conditions, such as precursor quantity, mineralizer concentration, and reaction time, the morphologies could be tailored from 20 nm granular nanoparticles to nano-platelets with different thickness. XRD and SEM results show a higher degree of crystallinity for increasing NaOH concentration and reaction time. The formation of the nanostructured microspheres probably follows a dissolution and subsequent recrystallization process. Since several complex oxides have important electric, magnetic, and electro-optical properties, the synthesis of nanostructured complex oxides will provide new opportunities for the exploration of structure- or morphology-dependent properties. Moreover, the recrystallization process observed in the formation of $Bi_4Ti_3O_{12}$ nanostructured microspheres may be used to growth oriented $Bi_4Ti_3O_{12}$ films by hydrothermal treatment of an amorphous film coated on a substrate.

4.3 $Bi_{3.25}Pr_{0.75}Ti_{2.97}V_{0.03}O_{12}$ Nanoparticles and Ceramics

In this section, a one-pot method, using metal oxide as starting material (V_2O_5), for the preparation of ammonium metal citrate aqueous solution is presented. By introducing the ammonium metal citrate aqueous solution into a modified citrate-gel method, Pr^{3+}/V^{5+} A- and B-site cosubstituted bismuth titanate $Bi_{4-x}Pr_xTi_{3-y}V_yO_{12+y/2}$, ($x = 0.75$, $y = 0.03$, BPTV) nanoparticles and ceramics have been prepared. The structure of the BPTV ceramics was refined using the Rietveld method. The ferroelectric properties of BPTV including hysteresis behavior, saturation characteristics, leakage current density, and polarization fatigue, are discussed. Substitution of Pr^{3+} by other rare earth ions is suitable to yield other kind of cosubstitutions.

4.3.1 Synthesis

Finding or preparing proper water-soluble metal salts is a prerequisite for the citrate-gel method. There are several kinds of commercially available water-soluble lanthanide metal salts, such as acetates and nitrates, which can be readily used for A-site substitutions. Therefore, the main obstacle for chemical solution methods to A- and B-site cosubstituted $Bi_4Ti_3O_{12}$ ceramics lies in the preparation of precursor solutions of the donor cations, such as Nb^{5+}, V^{5+}, Mo^{6+}, W^{6+}, etc. for B-site substitutions.

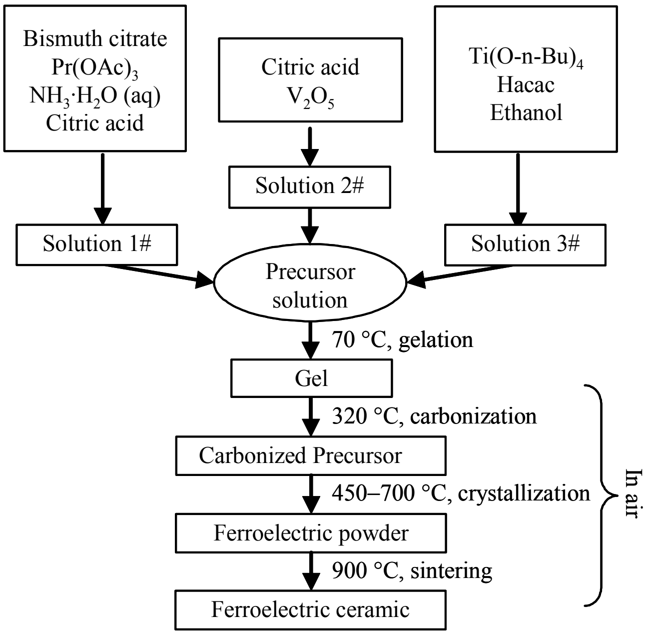

Fig 4.17 Flow diagram of the modified citrate-gel method for preparation of Pr^{3+}/V^{5+} cosubstituted $Bi_4Ti_3O_{12}$ ceramics

The modified citrate-gel process is illustrated in Fig 4.17. Bismuth citrate and praseodymium acetate was dissolved in water (former needs the help of aqueous ammonium hydroxide) (Fig 4.17, solution 1#). The vanadium citrate solution was prepared by dissolving V_2O_5 and citric acid in water (Fig 4.17, solution 2#). The as-prepared vanadium citrate solution was slightly dark green in color due to the reduction of V^{5+} into V^{3+} with citric acid. For the titanium source, a Hacac modified Ti(O-*n*-Bu)$_4$ solution in ethanol was used to reduce the moisture sensitivity of the titanium precursor solution (Fig 4.17, solution 3#). A clear precursor solution was formed when a proper total amount of ethanol was used.

A too small amount of ethanol will lead to two liquid phases while too much will cause precipitation. These phenomena can be explained by the hydrophobicity of the Ti-acac complex and the low solubility of metal citrates in ethanol. There is no separation step such as centrifugation or filtration in the whole citrate-gel process, therefore the composition of the solid is close to that of the starting gel composition. However, a small excess of bismuth is advantageous as discussed below. The citrate-gel process can be performed at ambient conditions allowing for convenient and feasible processing.

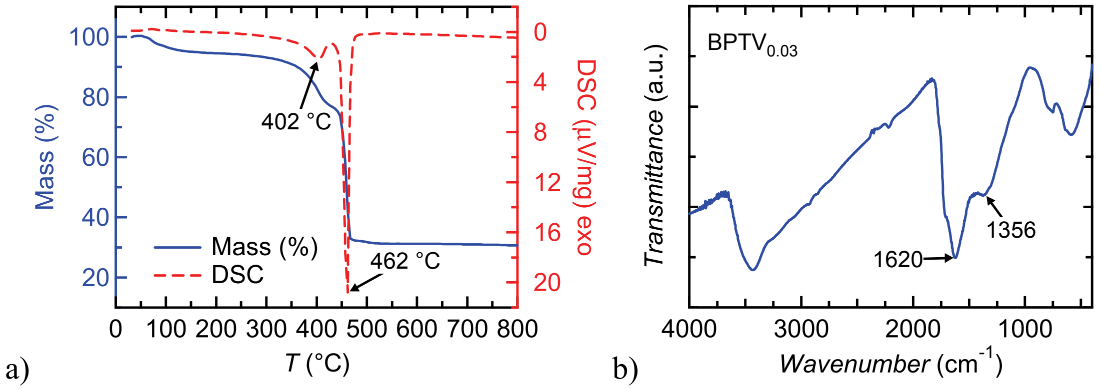

Fig 4.18 TG-DSC (a) and FTIR (b) plots of the carbonized precursor solid.

The gel is subsequently carbonized to give an amorphous intermediate. Fig 4.18a shows the TG-DSC curves of the carbonized solid. About 6 % mass loss was observed within the range of temperature from 100 to 150 °C resulting from the loss of adsorbed water. The exothermal peak at 404 °C was attributed to the decomposition of coordinated carboxyl groups, accompanied by 18 % of mass loss. The broad absorbance peaks at 1620 and 1356 cm^{-1} in the FTIR spectrum of the carbonized precursor solid (Fig 4.18b) are attributed to the CO symmetric and asymmetric stretching vibrations of the deprotonated carboxyl groups, implying the presence of residual coordinated carboxyl groups in the carbonized solid. The strongest exothermal peak (46 % mass loss) was observed at 462 °C (Fig 4.18a). The powder calcined at 400 °C for 1 h was still a black amorphous substance. However, peaks in the XRD pattern of the powder obtained at 450 °C for 1 h can be attributed to crystalline $Bi_4Ti_3O_{12}$ (Fig 4.19a). The exothermal peak at 462 °C probably results from burning of carbon produced by the decomposition of $-CH_x$ groups. The crystallization might be promoted by the released combustion enthalpy of the carbon, causing a low crystallization temperature of 450 °C.

Fig 4.19 shows the XRD patterns of calcined powders. The peak width decreases and the peak intensity increases with the calcination temperature. Below 450 °C, the calcined product was X-ray amorphous. A small impurity peak attributed to Bi_2O_3, as marked by a star in Fig 4.19a, was observed that might be attributed to the excess of bismuth used for compensation of bismuth loss during the sintering process. No impurity peak was detected after calcination above 500 °C, and all reflections can be well indexed to the $Bi_4Ti_3O_{12}$ structure despite some shifting, overlapping or changing in intensity observed. The above observations are in agreement with a direct transformation of the amorphous carbonized solid into a crystalline phase with $Bi_4Ti_3O_{12}$ structure. An intermediate phase, such as the pyrochlore phase, or fluorite phase,[164] was not observed.

The morphology and microstructure of the powder and ceramic was characterized by SEM. Fig 4.20a shows a typical SEM image of a powder sample synthesized at 500 °C. The particles are relatively uniform in size. The high magnification SEM image is shown in the inset, from which the particles can be observed more clearly. Investigation of various regions of the sample gave similar results with respect to the particle size and shape. The size distribution of the particle observed in the SEM image is given in Fig 4.20b from counting 100 randomly selected particles. The size of the particles ranged from 30 to 100 nm with a mean size of about 57 nm and a standard deviation of 14 nm.

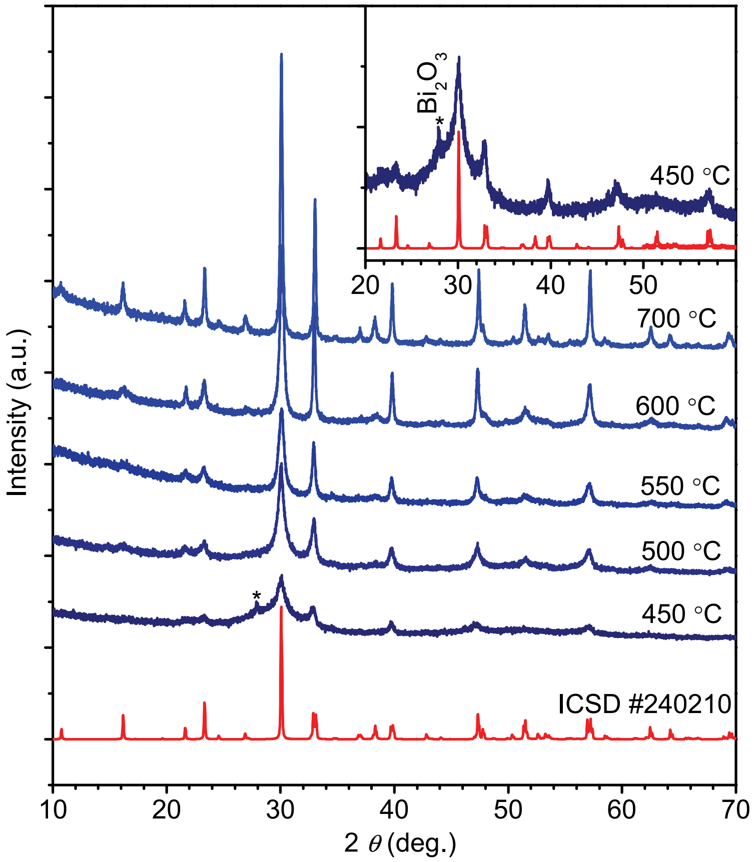

Fig 4.19 XRD powder patterns of carbonized gels calcined at different temperature for 1 h.

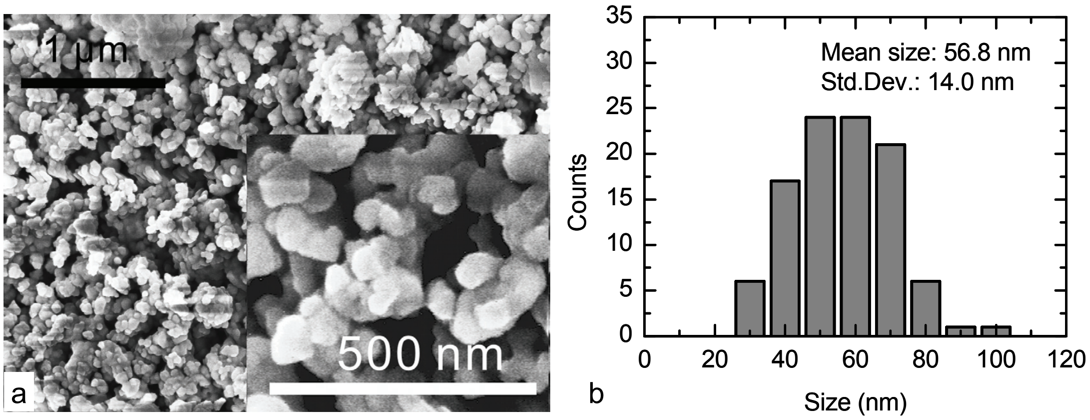

Fig 4.20 (a) SEM image of as prepared BPTV powder (inset: high magnification), (b) size distribution for randomly selected 100 particles in (a).

Fig 4.21a shows the SEM images of a ceramic sample, showing a uniform and dense structure. The grains in the ceramic were plate-like particles as observed in the high magnification SEM image in the inset of Fig 4.21a. No pores or cracks were observed. The dark areas in the SEM image are from the surface of crystallites while the light areas correspond to the edges. From the SEM images, it was found that the platelets were randomly arranged in the ceramic. No preferred orientation is observed. The composition of the ceramic was characterized by EDS given in Fig 4.21b. The atomic ratio for Bi : Pr : Ti measured was 3.25 : 0.76 : 2.85, and was close to the desired value of 3.25 : 0.75 : 2.97.

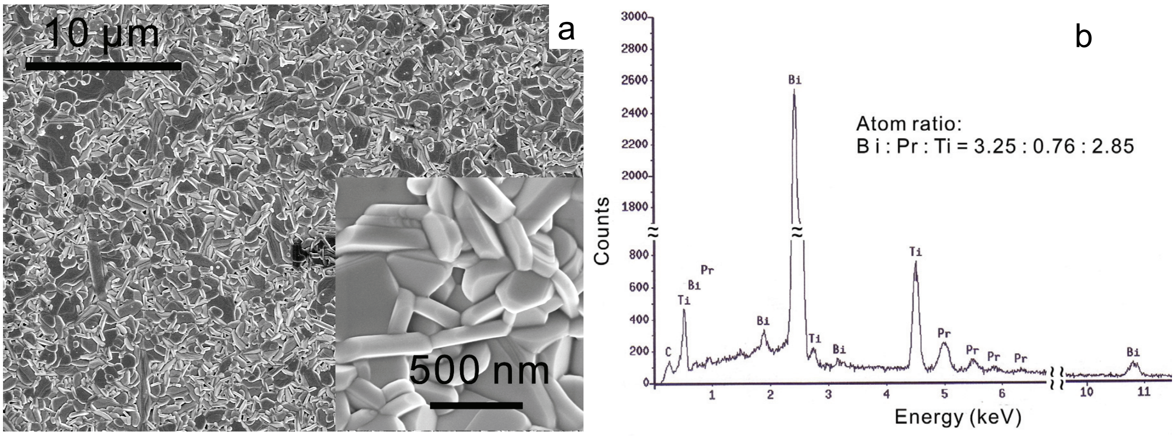

Fig 4.21 (a) SEM image of the BPTV ceramic (inset: high magnification), (b) EDS spectrum from (a).

4.3.2 Structure Refinement

According to powder neutron diffraction experiments, $Bi_4Ti_3O_{12}$ is orthorhombic and crystallizes in the space group *B*2*cb*[165] (standard setting is *Aea*2, former *Aba2*) at room temperature. However, an agreement on the structure of lanthanoid substituted $Bi_4Ti_3O_{12}$ has not been reached. Chon et al. has suggested a tetragonal structure for the praseodymium substituted bismuth titanate ($Bi_{4-x}Pr_xTi_3O_{12}$, x = 0.85) showing no peak splitting of (*h*0*l*)- and (0*kl*)-type reflections* in the powder XRD data.[166] Garg et al. confirmed the orthorhombic structure for Nd-substituted bismuth titanate ($Bi_{4-x}Nd_xTi_3O_{12}$, x = 0.85) by the observation of the (014), (125) and (034) reflections* using neutron powder diffraction.[167] In the case of La-substituted bismuth titanate ($Bi_{4-x}La_xTi_3O_{12}$, x = 0.5), Jeon et al. suggested a monoclinic *B*1*a*1 space group being more suitable according to the final weighted *R* factors (R_{wp}) and the 'goodness of fit' indicators ($S = R_{wp}/R_{exp}$) of a combined refinement of neutron and X-ray powder diffraction data.[168] On the other hand, a larger remanent polarization of 32 $\mu C/cm^2$ has been observed in highly *a*-axis oriented $Bi_{4-x}La_xTi_3O_{12}$ (x = 0.75) films,[30] which was comparable with the P_r value of 36 $\mu C/cm^2$ measured in parallel to the *a-b* plane of $Bi_{4-x}La_xTi_3O_{12}$ (x = 0.45) of a single crystal.[26] Meanwhile, large P_r values (50 $\mu C/cm^2$ for $Bi_{4-x}Nd_xTi_3O_{12}$, x = 0.85) were also observed in *c*-axis oriented films.[31]

Considering the relation between ferroelectric properties and the crystal structure and the lack of consensus on the structure of lanthanoid substituted $Bi_4Ti_3O_{12}$, the Rietveld method was used to refine the crystal structure of as-prepared BPTV. The structure models used for the Rietveld refinement were built by partially occupying the perovskite A-site with Pr^{3+} in the $Bi_4Ti_3O_{12}$ crystal structures. The ICSD data (No. 240210) were used as initial parameters for the orthorhombic $Bi_4Ti_3O_{12}$ structure refinement. Vanadium was not taken into account due to its low substitution level and atomic number being similar to that of the substituted

---

* Indices were assigned using *B*2*cb*, a nonstandard setting of S.G. 41.

titanium. The atomic coordinates and isotropic atomic displacement parameters were refined. The atomic occupancy of Bi/Pr was fixed at 0.375/0.625 presuming the ratio of Bi/Pr was 3.25 : 0.75. After refinement, the structure was transformed from space group *B*2*cb* to *Aea*2 by rotating axes and coordinates according to *a b c* = *b*' *c*' *a*'. The refined lattice and atomic parameters are listed in Table 4.3 and 4.4.

Table 4.3 Refined lattice parameters of BPTV ceramic in space group *Aea*2[a].

	Refined	ICSD#240210
a (Å)	5.4060(3)	5.41014(11)
b (Å)	32.8492(2)	32.8565(7)
c (Å)	5.4145(8)	5.44513(11)
Vol. (Å^3)	961.54(2)	967.91(9)
ρ_{calc} (g/cm^3)	7.741	
R_{wp} (%)	5.01	
R_p (%)	4.24	
D_{wd}	1.134	
Reduced χ^2	1.430	
Variables	25	
Wave length	Cu $K_{\alpha 1}$	
Geometry	transmission	
Monochromator	Ge(111)	
Temperature (K)	298	

[a] Parameters were transformed from space group *B*2*cb* to *Aea*2 by rotating axes and coordinates according to *a b c* = *b*' *c*' *a*'.

Table 4.4 Refined atomic parameters in space group *Aea*2.

Atoms	x	y	z	Occupancy	Uiso (Å^2)
Pr1	0.9966(4)	0.0668(7)	0.00000	0.375	0.019(0)
Bi1	0.9966(4)	0.0668(7)	0.00000	0.625	0.019(0)
Bi2	0.0167(5)	0.2109(9)	0.0062(2)	1.0	0.022(5)
Ti1	0.00000	0.50000	0.0329(9)	1.0	0.011(4)
Ti2	0.0047(2)	0.3717(6)	0.0308(9)	1.0	0.011(0)
O1	0.2626(0)	0.0084(2)	0.3110(9)	1.0	0.005(2)
O2	0.2469(6)	0.2499(3)	0.2636(6)	1.0	0.001(7)
O3	0.0723(2)	0.4415(8)	0.0589(8)	1.0	0.003(9)
O4	0.9506(2)	0.3189(6)	0.0392(9)	1.0	0.001(2)
O5	0.2302(2)	0.1124(6)	0.2734(9)	1.0	0.011(8)
O6	0.2984(2)	0.8761(6)	0.3431(9)	1.0	0.001(6)

Fig 4.22 gives the refined profiles of the XRD powder pattern of BPTV using a pseudo-Voigt peak function. The refined profile results in a good fit for the experimental data. As seen in the inset of Fig 4.22, the (140) diffraction peak in the space group *Aea*2 ((014) in *B*2*cb*) is detected. This result is consistent with Garg et al's observation in $Bi_{4-x}Nd_xTi_3O_{12}$ (x = 0.85).[167] The final weighted *R* value (R_{wp}) and the 'goodness of fit' (χ^2) for the orthorhombic structure were 5.01 % and 1.430 respectively, as listed in Table 4.3. Chon et al. have suggested a tetragonal structure for $Bi_{4-x}Pr_xTi_3O_{12}$ (x = 0.85).[166] However, no atomic coordinates, temperature factors, and atomic occupancies are provided in their report. The monoclinic structure suggested for $Bi_4Ti_3O_{12}$[168] did not result in a convergent

refinement for the cosubstituted samples reported in this work.

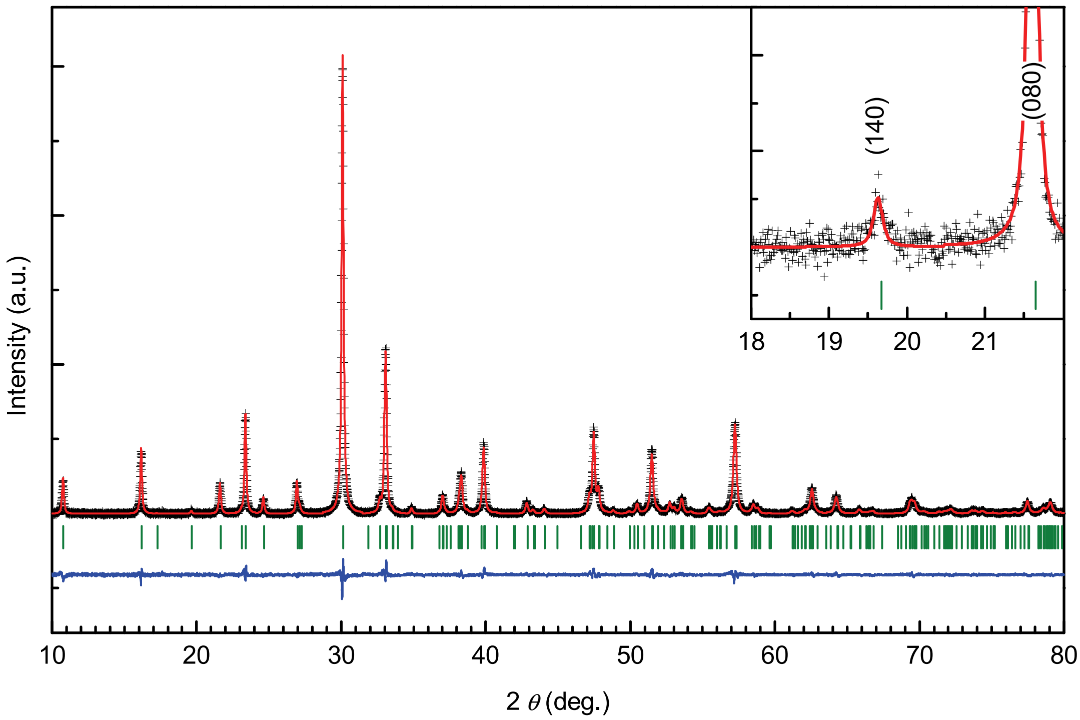

Fig 4.22 Difference plots of the BPTV (x = 0.75, y = 0.03) ceramic after the Rietveld refinement based on the orthorhombic model using space group *Aea2*, inset shows (140) diffraction peak.

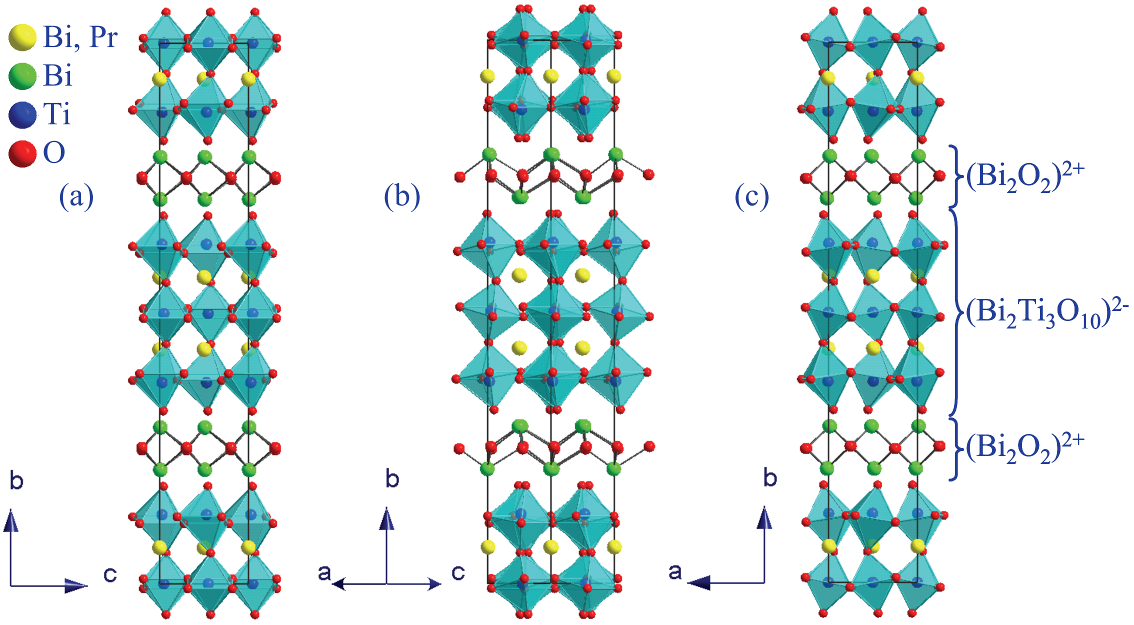

Fig 4.23 Refined BPTV crystal structure viewed along (a) [1 0 0], (b) [1 0 1], and (c) [0 0 1] directions.

As listed in Table 4.3, the final refined cell parameters were $a = 5.4060(3)$ Å, $b = 32.8492(2)$

Å, c = 5.4145(8) Å, and V = 961.54(2) Å^3 in the space group *Aea*2. As compared with $Bi_4Ti_3O_{12}$, only a small decrease of the lattice constants (0.0041, 0.0073, and 0.0305 Å for a, b, and c) was observed, resulting in a slight decrease of 6.38 Å^3 for the cell volume. The decrease of the c (a for *B*2*cb*) parameter and the cell volume for BPTV is consistent with the same trend observed in Pr^{3+},[166] Nd^{3+},[31] and La^{3+}[26] substituted $Bi_4Ti_3O_{12}$. This might be attributed to the larger effective radii of 1.17 Å for Bi^{3+}cations than that of 1.126 Å for Pr^{3+} cations with a coordination number of 8.[169] Fig 4.23 presents the crystal structure of BPTV projected along different directions using the final refined parameters. Even though absorption correction in transmission geometry is a concern for materials containing heavy atoms, the refinement resulted in satisfactory R-values.

4.3.3 Ferroelectric Properties

The as-prepared BPTV ceramic shows a well saturated *P*-*E* hysteresis loop, as seen in Fig 4.24a. The $2P_r$ and $2E_c$ values were 35 μC/cm^2 and 148 kV/cm, respectively. The switch current density reached a maximum value at the drive field of about $\pm E_c$ (Fig 4.24.b). A comparison between the BPTV ceramic and other lead free ferroelectric bulk ceramics and thin films is given in Table 4.5. The polarization P_r obtained is comparable with reported values, 12–19 and 8.5–17 μC/cm^2 for $Bi_{3.5}Pr_{0.5}(Ti,V)_3O_{12}$[35] and $(Bi, La)_4(Ti,V)_3O_{12}$[35, 92] films respectively. However, the P_r of the BPTV ceramic is lower than that of 37 μC/cm^2 observed in $Bi_{3.5}Nd_{0.5}Ti_{2.98}V_{0.02}O_{12}$ film.[35, 36] This can be explained by the larger structural distortion resulting from Nd^{3+} substitution as compared with Pr^{3+} substitution,[35, 167] because the ionic radius of Nd^{3+} (1.109 Å) is smaller than that of Pr^{3+} (1.126 Å) for a coordination number of 8.[169] Compared with other lead-free ceramics, the P_r of the prepared BPTV ceramic is comparable with that of pure $Bi_4Ti_3O_{12}$,[23] $Bi_4(Ti,V,W)_3O_{12}$,[23, 24] $Bi_{0.5}(Na_{0.8}K_{0.2})_{0.5}TiO_3$,[170] and $(Bi_{0.5}Na_{0.5})_{0.94}Ba_{0.06}TiO_3$[171] ceramics (Table 4.5), and is nearly twice the value observed for sol-gel derived $SrBi_2Ta_2O_9$[172] and citrate-nitrate gel derived $SrBi_4Ti_4O_{15}$[139] ceramics.

The measurements of $2P_r$ and $2E_c$ were carried out for different ceramic samples with identical composition and on different areas of a same ceramic showing good reproducibility. The saturation properties were characterized by the evolution of $2E_c$, $2P_r$, and P_{max} with E_{max}.

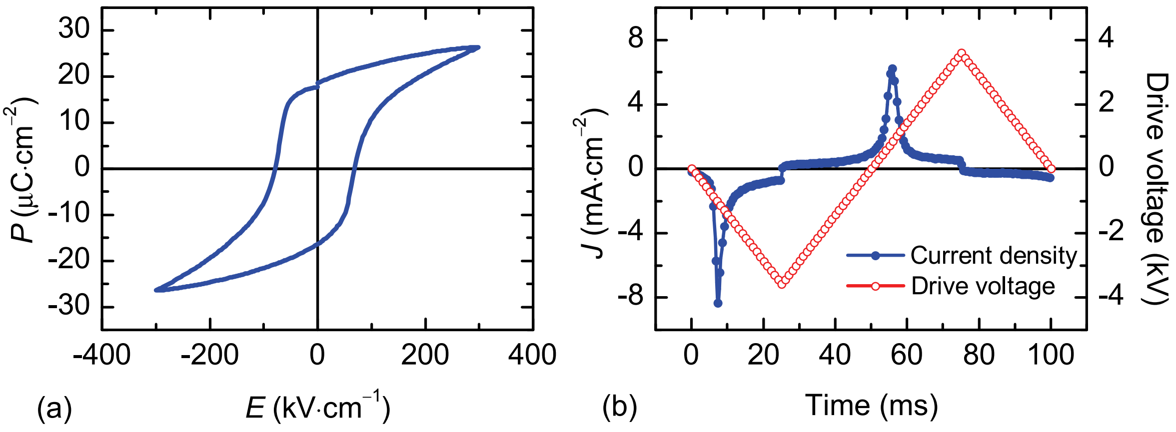

Fig 4.24 (a) *P-E* hysteresis loop of as-prepared ceramic (b) curves of switching current density and drive voltage as functions of time.

Table 4.5 Comparison of the properties for BPTV ceramics and other lead free ferroelectric bulk ceramics and thin films.

Composition	Form^a	P_r ^{b}	E_c ^{c}	E_{max} ^{c}	Growth method	Condition
$Bi_{3.5}Pr_{0.5}(Ti,V)_3O_{12}$	F	12–19	114–132	400	CSD[35]	750 °C, 5 min
$(Bi, La)_4(Ti,V)_3O_{12}$	F	8.5-17	48–135	300–400	CSD,[35] MOCVD[92]	680–750 °C
$Bi_{3.5}Nd_{0.5}Ti_{2.98}V_{0.02}O_{12}$	F	37	116	400	CSD[35, 36]	750 °C, 5 min
$Bi_4Ti_3O_{12}$	C	13	30	200	solid state [23]	850 °C, 2 h, O_2
$Bi_4(Ti,V,W)_3O_{12}$	C	18–20	~40	200	solid state [23, 24]	1050 °C, 2 h
$Bi_{0.5}(Na_{0.8}K_{0.2})_{0.5}TiO_3$	C	20	~3	4	solid state[170]	1100 °C, 2 h
$(Bi_{0.5}Na_{0.5})_{0.94}Ba_{0.06}TiO_3$	C	~20	/	/	solid state[171]	1200 °C, 2 h
$SrBi_2Ta_2O_9$	C	7.6	22	~ 40	sol-gel[172]	1200 °C, 8 h
$SrBi_4Ti_4O_{15}$	C	8	42.5	80	citrate-nitrate[139]	1060 °C, 1 h
$Bi_{3.25}Pr_{0.75}Ti_{2.97}V_{0.03}O_{12}$	C	17	74	300	citrate-gel*	900 °C, 4 h
$Bi_{3.25}Pr_{0.75}Ti_3O_{12}$	C	12	58	250	citrate-gel*	900 °C, 4 h

a ‘F’ represents film, ‘C’ represents ceramic, *b* in μC/cm^2, *c* in kV/cm, *this dissertation.

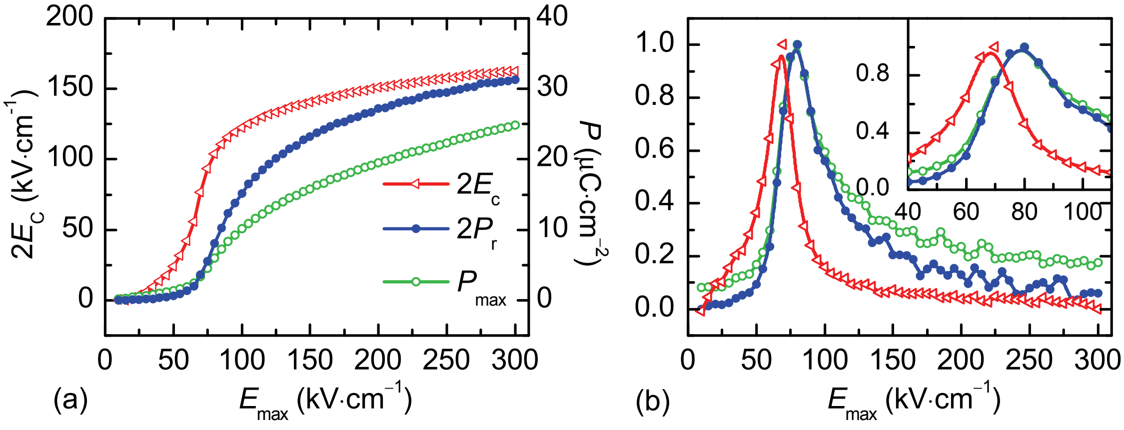

Fig 4.25 (a) $2E_c$, $2P_r$, and P_{max} as a function of E_{max}, (b) normalized plots of $d(2E_c)/d(E_{max})$ (triangle), $d(2P_r)/d(E_{max})$ (hollow circle), and $d(P_{max})/d(E_{max})$ (solid circle, inset: details of the peaks)

As seen in Fig 4.25a, the $2E_c$, $2P_r$, and P_{max} showed similar behavior. Their values show a pronounced increase within the range of E_{max} from 50 to 100 kV/cm, whereas above ($E_{max} >$ 100 kV/cm) a more gradual increase was observed. These saturation properties were more apparent in the first derivative shown in Fig 4.25b. The values of $d(2P_r)/d(E_{max})$ and $d(P_{max})/d(E_{max})$ had maxima at the same E_{max} of 80 kV/cm, and 70 kV/cm for that of $d(2E_c)/d(E_{max})$. These values are coincidentally close to the E_c of 74 kV/cm from the hysteresis with 300 kV/cm of E_{max}, as shown in Fig 4.24. This coincidence is confirmed using an ideal ferroelectric capacitor model,[173] in which the ferroelectric has a field independent dielectric constant (ε_{fe}) and an ideal switching behavior (the ferroelectric polarization is zero below E_c and has a constant value (P_s, spontaneous polarization) above E_c). The electric displacement (D) in the ideal ferroelectric capacitor therefore consists of two components and can be expressed as:

$$D = P_s + \varepsilon_0 \cdot \varepsilon_{fe} \cdot E \quad \textbf{Eq 4.4}$$

Here ε_0 is the vacuum permittivity.

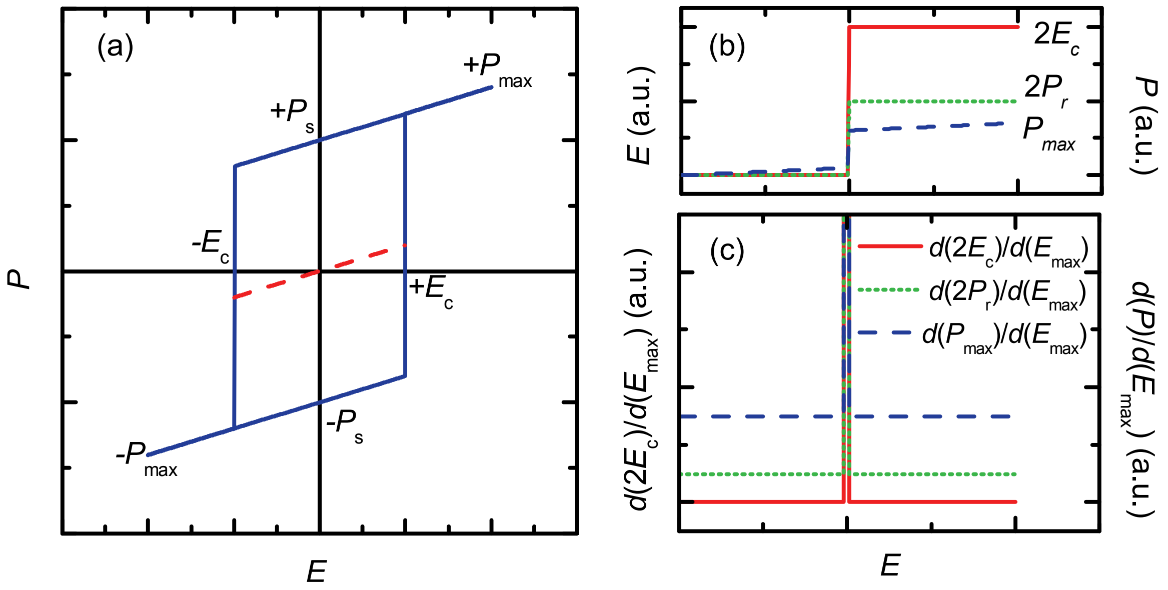

Fig 4.26 Plots from the ideal ferroelectric capacitor model: (a) hysteresis loop (dashed line: below E_c, solid line: above E_c), (b) $2E_c$, $2P_r$ ($P_r = P_s$), and P_{max} vs. E_{max}, and (c) differentiated curves of (d).

Fig 4.26a shows the hysteresis loop based on the ideal ferroelectric capacitor model. Obviously, the measured $2E_c$ and $2P_r$ (P_r equals P_s in the ideal model) are zero below E_c and have a constant value above E_c, while the P_{max} (measured D value) has a linear relationship with electric field but an abrupt increase at E_c (Fig 4.26b). Their differentiated curves will have sharp peaks at E_c, as illustrated in Fig 4.26c. In a ceramic sample, these peaks are broadened due to different domains with different E_c (caused by domain-wall pinning) and different polarization (caused by domain orientation). Therefore, the peak positions observed in the experimental plots of $d(2P_r)/d(E_{max})$, $d(P_{max})/d(E_{max})$, and $d(2E_c)/d(E_{max})$ indicate statistical values in terms of E_c, suggesting the validity of using these plots within a range of relatively low E_{max} to estimate the E_c value at highly saturated conditions (or denoted as saturated E_c). This treatment has advantages especially in two cases. One case is that a material with larger E_c makes it difficult to achieve saturated hysteresis loops. The other case is a material with a low breakdown electric field resulting from a high leakage current. In the latter case, failure of the measurement will occur before saturation is observed in the hysteresis loop. In both cases, it will be difficult to get the saturated E_c value directly from a P-E hysteresis loop measurement.

The saturation properties can also be expressed by using the ratio of P_{max}/P_r. As seen in Fig 4.27, the value of P_{max}/P_r decreases with E_{max} but reaches a constant value above 75 kV/cm of E_{max}, in agreement with the E_c obtained from the saturated hysteresis loop as discussed above. The inset of Fig 4.27 shows that P_{max}/P_r increases linear with E_{max} at $E_{max} > 100$ kV/cm. The linear relationship is held above E_c in an ideal ferroelectric capacitor as obtained from Eq 4.4:

$$\frac{P_{max}}{P_r} = \frac{P_{max}}{P_s} = 1 + \frac{\varepsilon_0 \cdot \varepsilon_{fe}}{P_s} \cdot E_{max} \qquad \textbf{Eq 4.5}$$

Here the y-intercept equals one, and the slope equals $\varepsilon_0 \cdot \varepsilon_{fe}/P_s$.

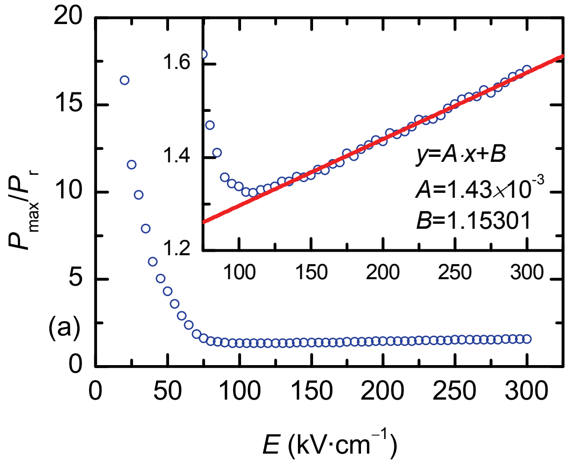

Fig 4.27 Plots of P_{max}/P_r vs. E_{max}, and inset: linear fitted plots.

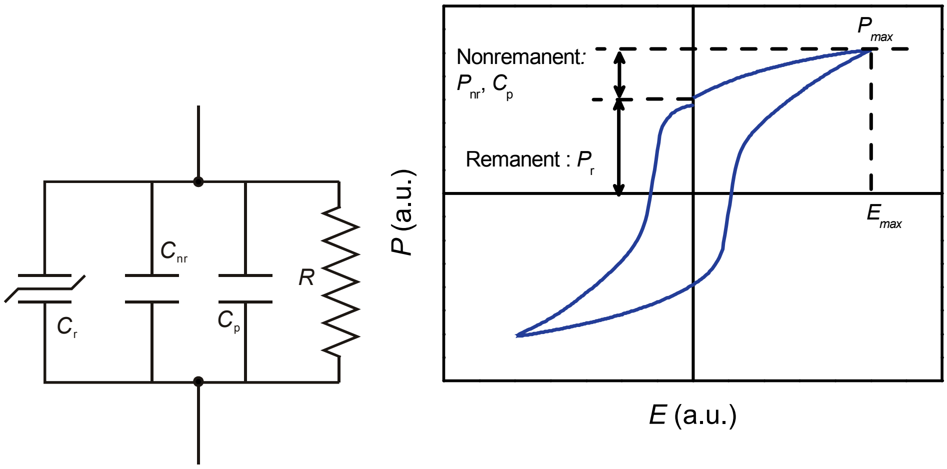

Fig 4.28 Four components model for a ferroelectric capacitor (left) and illustration of contributions of these components to P_{max} with omitting the leakage current (right).

As far as a real ferroelectric ceramic capacitor is concerned, four current sources should be taken into account (a four parallel components model[174]): remanent polarization produced by uncoupled domains (P_r from C_r), nonremanent polarization due to coupled domains in a ferroelectric capacitor (P_{nr} from C_{nr}), parallel parasitic capacitance from field independent dielectric constant (C_p: $\varepsilon_0 \cdot \varepsilon_{fe} \cdot E$), and resistive leakage (J from R), as illustrated in Fig 4.28 (left). The measured P_{max} therefore can be expressed using these four components (Fig 4.28):

$$P_{max} = P_r + P_{nr} + \varepsilon_0 \cdot \varepsilon_{fe} \cdot E_{max} + \int J(t)dt \qquad \textbf{Eq 4.6}$$

For a low leakage current ferroelectric material, the contribution of the last component can be omitted (Fig 4.28, right). Therefore, the value of P_{max}/P_r is deduced as:

$$\frac{P_{max}}{P_r} = 1 + \frac{P_{nr}}{P_r} + \frac{\varepsilon_0 \cdot \varepsilon_{fe}}{P_r} \cdot E_{max} \qquad \textbf{Eq 4.7}$$

When the E_{max} is lower than E_c, few domains can be switched by such low electric field, thereby, both P_r and P_{nr} is close to zero. So the value of P_{max}/P_r is dominated by E_{max}/P_r. This is consistent with the result in the low electric field range as observed in Fig 4.27. On the other hand, when the E_{max} is above E_c, both P_r and P_{nr} will increase with E_{max}. The ratio of P_{nr} and P_r might be close to a constant that is predetermined by the fractions of coupled and free (or switchable) domains, which are dependent on both the composition and preparation. Based on above hypothesis, a linear plot can be obtained only if $\varepsilon_0 \cdot \varepsilon_{fe}/P_r$ is also close to a constant. With presumption of ε_{fe} about 300, the value of $\varepsilon_0 \cdot \varepsilon_{fe}/P_r$ was 3.8–1.6 $\times 10^{-3}$ (cm/kV) when the P_r increases from 7 to 17 μC/cm^2 as observed at about 100 and 300 kV/cm in this work. The $\varepsilon_0 \cdot \varepsilon_{fe}/P_r$ shows only a slight decrease with increasing E_{max} within the high electric field range, therefore, a linear relationship between P_{max}/P_r and E_{max} will be obtained. The linear part of the plot of P_{max}/P_r vs. E_{max} has a y-intercept $B = 1 + P_{nr}/P_r$ and a slope of $\varepsilon_0 \cdot \varepsilon_{fe}/P_r$. Thus, the y-intercept allows for the estimation of $P_{nr}/P_r = B - 1$. For the studied BPTV ceramic, ε_{fe} and P_{nr} were 283 and 2.7 μC/cm^2 calculated from the fitted values of slope and y-intercept using the measured P_r of 17.5 μC/cm^2 at E_{max} of 300 kV/cm. The linear dielectric constant of 283 is reasonable for a ferroelectric $Bi_4Ti_3O_{12}$ based material that normally is in the range of one to several hundred at room temperature (Table 4.6), and P_{nr} of 2.7 μC/cm^2 is very low in comparison to 17.5 μC/cm^2 for P_r, indicating a low degree of coupling of the domains in the sample. For the studied BPTV, the value of P_{nr}/P_r from Eq 4.7 equals 0.153 using the measured P_r of 17.5 μC/cm^2 at E_{max} of 300 kV/cm. This value could be used as a factor to characterize the level or extent of domain coupling.

Table 4.6 Relative dielectric constant of $Bi_4Ti_3O_{12}$ based ceramics and films.

Materials	Form	Frequency (kHz)	ε_r
$Bi_4Ti_3O_{12}$	ceramic[24, 175, 176]	1000	71–173
$Bi_4Ti_{2.97}V_{0.03}O_{12}$	ceramic[24]	1000	131
$Bi_4Ti_{2.95}W_{0.05}O_{12}$	ceramic[175]	1000	184
$Bi_4Ti_{2.985}W_{0.015}O_{12}$	ceramic[23]	1000	150
$Bi_{3.2}Sm_{0.8}Ti_3O_{12}$	ceramic[177]	1000	280
$Bi_4Ti_3O_{12}$	film[178]	1000	236
		1.0	240
$Bi_{3.25}La_{0.75}Ti_3O_{12}$	film[28]	1000	310
		3.0	358
$Bi_{3.15}Pr_{0.85}Ti_3O_{12}$	film[166]	1000	558
		1.0	700
$Bi_{3.5}Pr_{0.5}Ti_{2.99}Mo_{0.01}O_{12}$	film[32]	1000	264
		1.0	275
$Bi_{3.15}Nd_{0.85}Ti_{2.08}W_{0.02}O_{12}$	film[33]	1000	480
		1.0	516

Fig 4.29a presents the logarithmic scale J-E curves, showing symmetric leakage current density. It was found that J was linear with E within a range of ±200 kV/cm (Fig 4.29b). The sudden increase of J around ± 200 kV/cm might due to a change of the conductive mechanism. However, a breakdown is unlike because after leakage measurement the hysteresis loop almost has no change. The typical leakage current density was below 0.7 μA/cm^2. Based on the measured leakage current density, the contribution of leakage to the P_{max} should be much lower than 0.1 μC/cm^2. Therefore, neglecting the contribution of leakage current to the P_{max} in the four components model as discussed above was a valid assumption. The low leakage current density might be due to a reduced number of oxygen vacancies caused by the substitution of Pr^{3+} and V^{5+}.

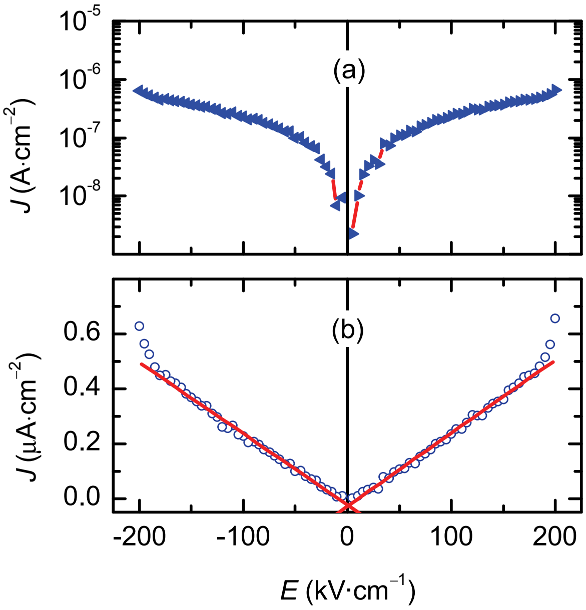

Fig 4.29 Room temperature *J-E* plots of the BPTV ceramic: (a) logarithmic scale, (b) linear scale (circles: experiment, solid line: linear fit).

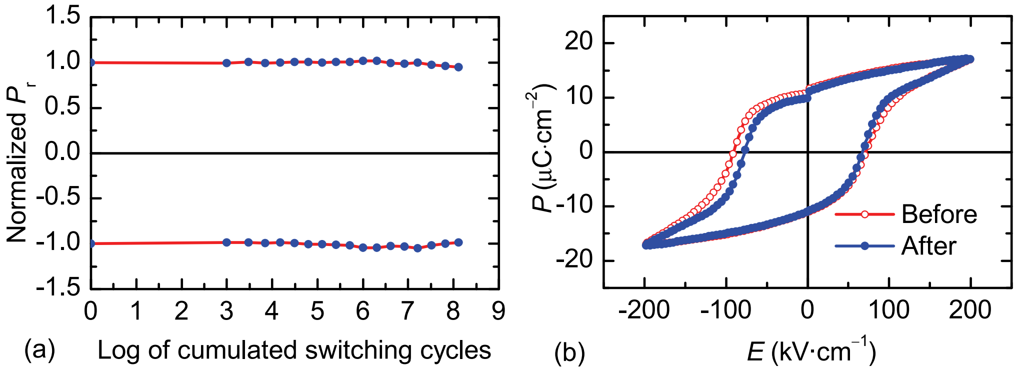

Fig 4.30 (a) Plots of P_r vs. cumulated switching cycles, (b) hysteresis loop before and after 10^8 switching cycles.

Polarization fatigue measurements show a high endurance for the as-prepared BPTV ceramic. As seen in Fig 4.30a, there was no significant decrease of ± P_r after switching over 10^8 cycles. A slight increase of ± P_r was observed around 10^6 switching cycles. Fig 4.30b gives the hysteresis loops measured before and after the polarization fatigue test, resulting in almost the same ± P_r and $\pm P_{max}$. This provides further evidence for the low polarization fatigue of the as-prepared BPTV ceramic. A small difference between the two hysteresis loops was a little decrease of $-E_c$ for the hysteresis loop measured after the fatigue test.

V^{5+} substitution has been found to be important to improve P_r in this work. The ceramic of $Bi_{3.25}Pr_{0.75}Ti_3O_{12}$ (BPT) was also prepared using the same method for comparison. As seen in Fig 4.31, the $2P_r$ of the BPT ceramic was 24 µC/cm^2 at E_{max} of 250 kV/cm, which is smaller than that of BPTV (30µC/cm^2). A slight increase of the coercive field was observed with V^{5+} substitution. However, it was failed to obtain a P-E hysteresis loop with E_{max} of 300 kV/cm for BPT ceramic before the breakdown of the sample. There are two possible ways for V^{5+} substitution that can contribute to improve the ferroelectric properties, in particular to increase P_r. Domain-wall pinning was supposed to be suppressed due to V^{5+} substitution causing a decrease of the space charge density through compensating oxygen vacancies.[23, 24, 35] On the other hand, substitution of Ti^{4+} (0.605 Å) by smaller V^{5+} (0.54 Å) may cause a local lattice distortion, which may be in favor of increase of P_r in a similar way as substitutions by lanthanide cations having smaller ionic radii than Bi^{3+}.[167] The effect of local lattice distortion caused by V^{5+} substitution may be less important than that of suppressing of domain-wall pinning by compensating oxygen vacancies due to the low substitution level.[37]

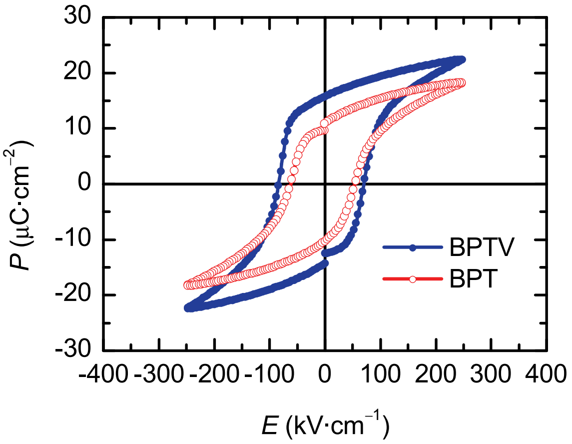

Fig 4.31 Comparison of P–E hysteresis loops between BPTV and BPT ceramics at E_{max} of 250 kV·cm^{-1}.

4.3.4 Summary

Praseodymium and vanadium cosubstituted $Bi_4Ti_3O_{12}$ nanoparticles and ceramics were synthesized using a modified citrate-gel method. The crystallization was observed as low as 450 °C. The carbonized amorphous precursor was directly transformed into crystalline BPTV with the $Bi_4Ti_3O_{12}$ structure. The synthesized nanoparticles were of uniform particle size ranging from 30 to 100 nm. The mean size was 57 nm with a standard deviation of 14 nm. The ceramic prepared from the as-synthesized nanoparticles consisted of randomly arranged platelets with a thickness of about 200 nm. The Rietveld refinement in the orthorhombic space group $Aea2$ for the as-prepared Pr^{3+} and V^{5+} cosubstituted $Bi_4Ti_3O_{12}$ resulted in a convergent refinement (R_{wp} = 5.01 %).

Ferroelectric measurements show that the as-prepared ceramics have good ferroelectric properties. A saturated P-E hysteresis loop was obtained from the as-prepared ceramic. The $2P_r$ and $2E_c$ values measured at 300 kV/cm were 35 µC/cm^2 and 148 kV/cm respectively. The observed linear relationship between P_{max}/P_r and E_{max} was interpreted as an ideal and a four components ferroelectric capacitor model for the calculation of the field independent dielectric constant and nonremanent polarization. For the BPTV ceramic studied, the calculated field independent dielectric constant was 282, and the calculated nonremanent polarization resulting from coupled domains was 2.7 µC/cm^2 at E_{max} = 300 kV/cm. The as-prepared ceramic shows ohmic conductivity. The current density was found to be below 0.7 µA/cm^2. No significant decrease of P_r was observed after switching over 10^8 cycles. The well saturated hysteresis loop, low leakage, and low polarization fatigue is promising for applications in devices.

4.4 $Bi_{3.25}La_{0.75}Ti_{3\text{-}x}M_xO_{12}$ (M = Mo, W, Nb, V) Nanoparticles and Ceramics

In this section, a one-pot method, using corresponding metal oxides as starting materials (V_2O_5, MoO_3, and WO_3), for preparation of ammonium metal citrate aqueous solution is presented. By introducing the ammonium metal citrate aqueous solution and the reported peroxy niobium citrate aqueous solution into the modified citrate-gel method, $Bi_{3.25}La_{0.75}Ti_{3\text{-}x}M_xO_{12}$, ($BLTM_x$, M = Mo, W, Nb, V, x = 0.0–0.12) powder and ceramics were synthesized. The phase purity and morphologies of the powder and ceramics were characterized by XRD and SEM. The profound effects of cosubstitutions on the texture, microstructure (grain size and orientation), and ferroelectric properties of the cosubstituted ceramics are discussed.

4.4.1 Synthesis

As seen in Fig 4.32, the modified citrate-gel process is analogous to that for the synthesis of BPTV ceramics (section 4.3). However, praseodymium acetate was replaced with lanthanum acetate for precursor solution #1, and various donor aqueous solutions were used for precursor solution #2 to vary cosubstitutions. Though V_2O_5 can be dissolved with citric acid in water above 90 °C,[179] MoO_3 and WO_3 were not completely dissolved. However, clear solutions were formed at a lower temperature (70 °C) when water was replaced with ammonia aqueous solution. This can be explained by the increase of pH value caused by introducing of aqueous ammonia solution. Firstly, increase pH value will increase the chelating ability of the carboxylic groups in the citric acid molecule. Secondly, V_2O_3, MoO_3, and WO_3 are acidic oxides. Therefore, high pH value will be in favor of the dissolution of these metal oxides with both considerations.

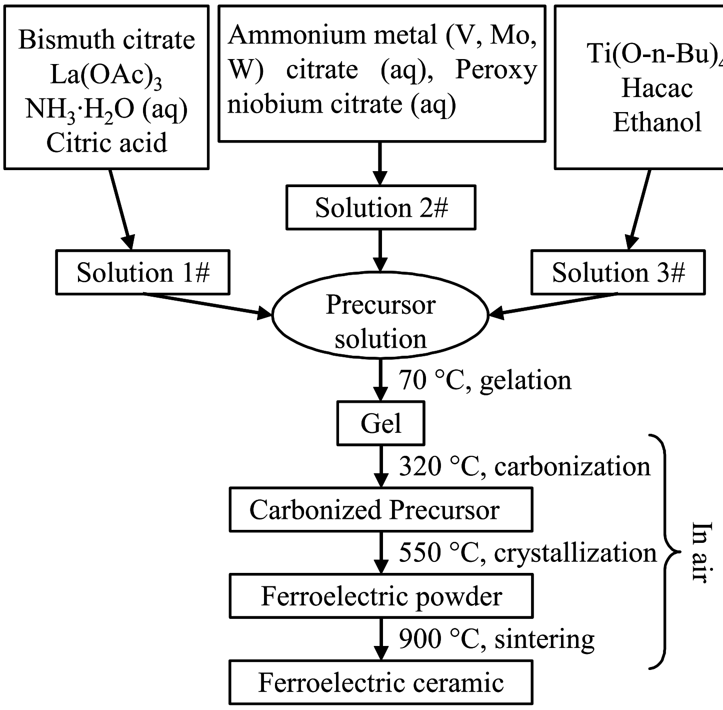

Fig 4.32 Flow diagram of the modified citrate-gel method for preparation of $BLTM_x$ (M = Nb , V, Mo, and W) ceramics.

The color of ammonium vanadium citrate aqueous solution is yellowish and colorless for the others. There were only three kind of chemicals involved in the one-pot method to prepare each ammonium metal citrate aqueous solution, and there is no need of adjusting the pH value during the whole process.

Fig 4.33a gives the TG-DSC curves of the carbonized gel, which show little difference to those of the carbonized gel for preparation BPTV ceramics.[179] About 5 % mass loss is observed in the TG plot within the range of temperature from 30 to 150 °C, which may be attributed to the loss of adsorbed water. The exothermal peak at 405 °C accompanied with 17 % mass loss, may result from the decomposition of coordinated carboxyl groups. The broad absorbance peaks at 1620 and 1356 cm^{-1} in the FTIR spectrum of the carbonized precursor solid (Fig 4.33b) are attributed to the CO symmetric and asymmetric stretching vibrations of the deprotonated carboxyl groups, implying the presence of coordinated carboxyl groups in the carbonized solid. The maximum exothermal peak at 463 °C was attributed to the burning of carbon formed by the decomposition of -CH$_x$ groups, which resulted in 49 % mass loss.

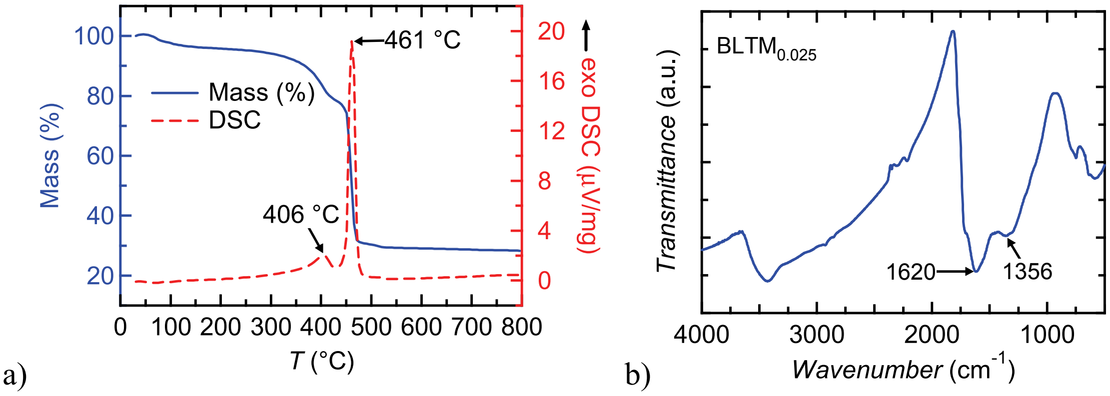

Fig 4.33 TG-DSC (a) and FTIR (b) plots of the carbonized solid (BLTMo$_{0.025}$).

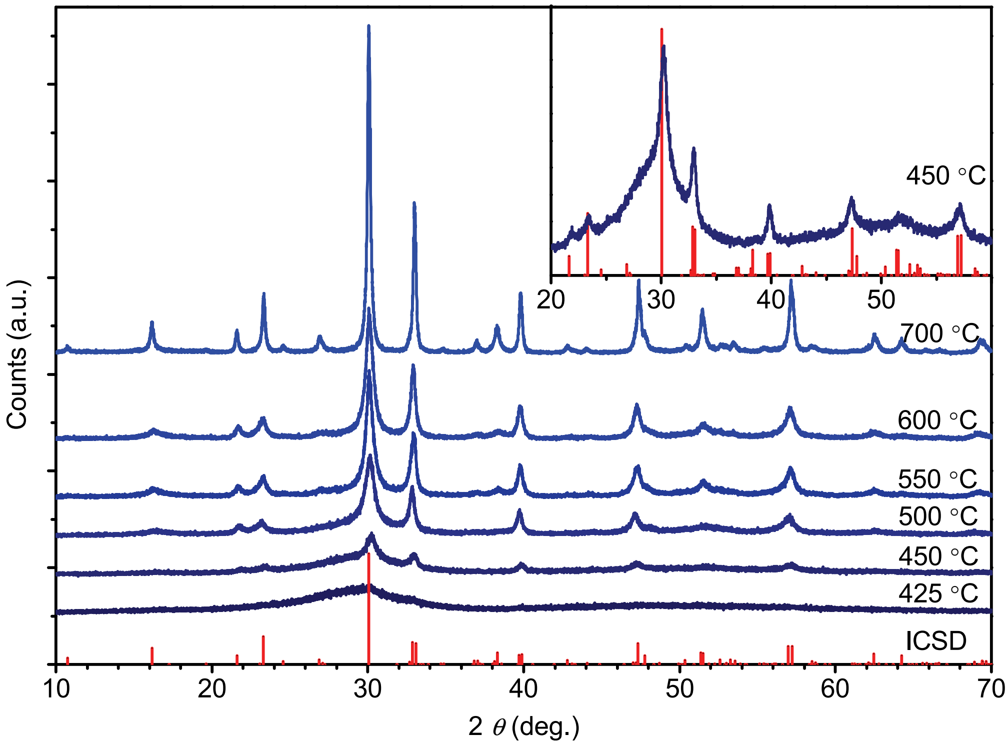

Fig 4.34 Powder XRD patterns of carbonized gels (BLT) calcined at 425–700 °C for 1 h, bottom: ICSD #240210.

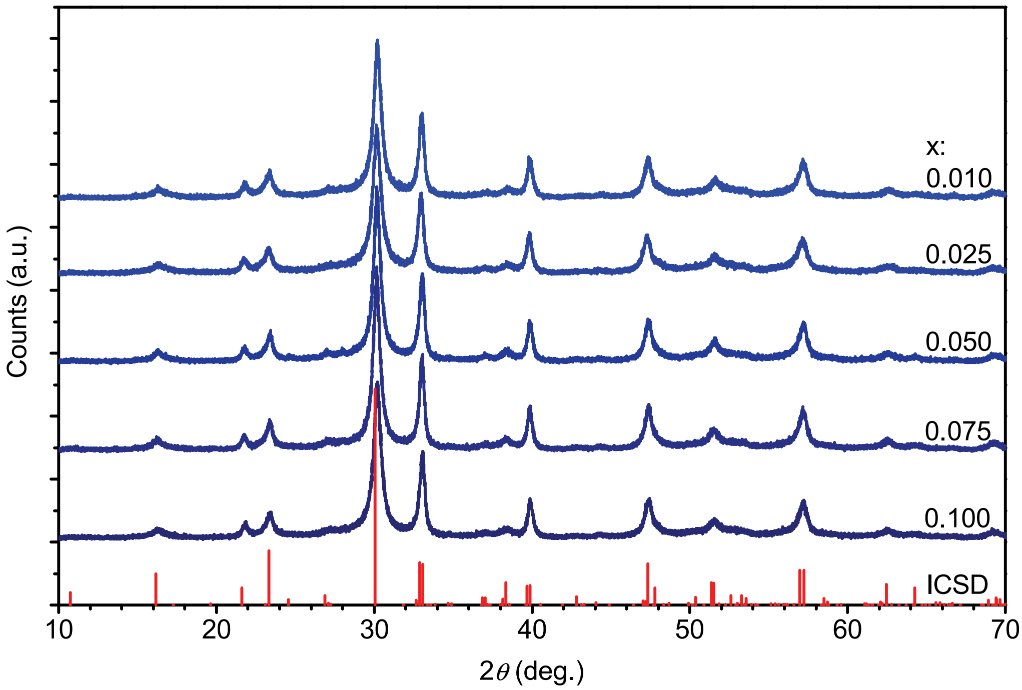

Fig 4.35 Powder XRD patterns of $Bi_{3.25}La_{0.75}Ti_{3-x}Nb_xO_{12}$, nanoparticles prepared at 550 °C for 1 h, bottom: ICSD #240210.

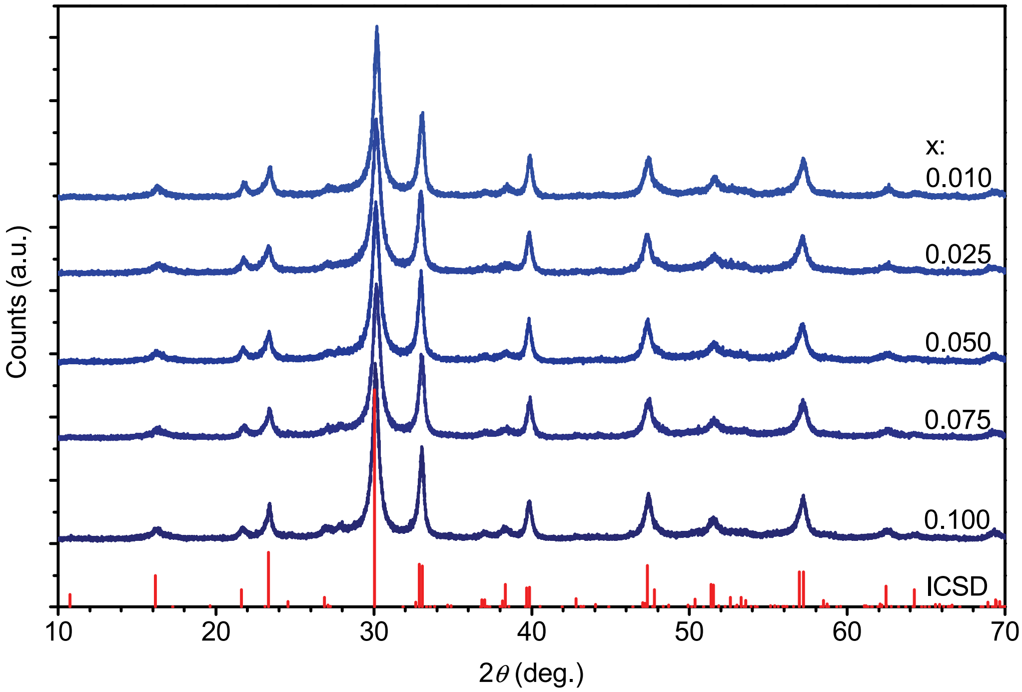

Fig 4.36 Powder XRD patterns of $Bi_{3.25}La_{0.75}Ti_{3-x}V_xO_{12}$, nanoparticles prepared at 550 °C for 1 h, bottom: ICSD #240210.

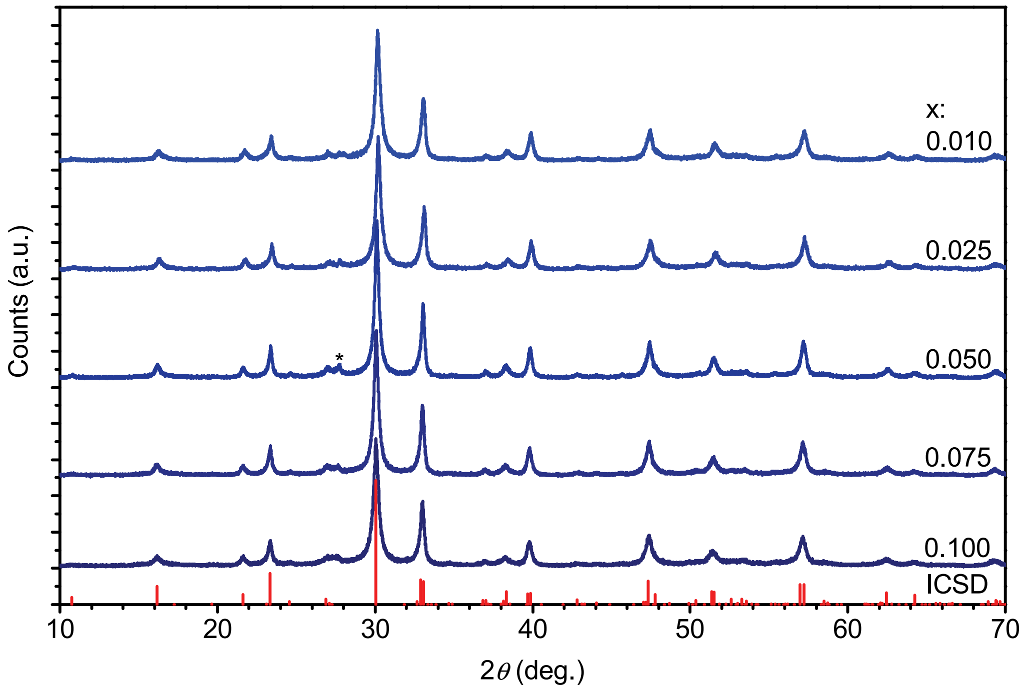

Fig 4.37 Powder XRD patterns of $Bi_{3.25}La_{0.75}Ti_{3-x}Mo_xO_{12}$, nanoparticles prepared at 550 °C for 1 h, bottom: ICSD #240210, * Bi_2O_3.

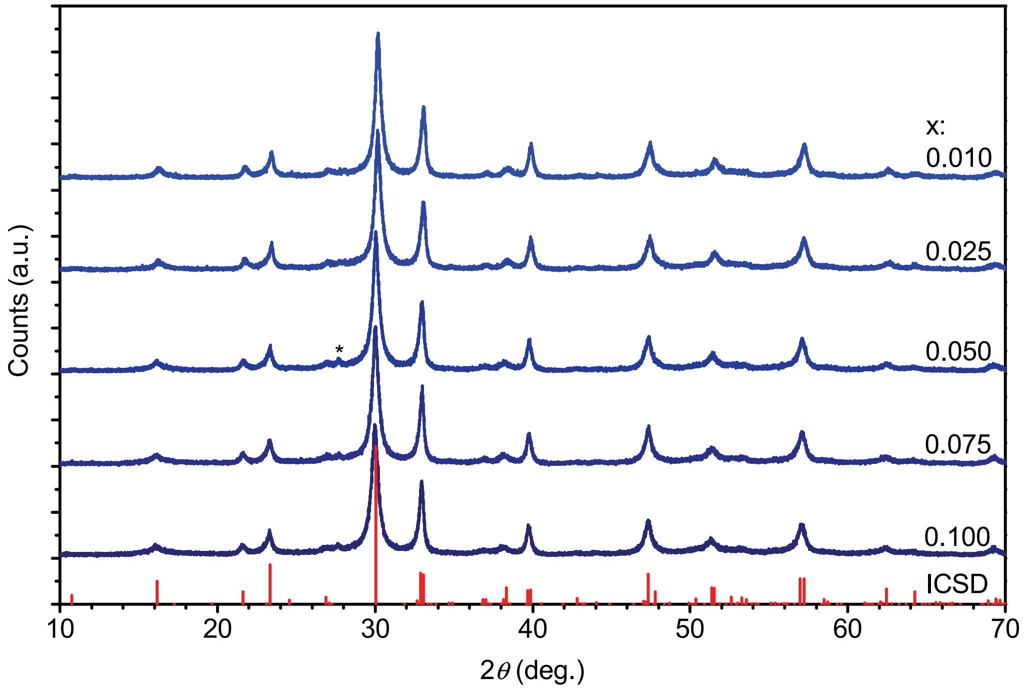

Fig 4.38 Powder XRD patterns of $Bi_{3.25}La_{0.75}Ti_{3-x}W_xO_{12}$ nanoparticles prepared at 550 °C for 1 h, bottom: ICSD #240210, * Bi_2O_3.

Considering the low cosubstitution level of the donor cations, it is convenient to start with the $Bi_{3.25}La_{0.75}Ti_3O_{12}$ to determine the crystallization conditions of the carbonized gel. The XRD patterns of the carbonized gel of $Bi_{3.25}La_{0.75}Ti_3O_{12}$, calcined at different temperature (425–700 °C) for 1 h, are shown in Fig 4.34. As seen in Fig 4.34, the calcined product at 425

°C for 1 h was X-ray amorphous. However, the XRD patterns of the products calcined at 450 °C and above for 1 h can be indexed to orthorhombic $Bi_4Ti_3O_{12}$ (Fig 4.34, inset). The crystallization temperature of 450 °C coincides with the onset of the maximum exothermal peak of 463 °C in the DSC curve (Fig 4.33), suggesting that the released combustion enthalpy of the carbon may promote the crystallization at a low temperature of 450 °C (Fig 4.34). No intermediate phase, such as fluorite phase,[164] is observed, which supports a direct transformation from the carbonized amorphous precursor to the crystalline $Bi_4Ti_3O_{12}$ structure as observed in BPTV (section 4.3).[179] The diffraction peak intensity increases with the calcination temperature, and an inverse trend is observed for the diffraction peak width, indicating the increase of crystallinity with calcination temperature.

According to the crystallization temperature of the carbonized gel, the $BLTM_x$ powders were prepared at 550 °C for 1 h. A small diffraction peak indexed to Bi_2O_3 was observed in the XRD patterns of some products (Fig 4.37, 4.38). All the others diffraction peaks can be indexed to the orthorhombic $Bi_4Ti_3O_{12}$ (ICSD #240210), even though broad diffraction peaks with overlapping was observed (Fig 4.35–4.38). The observed Bi_2O_3 diffraction peak may be caused by the excess bismuth used for compensation of bismuth loss during the sintering process. The diffraction peak positions show almost no change with variation of donor species and/or their levels within the range studied. This can be explained by the low cosubstitution levels (≤ 4%) and the similar effective ionic radii of Ti^{4+} (0.605 Å) and donor cations (Nb^{5+}: 0.640, V^{5+}:0.540, Mo^{6+}:0.590, W^{6+}:0.600 Å).[169]

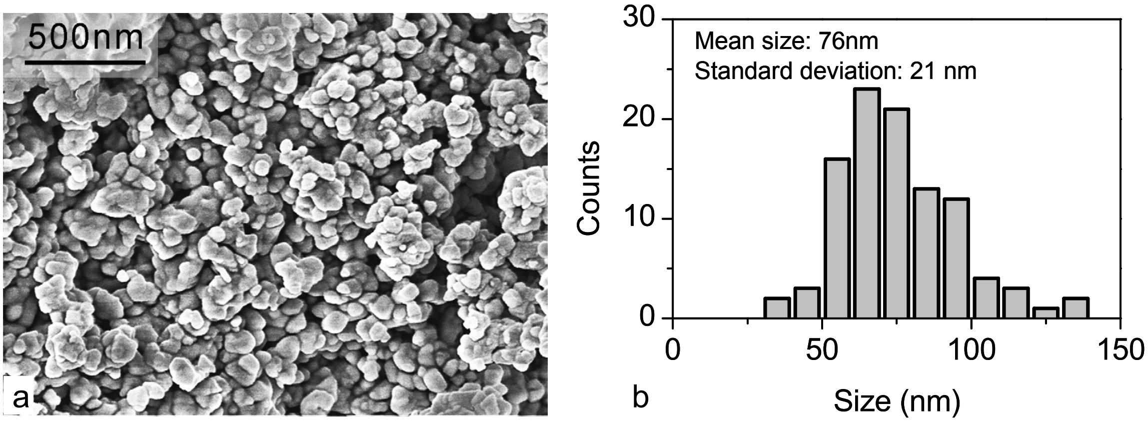

Fig 4.39 (a) Typical SEM image of synthesized powders, (b) particle size distribution obtained from (a).

Fig 4.39a gives a typical SEM image from the powders synthesized at 550 °C for 1 h. The particles are spherical in shape with a mean size of 76 nm and a standard deviation of 21 nm, obtained by measuring 100 particles in the SEM image (Fig 4.39b). The mean size is slightly larger than 57 nm for that of BPTV powder synthesized at 500 °C for 1 h (section 4.3),[179] which can be attributed to the increase of particle size with synthesis temperature.

4.4.2 Phase and Texture

The XRD patterns of the cosubstituted ceramics are shown in Fig 4.40–4.43. All the diffraction peaks can be indexed to the orthorhombic $Bi_4Ti_3O_{12}$ (ICSD #240210), despite some changes in intensity and position were observed. No impurity peak was observed in the XRD patterns for all of the $BLTM_x$ ceramics. The donor cosubstitution has few effects on the lattice of the $BLTM_x$ ceramics as indicated by the observed almost identical diffraction peak positions. However, change of relative intensity of some diffraction peaks, such as (060), (002), and (0$\underline{14}$0), etc., has been observed, which are correlated with both the donor species and their levels.

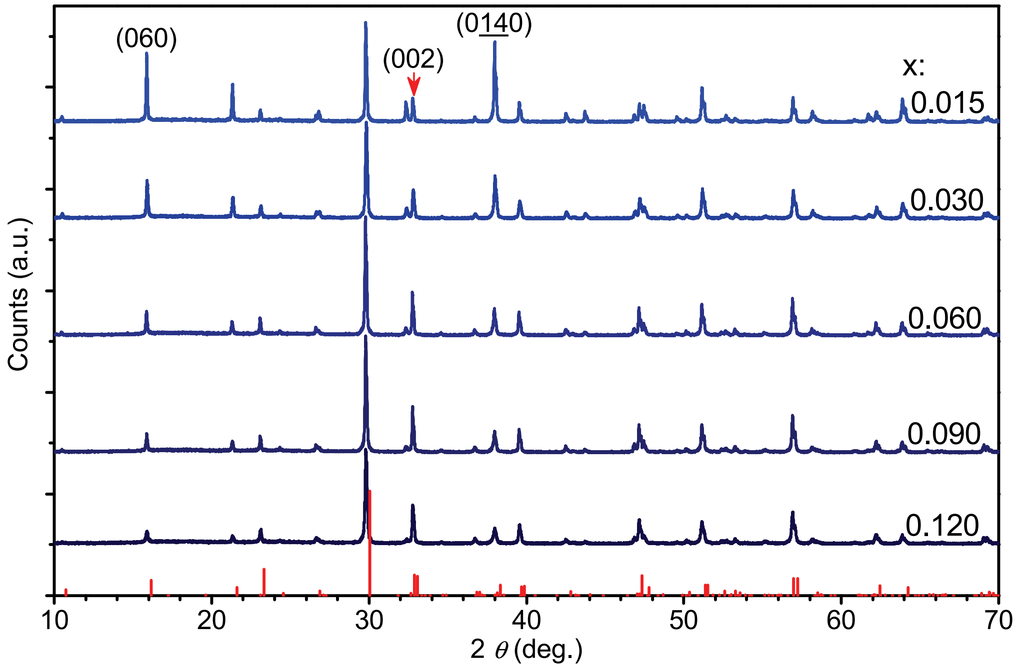

Fig 4.40 XRD patterns of the $Bi_{3.25}La_{0.75}Ti_{3-x}Nb_xO_{12}$ ceramics sintered at 900 °C for 4 h, bottom: position and intensity from ICSD #240210.

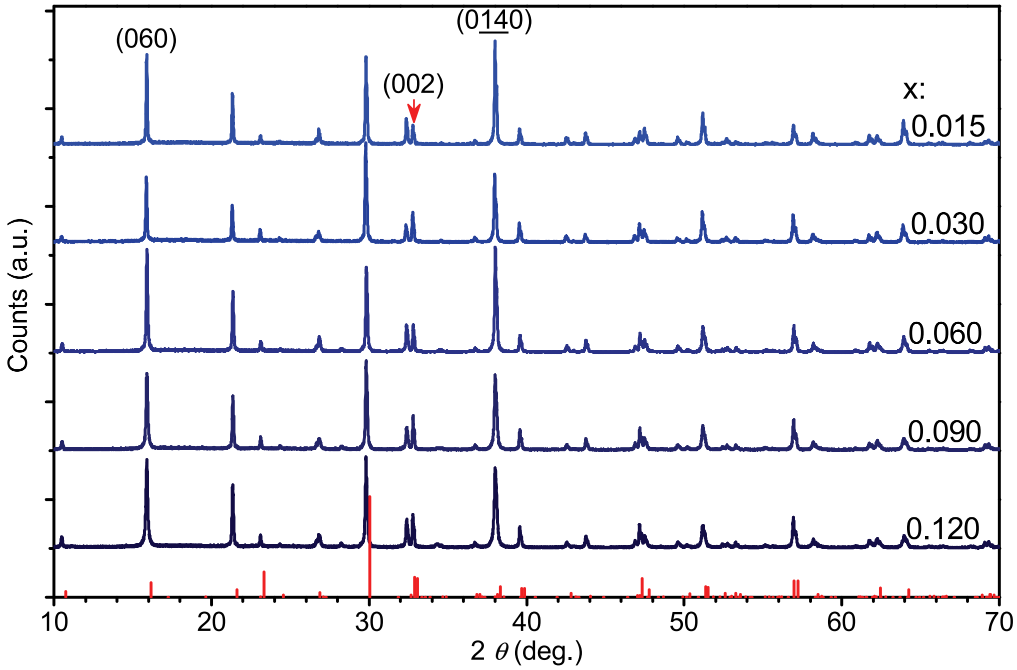

Fig 4.41 XRD patterns of the $Bi_{3.25}La_{0.75}Ti_{3-x}V_xO_{12}$ ceramics sintered at 900 °C for 4 h, bottom: position and intensity from ICSD #240210.

As seen in Fig 4.40, 4.42, and 4.43, the diffraction peak intensity of (060) and (0$\underline{14}$0) has an evident inverse relationship with x in the $BLTNb_x$, $BLTMo_x$, and $BLTW_x$ ceramics, respectively. On the contrary, a positive correlation was observed between x and the diffraction peak intensity of (002). These observations clearly demonstrate the donor cosubstitutions have profound influence on the texture of the cosubstituted ceramics. However, an obvious correlation between the change of diffraction peak intensity and x in $BLTV_x$ ceramics was not observed (Fig 4.41).

Texture effect is referred to as the grains in a polycrystalline material are aligned in a preferred orientation along certain lattice planes. Therefore, it is necessary to define a direction along which the alignment of the grains in the ceramics can be compared. The sample configuration of the ceramic platelets for XRD measurement is shown in Fig 4.44, in which the direction of preferred orientation was defined along the axis of the ceramic sample ($\boldsymbol{v}$ in Fig 4.44). For a textured ceramic platelet consisting of a larger number of grains with *c*-axis aligned in the preferred orientation direction, the relative intensity of (0 0 *l*) series diffraction peaks for the former will increase.

The texture effect in the $BLTM_x$ ceramics was quantitatively characterized by comparison of the diffraction peak intensity of (002) and (060) using a texture factor *f*:

$$f = \frac{I_{(002)}}{I_{(002)} + I_{(060)}} \qquad \textbf{Eq 4.8}$$

Here peak height was used as the peak intensity for convenience. Using integrated peak area for *I* only resulted in a slight change for *f*. A texture factor for a randomly oriented sample, denoted as f_0, equals 0.58 calculated from ICSD #240210 using above formula, which is represented by the dashed line in Fig 4.45. Therefore, the texture factor *f* of the ceramics with *c*-axis* aligned along $\boldsymbol{v}$ (Fig 4.44) will be larger than f_0 and it will be smaller than f_0 for that of the ceramics with *b*-axis orientated along $\boldsymbol{v}$, allowing the convenience of characterization of two texture effects by one factor. As seen in Fig 4.45, cosubstitution with M^{n+} causes an increase of the texture factor *f* in comparison to $Bi_{3.25}L_{0.75}Ti_3O_{12}$ (x = 0), which implies an increase of the preferred orientation with *c*-axis aligned along $\boldsymbol{v}$. The texture factor *f* of the $BLTNb_x$, $BLTMo_x$, and $BLTW_x$ ceramics has a relatively pronounced increase with x initially but has a more gradual increase for x above 0.05. The texture factor *f* reaches about the same value of f_0 at x = 0.05 for Nb^{5+}, Mo^{6+} cosubstitutions, and for x around 0.025 in the case of W^{6+}. Therefore, a change from the preferred orientation with *b*-axis to the *c*-axis aligned along $\boldsymbol{v}$ occurs at these x values when x increases from 0 to 0.1 or 0.12. However, the texture factor *f* of $BLTV_x$ ceramics varied from 0.2 to 0.3, which is far below f_0, indicating the preferred orientation with *b*-axis aligned along $\boldsymbol{v}$ for all the $BLTV_x$ ceramics studied ($0 \leq x \leq 0.12$). The texture factor *f* at the same x is roughly in the order of $BLTW_x > BLTNb_x$, $BLTMo_x$, $> BLTV_x$.

To confirm the texture of the ceramics, a BLT (x = 0) ceramic was ground and powder XRD pattern was recorded from the ground powder. As seen in Fig 4.46, the XRD pattern of the as-prepared ceramic platelet has much higher relative intensity of the (0 *k* 0) series diffraction peaks, indicating the presence of texture of the ceramic (Fig 4.46a). However, after grinding, the relative intensity of the (0 *k* 0) series diffraction peaks substantially decreased (Fig 4.46b). This suggests the observed change of relative intensity of diffraction peaks for the $BLTM_x$ ceramics mainly resulted from the texture effect and not from the change of crystal structure due to the cosubstitution. It was further supported by the almost identical factor *f* calculated from the simulated XRD patterns of the crystal structures by partial replacement of Bi with La at the perovskite layer, and replacement of Ti with Nb at both Ti1 and Ti2 site. The overall shift of diffraction peak positions of the ceramic sample in

---

* Because (002) and (200) diffraction peaks overlapped, the preferred orientation could be also along *a*-axis.

comparison to those of the ground sample (Fig 4.46) might result from the sample displacement of the ceramic.

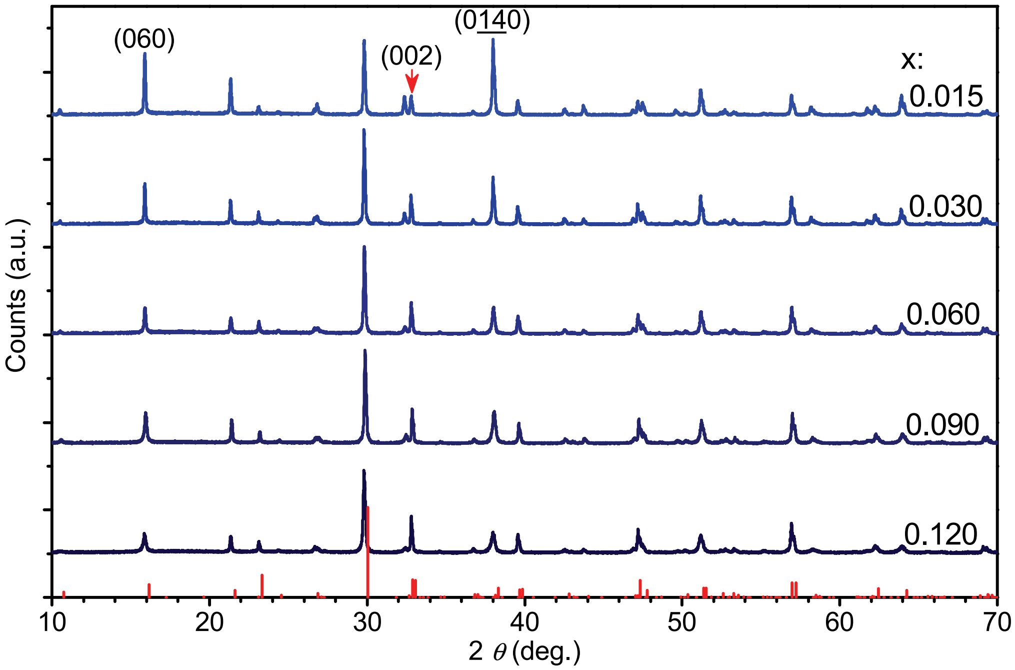

Fig 4.42 XRD patterns of the $Bi_{3.25}La_{0.75}Ti_{3-x}Mo_xO_{12}$ ceramics sintered at 900 °C for 4 h, bottom: position and intensity from ICSD #240210.

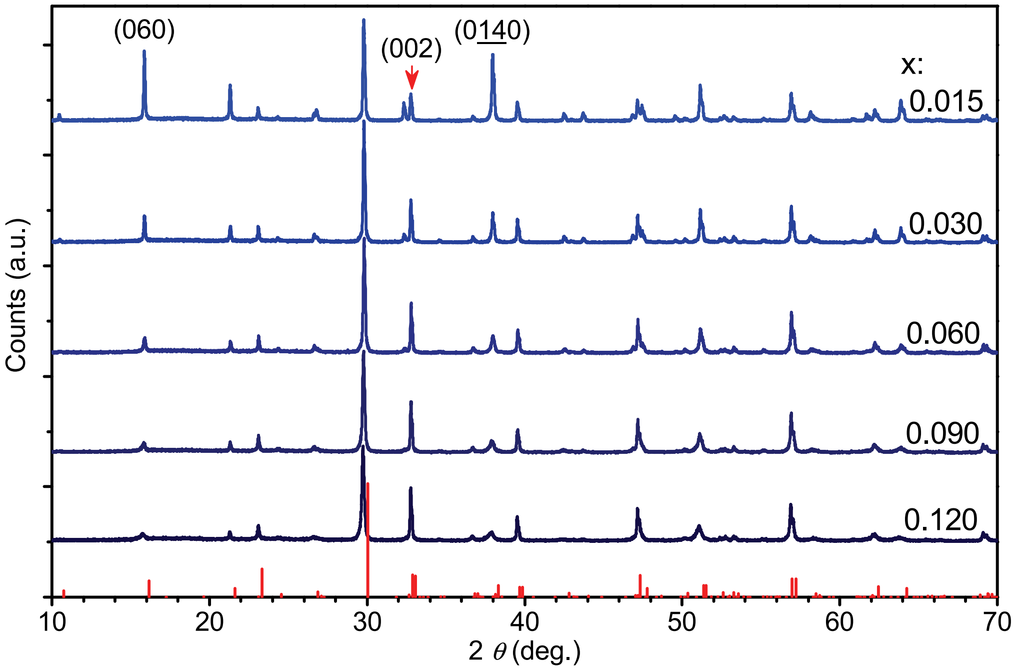

Fig 4.43 XRD patterns of the $Bi_{3.25}La_{0.75}Ti_{3-x}W_xO_{12}$ ceramics sintered at 900 °C for 4 h, bottom: position and intensity from ICSD #240210.

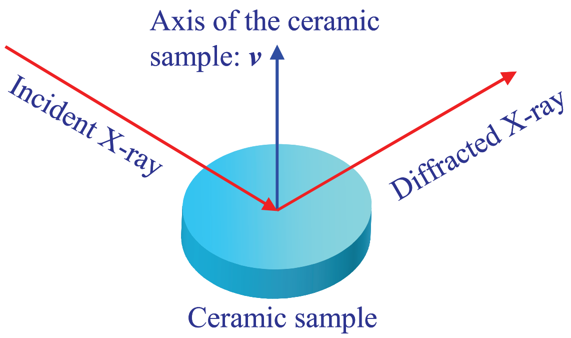

Fig 4.44 Sample configuration of the ceramic platelets for XRD measurement.

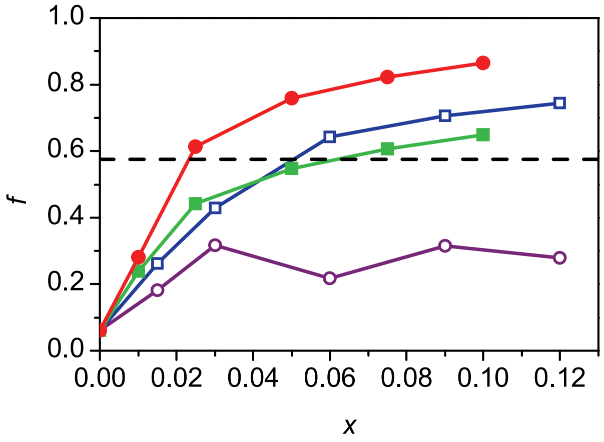

Fig 4.45 The orientation factor, $f = I_{(002)} / (I_{(002)}+I_{(060)})$, as function of x in BLTM$_x$ ceramics, □ M = Nb, ○ M = V, ■ M = Mo, ● M = W, dashed line: ICSD #240210.

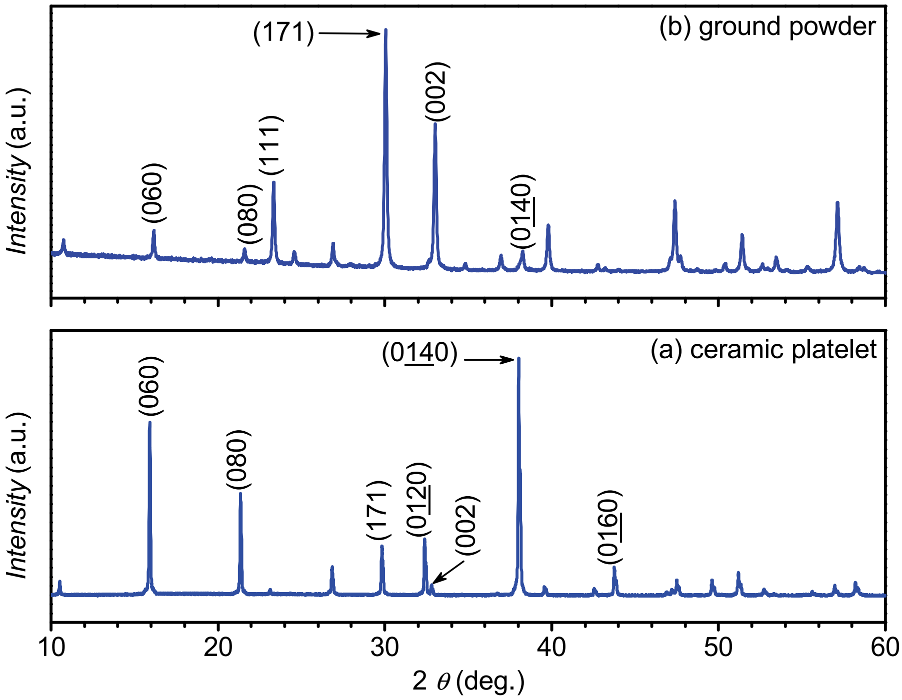

Fig 4.46 XRD patterns of $Bi_{3.25}La_{0.75}Ti_3O_{12}$ ceramics, (a) as-prepared and (b) ground.

The increase of preferred orientation with *c*-axis aligned along ***v*** with donor substitution is in agreement with Chang et al's observations in $Bi_{3.5}Nd_{0.5}Ti_{2.97}Nb_xO_{12}$ thin films.[180] The decrease of preferred orientation with *b*-axis aligned along ***v*** at low substitution level is consistent with Hardy and Ohki et al's results in $Bi_{3.5}La_{0.5}Ti_{2.97}M_{0.03}O_{12}$ (M = Nb, V, Mo, and W) and $Bi_{3.25}La_{0.75}Ti_{2.985}Mo_{0.015}O_{12}$ thin films respectively.[34, 181] However, in Hardy et al's report, both increase (M = Nb, Mo) and decrease (M = W, V) of preferred orientation with *b*-axis aligned along ***v*** was observed in the $Bi_{3.5}La_{0.8}Ti_{2.97}M_{0.03}O_{12}$ thin films annealed at 650.[181]

Another contrary observation of an increase of preferred orientation with *b*-axis aligned along ***v*** with donor cosubstitutions in $Bi_{3.5}Pr_{0.5}Ti_{3-x}M_xO_{12}$ (M = Mo, and W) thin films on $Pt/Ta/SiO_2/Si$ substrates was reported by Lin et al.[32] The confliction of these reports with this work is tentatively attributed to the possible interferences from substrates. The interferences from substrates include the different boundary conditions between film/substrate and film/air, and stresses resulting from the mismatch of lattice constant and/or thermal expansion coefficient between the films and the substrate, etc, which could be possible to alter the preferred orientation. The different level and kind of lanthanoid substitutions, preparation temperature and time might also be the possible reasons for the inconsistent observations. Since all the ceramics studied in this work are free standing, the interference from substrates can be excluded. Therefore, the change of texture observed in this work could be attributed to the pure donor cosubstitution effects.

4.4.3 Morphology and Microstructure of Ceramics

Fig 4.47–4.50 shows the typical SEM images of the cosubstituted ceramics, in which the inset gives the corresponding higher magnification image. All the cosubstituted ceramics show dense microstructures, which mainly consist of platelet-like grains despite variation of grain size with donor species and their levels have been observed. A major change in the microstructure of the $BLTM_x$ ceramics is the decrease of the platelet-like grain size, both in length and thickness, with the increase of x.

As seen in Fig 4.47a, $BLTNb_{0.015}$ ceramics consist of platelet-like grains with a mean size of about 2.8 μm in length and 200 nm in thickness. However, the mean size of the platelet-like grains in the $BLTNb_{0.12}$ ceramics decrease to about 320 nm in length and 120 nm in thickness (Fig 4.47e), which is much more isotropic in shape. In comparison to the $BLTNb_x$ ceramics, the $BLTV_x$ ceramics consist of larger platelet-like grains and show less decrease in size with increase of x (Fig 4.48). The mean size of the platelet-like grains in the $BLTV_{0.015}$ ceramics is about 3.0 μm in length and 325 nm in thickness (Fig 4.48a), and that of $BLTV_{0.12}$ is about 1.7 μm in length and 210 nm in thickness (Fig 4.48e). The $BLTMo_x$ and $BLTW_x$ ceramics show similar microstructure evolution to that of $BLTNb_x$ ceramics (Fig 4.49 and 4.50).

The length, thickness, and the ratio of length to thickness of the platelet-like grains, obtained from the SEM images, as functions of x are shown in Fig 4.51. As seen in Fig 4.51a, all the cosubstituted ceramics decrease in the thickness of the plate-like grains with x. The same trend is observed for the length and the ratio of length to thickness of the platelet-like grains in $BLTNb_x$, $BLTMo_x$, and $BLTW_x$ ceramics (Fig 4.51b and 4.51c). However, the length and the ratio of length to thickness of the platelet-like grains in $BLTV_x$ ceramics initially increase with x, but decrease after x reaches a threshold (Fig 4.51b and 4.51c).

The decrease of grain size with donor cosubstitution is consistent with previous reports on the inhibition of the grain growth in Ta^{5+},[182] Nb^{5+},[180] Mo^{6+},[32]and W^{6+}[32, 181] substituted

$Bi_4Ti_3O_{12}$, W^{6+} substituted Bi_3TiNbO_9[183], and La^{3+} substituted $BaTiO_3$[184] and $PbSn_{0.5}Sb_{0.5}O_3$- $PbTiO_3$- $PbZrO_3$[185] ceramics or thin films. However, the evident decrease of grain size in the $BLTNb_x$ ceramics is not in agreement with a report that Nb^{5+} cosubstitution led to enhanced grain growth in BLTNb thin films.[181] This discrepancy may be attributed to the differences in form, preparation temperature and time, etc. The decrease of grain size with donor cosubstitution cannot be explained by the change of surface free energy alone, since both the length and thickness decreased. In fact, growth step terraces are frequently observed in all the cosubstituted ceramics (Fig 4.52a), suggesting the platelet-like grains are formed by epitaxial growth on the (0 *k* 0) facets and supporting few changes of surface free energy with donor cosubstitution.

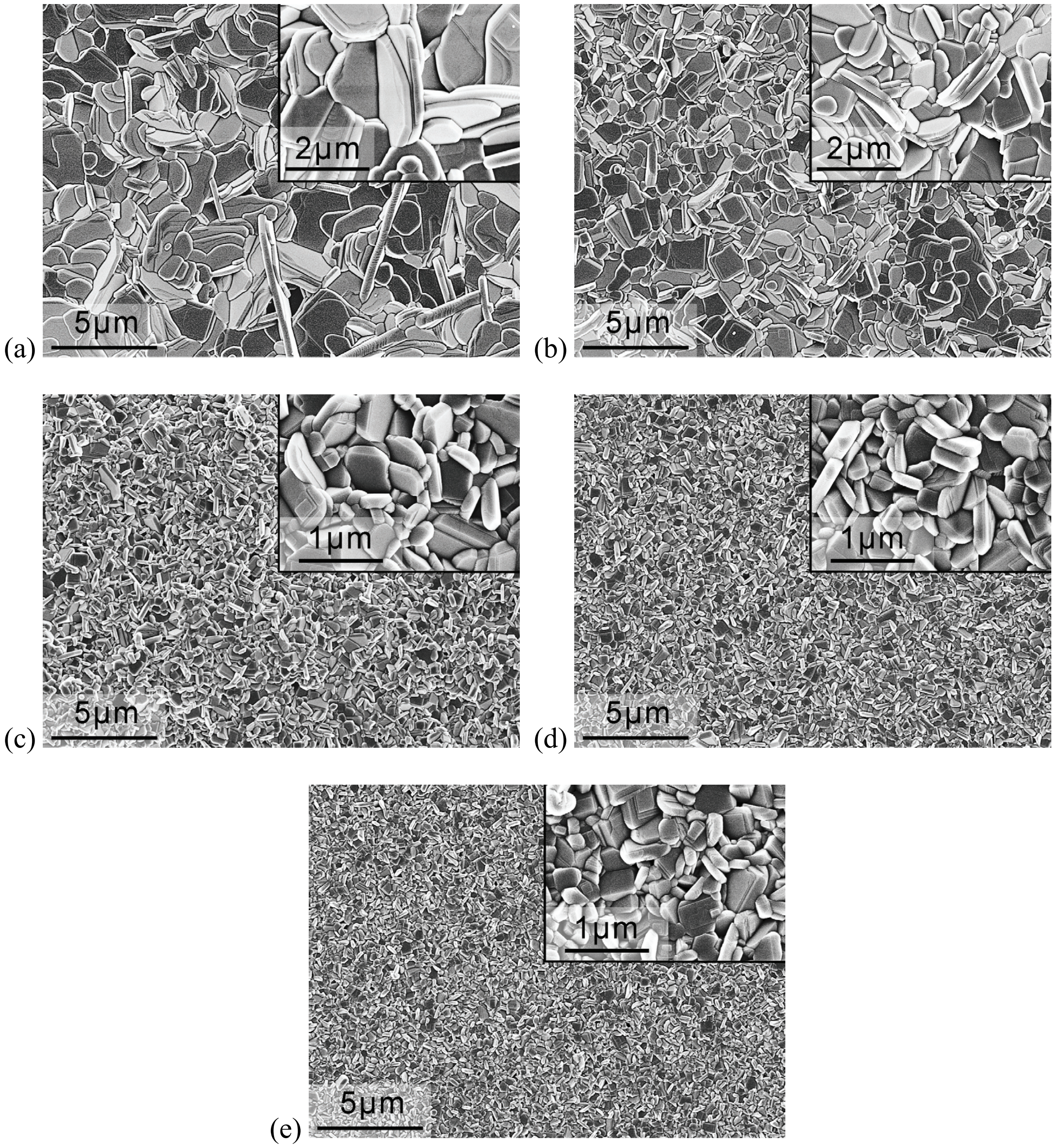

Fig 4.47 SEM images of $BLTNb_x$ ceramics, (a) x = 0.015, (b) x = 0.030, (c) x = 0.060, (d) x = 0.090, and (e) x = 0.120.

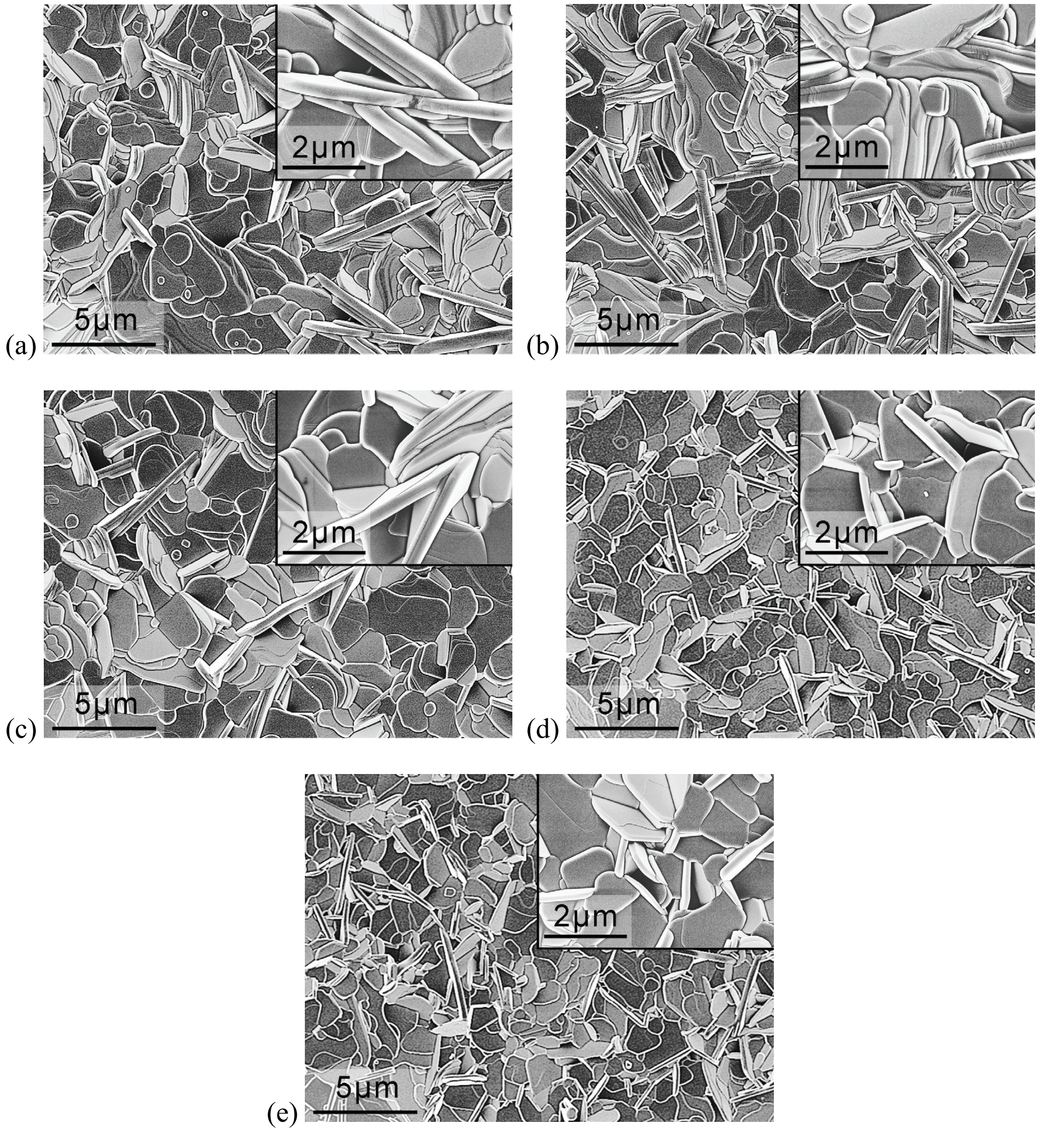

Fig 4.48 SEM images of BLTV$_x$ ceramics, (a) x = 0.015, (b) x = 0.030, (c) x = 0.060, (d) x = 0.090, and (e) x = 0.120.

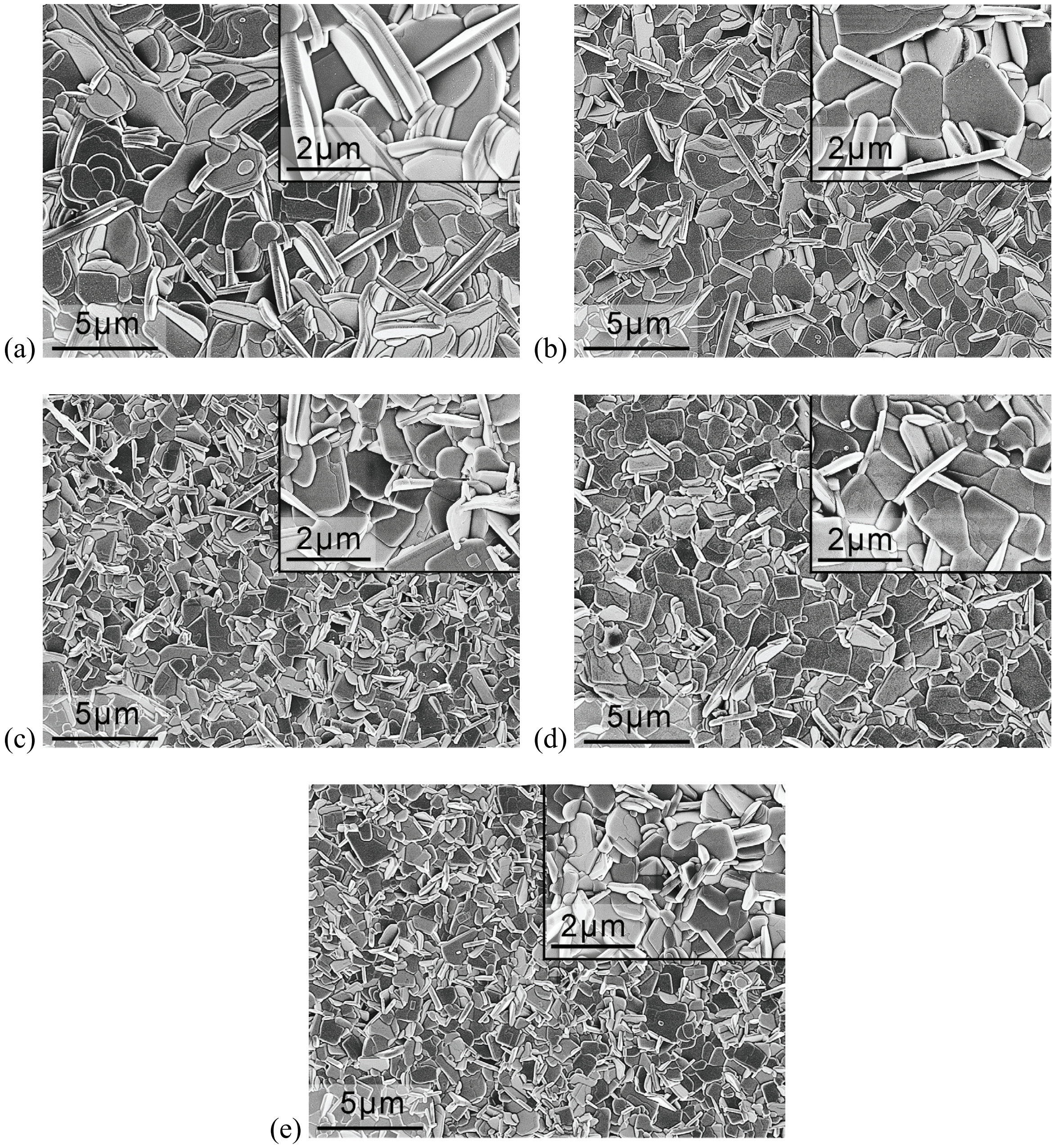

Fig 4.49 SEM images of BLTMo$_x$ ceramics, (a) x = 0.010, (b) x = 0.025, (c) x = 0.050, (d) x = 0.075, and (e) x = 0.100.

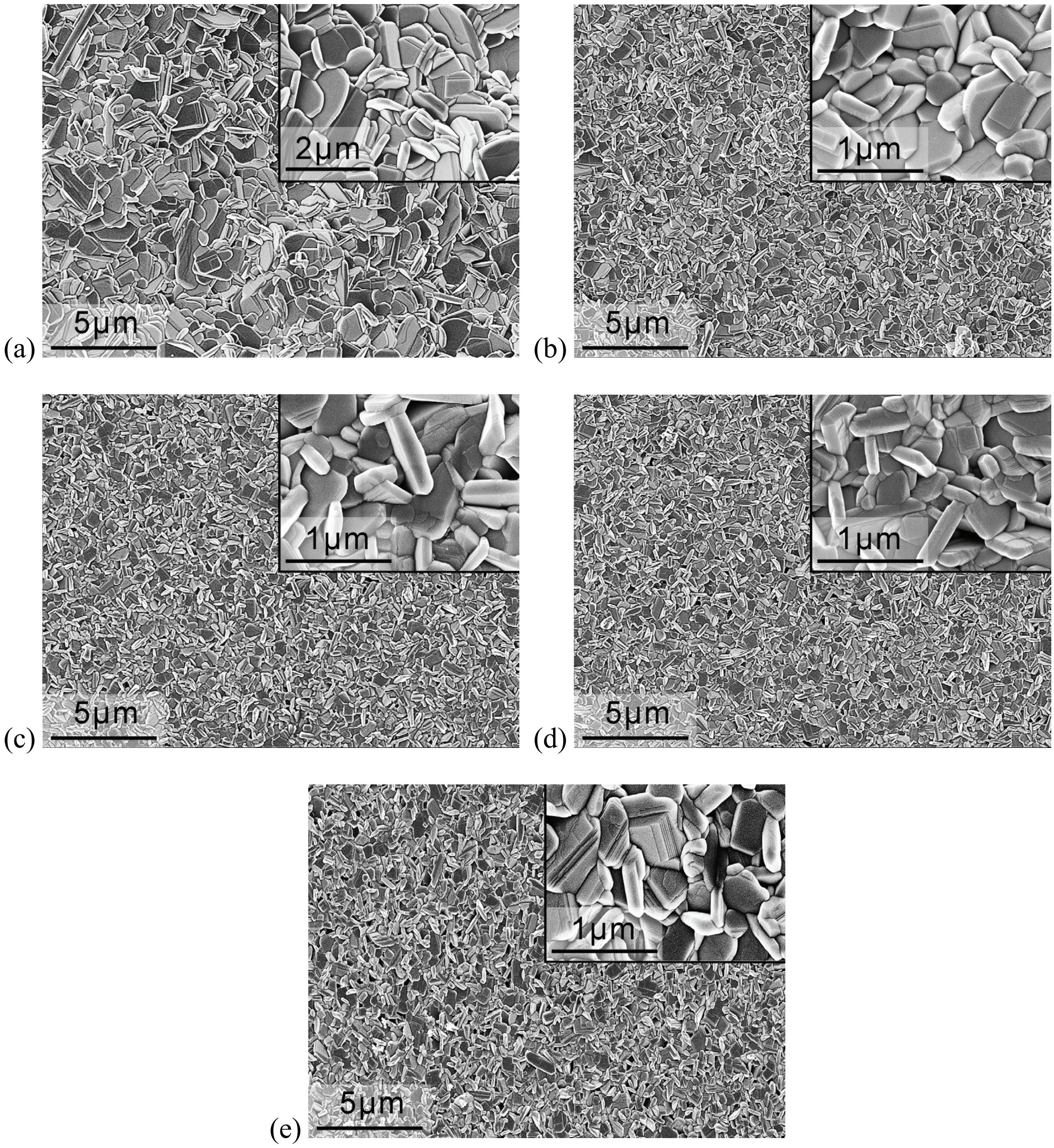

Fig 4.50 SEM images of BLTW$_x$ ceramics, (a) x = 0.010, (b) x = 0.025, (c) x = 0.050, (d) x = 0.075, and (e) x = 0.100.

By comparison of the grain size of donor (La^{3+}) substituted $BaTiO_3$ sintered in air and in high oxygen pressure atmospheres, Shimanskij et al. have suggested that the inhibition of grain growth in donor substituted $BaTiO_3$ is caused by the decrease of oxygen vacancies.[184] Because the decrease of oxygen vacancies slows down the transport of oxygen ions, thus suppresses the diffusion process in the grains and/or grain boundaries and hinders the grain growth. Shimanskij et al's explanation is further supported by the evidence of the decrease of the grain size with La^{3+} substitution in the $PbSn_{0.5}Sb_{0.5}O_3$- $PbTiO_3$- $PbZrO_3$ system observed by Hwang et al.[185] The observed inhibition of grain growth in the BLTM$_x$ ceramics in this work may be explained in the similar way to that of Shimanskij et al's report.

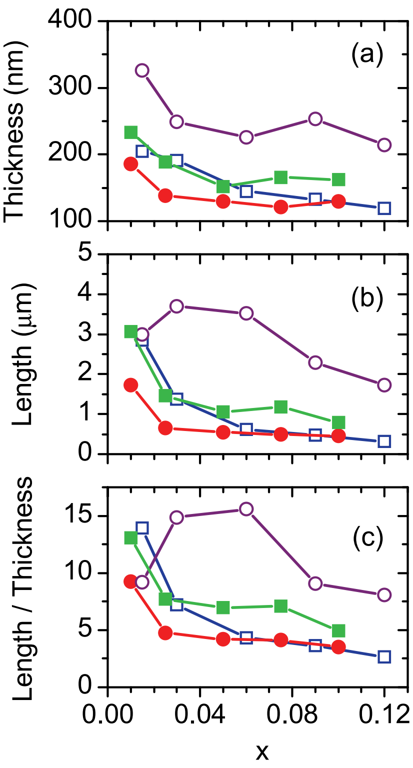

Fig 4.51 Thickness (a), length (b), and the ratio of length to thickness (c) of the platelet-like grains as function of x measured from SEM images of BLTM$_x$ ceramics, □ M = Nb, ○ M = V, ■ M = Mo, ● M = W.

However, the decrease of oxygen vacancies can not explain why the BLTNb$_x$ and BLTV$_x$ ceramics have such huge differences in their microstructure (Fig 4.47 and 4.48) because the Nb^{5+} and V^{5+} have same charge, and so do the BLTMo$_x$ and BLTW$_x$ ceramics (Fig 4.49 and 4.50). One possible reason for the huge differences between the BLTNb$_x$ and BLTV$_x$ ceramics in their microstructure (Fig 4.47 and 4.48) could be attributed to the possible presence of low-valent vanadium ions (V^{4+}) in the BLTV$_x$ ceramics, which have been observed in $SrBi_2(V_{0.1}Nb_{0.9})_2O_9$ ceramics[186] sintered in air. Since V^{4+} has the same valence as Ti^{4+}, it will loss the ability to compensate oxygen vacancies, thereby causing V^{5+} cosubstitution less effective in the decrease of grain size than that of Nb^{5+}. However, this cannot explain why the BLTMo$_x$ and BLTW$_x$ ceramics have different grain size (Fig 4.49 and 4.50). It is worth noting that the grain size is in the order of BLTV$_x$ > BLTNb$_x$, and BLTMo$_x$ > BLTW$_x$, which have a reverse relationship with the effective ionic radii of the donor cations (V^{5+} (0.540) < Nb^{5+} (0.64), and Mo^{6+}(0.590) < W^{6+} (0.60), in Å with a coordination number of 6[169]). This demonstrates that cosubstitution using the smaller donor results in larger grain size. A smaller donor is reasonably expected to have high mobility than a larger one, thereby resulting in larger grains. This also could be the reason for the initial increase of grain size (length) with the V^{5+} cosubstitution. Because the size of V^{5+} (0.540 Å) is smaller than that of Ti^{4+}(0.605 Å),[169] the V^{5+} cosubstitution could promote the grain growth and the oxygen compensation effect might be less important at low substitution level. As x increases above the threshold, the decrease of the mobility of oxygen ions becomes the profound effect, thereby resulting in the decrease of the grain size. Moreover, the grain size also has a reverse relationship with the melting point of the donor oxides (V_2O_5: 690 < Nb_2O_5: 1520, and MoO_3: 795 < WO_3: 1473, in °C). However, no increase of grain size was observed in the BLTV$_{0.12}$ and BLTMo$_{1.0}$ ceramics in comparison to the BLT ceramic.

Furthermore, all the melting points of the donor oxides are lower than that of TiO_2 (1840 °C), implying the lower melting point of the donor cation oxides does not have significant effect on the grain size. Therefore, the possible presence of V^{4+} ions and the subtle differences in the donor cation size might be the reason for the observed considerable variations in the microstructure of the $BLTM_x$ ceramics cosubstituted with the same valence donors at the same cosubstitution levels.

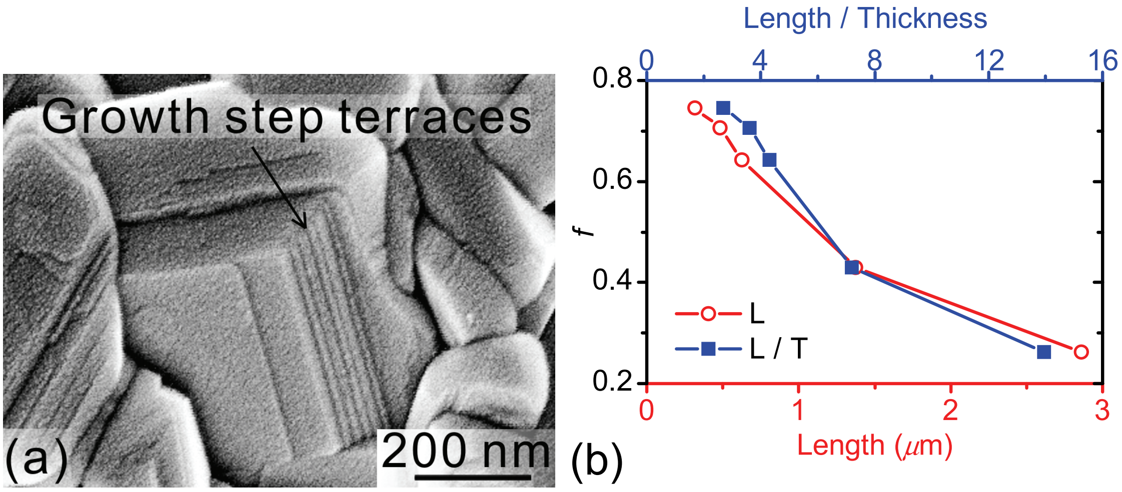

Fig 4.52 (a) The growth step terraces observed in $BLTW_{0.1}$, (b) the orientation factor, $f = I_{(002)} / (I_{(002)}+I_{(060)})$, as a function of length (L) and the ratio of length to thickness (L / T)of the platelet-like grains in $BLTNb_x$ ceramics.

Another point should be stressed, that is an inverse relationship between the texture factor *f* and the platelet length, or the ratio of length to thickness is observed in BLTNb, BLTMo, and BLTW ceramics (represented by BLTNb, Fig 4.52b). This implies the increase of the texture factor *f* with the donor cosubstitution is probably related to the decrease of grain size. The latter could be caused by the slow transport of oxygen ions[184] because of the compensation of oxygen vacancies by the donor cosubstitution.

4.4.4 Ferroelectric Properties

The *P-E* hysteresis loops were measured for all the prepared $BLTM_x$ ceramics. To subtract the contribution of leakage current to the *P-E* hysteresis loops, a dynamic leakage current compensation (DLCC) method developed by Meyer et al.[187] was used to obtain the leakage current compensated *P-E* hysteresis loops. Using the different frequency dependencies of the ferroelectric switching current, dielectric displacement current and ohmic leakage current, the DLCC method provides a convenient way to subtract the leakage current contribution to a *P-E* hysteresis loop without performing a static leakage current measurement.

In the DLCC method,[187] it was supposed that ferroelectric domain switching current (i_{FE}) and parasitic dielectric displacement current (i_P) have a linear relationship with the frequency of the drive electric field, however, the leakage current (i_R) obeys Ohm's law and is independent on the frequency of the drive electric field (Fig 4.53). Therefore, the electric current ($i(\omega)$)for uncompensated hysteresis measurement can be written in the following form:

$$i(\omega) = \omega \cdot i_{\mathrm{FE}}(0) + \omega \cdot i_P(0) + i_R \qquad \textbf{Eq 4.9}$$

Therefore, the leakage current (i_R) can be eliminated by two hysteresis measurements at different frequencies:

$$\Delta i = i(\omega_2) - i(\omega_1) = (\omega_2 - \omega_1) \cdot (i_{\mathrm{FE}}(0) + i_P(0)) \qquad \textbf{Eq 4.10}$$

If $\omega_2 = 2\omega_1$, the compensated electric current (i_{comp}) at frequency of ω_1 can be obtained:

$$\Delta i(\omega_1) = \omega_1 \cdot (i_{\mathrm{FE}}(0) + i_P(0)) = i_{\mathrm{comp}}(\omega_1) \qquad \textbf{Eq 4.11}$$

The compensated hysteresis loop at frequency ω_1 can be obtained by integration of the compensated electric current ($i_{\mathrm{comp}}(\omega_1)$) with time and the plot vs. the electric field.

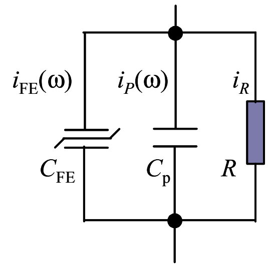

Fig 4.53 Equivalent circuit for a ferroelectric capacitor used in the DLCC method.[187]

The upper parts of Fig 4.54a–d (blue) show the uncompensated *P-E* hysteresis loops for $BLTM_x$ at the optimum x values, in which all the plots show well-saturated hysteresis loops with sharp ends at high electric field. The dynamic leakage current compensated 10 Hz *P-E* hysteresis loops are shown in the upper parts of Fig 4.54a–d (red), which were obtained from *P-E* hysteresis loops at 10, and 20 Hz. The lower parts of Fig 4.54a–d give the corresponding *J-E* curves for the hysteresis loops obtained at 10 Hz (uncompensated, blue), 20 Hz (uncompensated, green), and 10 Hz(compensated, red). The leakage current compensated (red) and uncompensated (blue) *P–E* hysteresis loops are almost identical in ± P_r and maximum polarization ± $P_{\max}$, implying no considerable leakage current contributions to the *P-E* hysteresis loops. The main difference between the compensated and uncompensated *P-E* hysteresis loops is an increase of the value of ± E_c, and so is that between the compensated and uncompensated *J–E* curves. This might be a result of neglecting the increase of E_c with switching frequency in the DLCC method.[187]

The low leakage current was further verified by the static leakage current measurements. Fig 4.55a and 4.55b give the logarithmic and linear scale *J–E* curves of the $BLTW_{0.025}$ ceramic, showing a slight asymmetric leakage current density. A linear relationship was observed between *J* and *E* (Fig 4.55b). The leakage current density is below 1.0 μA/cm^2 within a range of ± 200 kV/cm, which is consistent with the DLCC result (Fig 4.54d).

Fig 4.56a and 4.56b show the $2E_c$ and $2P_r$ against x in the $BLTM_x$ ceramics measured at 10 Hz with an applied electric field of 250 kV/cm. Compared to the BLT ceramics, a slight increase of $2E_c$ is observed in the cosubstituted ceramics (Fig 4.56a). The $2P_r$ values of the $BLTM_x$ ceramics have a pronounced increase with x and reach a maximum of 30.6, 31.0 and 30.8, 30.4 μC/cm^2, at x = 0.025 and 0.030 for the $BLTMo_x$, $BLTW_x$ and $BLTNb_x$, $BLTV_x$ ceramics respectively (Fig 4.56b). The $2P_r$ values are less dependent on the donor species at the optimum x. After reaching the maximum, the $2P_r$ values show a gradual decrease for $BLTMo_x$, and $BLTW_x$ ceramics, and a steep decrease for the $BLTV_x$ ceramics. However, no profound decrease of $2P_r$ is observed in the $BLTNb_x$ ceramics.

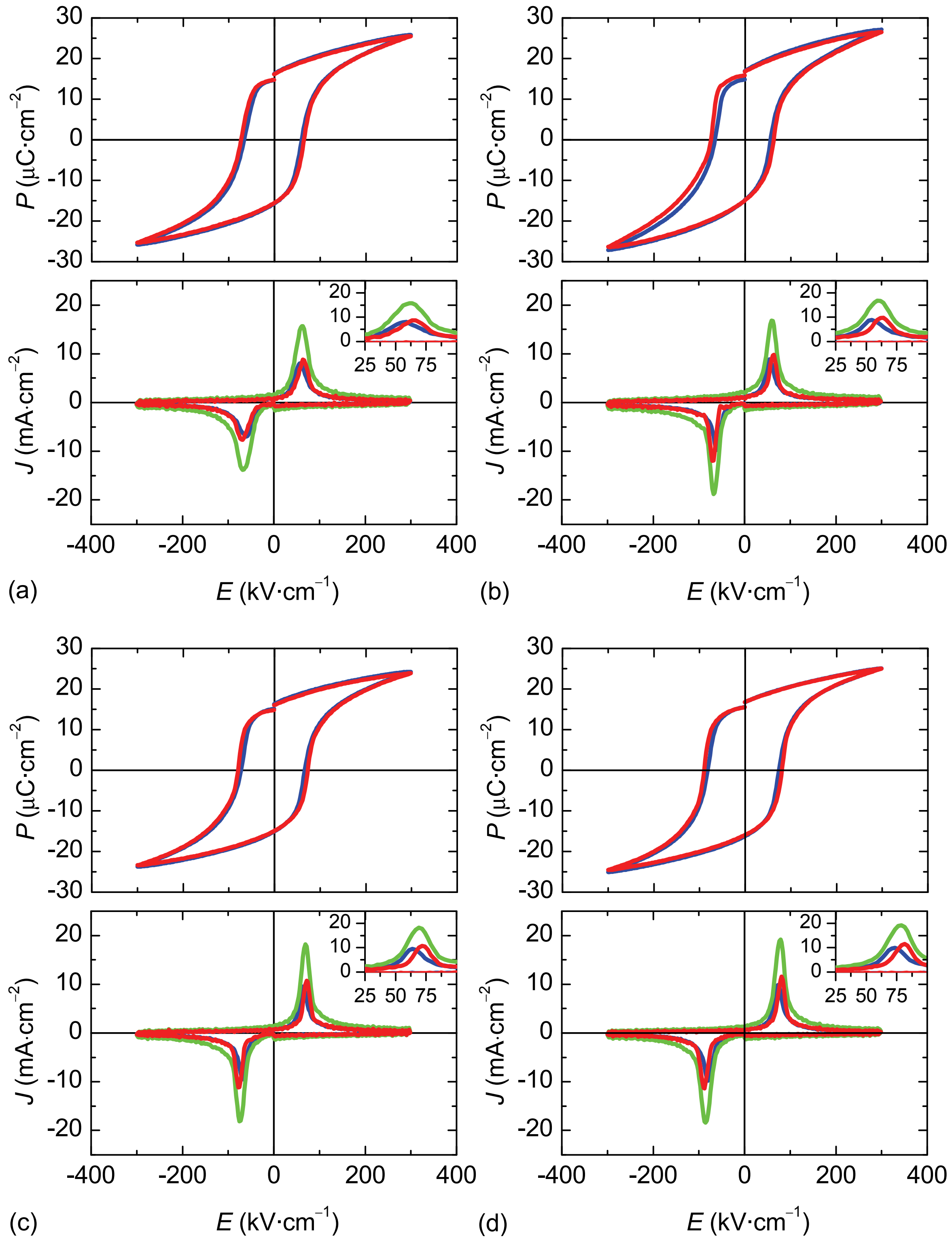

Fig 4.54 ***P-E*** **hysteresis loops and** ***J-E*** **curves of (a) BLTNb$_{0.03}$, (b) BLTV$_{0.03}$, (c) BLTMo$_{0.025}$, and (d) BLTW$_{0.025}$, upper parts: uncompensated (red) and compensated (blue)** ***P-E*** **hysteresis loops; lower parts:** ***J-E*** **curves at 10 Hz (uncompensated, blue; compensated, red), and 20 Hz (uncompensated, green), insets: details of the peaks in the positive electric field observed in the corresponding** ***J-E*** **curves.**

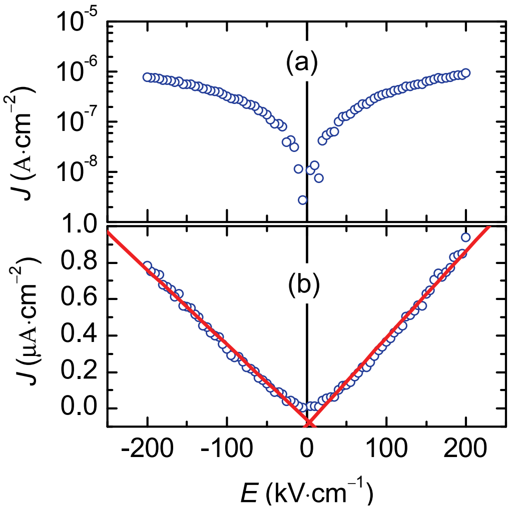

Fig 4.55 *J–E* plots of the $BLTW_{0.025}$ ceramic: (a) logarithmic scale, (b) linear scale (circles, experiment; solid line, line fit).

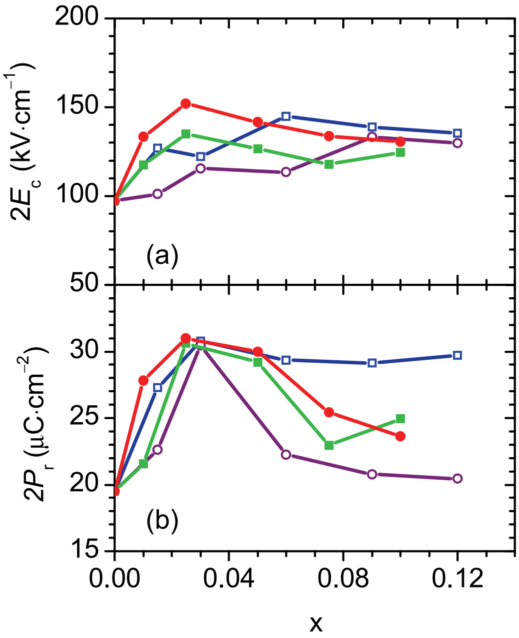

Fig 4.56 $2E_c$ (a) and $2P_r$ (b) as function of x for $BLTM_x$ ceramics, □ M = Nb, ○ M = V, ■ M = Mo, ● M = W.

A comparison between the $BLTM_x$ ceramics prepared by the citrate-gel method and those prepared by the solid-state reaction is listed in Table 4.7. It clearly demonstrates the advantage of the citrate-gel method as compared to the solid-state reaction method in terms of the P_r. Nd^{3+} substitution has been reported to be more effective than La^{3+} in improving the P_r.[35, 167] However, the $BLTM_x$ ceramics obtained from citrate-gel method have larger P_r than that of V^{5+} cosubstituted $(Bi,Nd)_4Ti_3O_{12}$[38, 39] and $Bi_{3.25}La_{0.75}Ti_3O_{12}$[40] ceramics prepared by solid-state reaction. The maximum P_r of $BLTM_x$, about 16 μC/cm^2 at 300 kV/cm, is slight smaller than that of BPTV ceramics (17 μC/cm^2).[179] This could be explained by larger structural distortion in Pr^{3+} substitution than that of La^{3+} substitution,[167] because the smaller effective radii of Pr^{3+}(1.126 Å) than that of La^{3+} (1.160) for a coordination number of 8.[169]

Table 4.7 Comparison of the properties for the cosubstituted $Bi_4Ti_3O_{12}$ ceramics prepared from solid-state reaction and citrate-gel method.

Composition	P_r [a]	E_c [b]	E_{max} [b]	Growth method	Growth Condition
$Bi_{3.15}Nd_{0.85}Ti_{2.97}V_{0.03}O_{12}$	13	54	~115	Solid-state[38]	900–1100 °C, 2 h
$Bi_{3.64}Nd_{0.36}Ti_{2.98}V_{0.02}O_{12}$	15.5	54	/	Solid-state[39]	950–1150 °C, 2 h
$Bi_{3.25}La_{0.75}Ti_{2.97}V_{0.03}O_{12}$	11	42	80	Solid-state[40]	900–1150 °C, 2 h
$Bi_{3.25}La_{0.75}Ti_3O_{12}$	7.5	56	80	Solid-state[40]	900–1150 °C, 2 h
$Bi_{3.25}Pr_{0.75}Ti_{2.97}V_{0.03}O_{12}$	17	74	300	Citrate-gel[c]	900 °C, 4 h
$Bi_{3.25}Pr_{0.75}Ti_3O_{12}$	12	58	250	Citrate-gel[c]	900 °C, 4 h
$Bi_{3.25}La_{075}Ti_3O_{12}$	9.7	49	200	Citrate-gel[c]	900 °C, 4 h
$Bi_{3.25}La_{075}Ti_{2.97}Nb_{0.03}O_{12}$	15.9	63	300	Citrate-gel[c]	900 °C, 4 h
$Bi_{3.25}La_{0.75}Ti_{2.97}V_{0.03}O_{12}$	15.9	62	300	Citrate-gel[c]	900 °C, 4 h
$Bi_{3.25}La_{0.75}Ti_{2.97}Mo_{0.025}O_{12}$	15.3	70	300	Citrate-gel[c]	900 °C, 4 h
$Bi_{3.25}La_{0.75}Ti_{2.97}W_{0.025}O_{12}$	16.3	78	300	Citrate-gel[c]	900 °C, 4 h

a in μC/cm², *b* in kV/cm, *c* this dissertation.

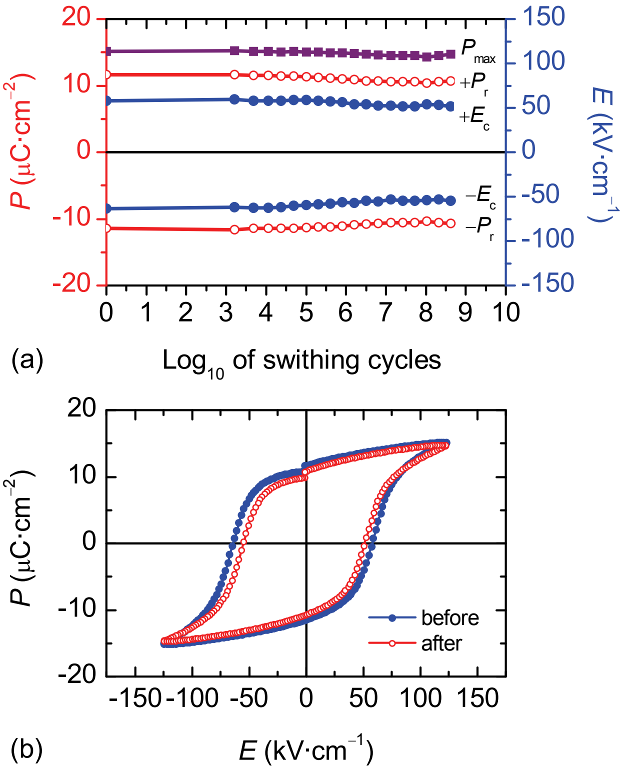

Fig 4.57 Fatigue properties of $BLTW_{0.025}$ ceramic.

A $BLTW_{0.025}$ ceramic was used for polarization fatigue measurements because of its slight larger P_r than that of the other $BLTM_x$ ceramics. As seen in Fig 4.57a, both ± P_r, ± E_c, and P_{max} show a slight decrease with the accumulative switching cycles. The decrease in ± P_r after 4.19×10^8 switching cycles is less than 7 %. However, only about 3 % decrease was observed in P_{max}. Supposing the polarization fatigue process is caused by pinning of domains, and the pinned domains cannot be reoriented up to E_{max}, there should be always equal amount of absolute decrease in P_r and P_{max} after fatigue measurement. However, the absolute decrease in P_{max} is 0.43 μC·cm^{-2}, about half of the decrease in P_r (0.80 μC·cm^{-2}). This implies that the pinned domains formed during the repetitive switching may be reoriented to a certain extent at high electric field, and hence still have contribution to the P_{max} in a P-E measurement. However, these pinned domains restore to their original pinning state as the electric field steps down, therefore, have no contributions to the P_r. Fig 4.57b gives the hysteresis loops measured before and after the fatigue test, showing a slight decrease of $\pm P_r$, $\pm E_c$, and P_{max} after the fatigue test.

4.4.5 Effect of the Donor Cosubstitution

As discussed above, the donor cosubstitution has a great influence on the preferred grain orientation (texture), microstructure (grain size and shape), and ferroelectric properties (especially P_r). Firstly, the cosubstituted donors compensate charged defects (such as Na^+, Fe^{3+}, etc., which are abundant in nature[63]), decrease the concentration of oxygen vacancies, and thus suppress the domain-wall pinning and decrease the electric leakage current (effect i).[23, 24] Secondly, because of the decrease in the concentration of oxygen vacancies, the donor cosubstitution probably results in slow transport of oxygen ions,[184] hence inhibiting the grain growth. The inhibition of grain growth may result in two contrary effects: It causes higher *c*-axis orientation along ***v*** (Fig 4.44, effect ii) and smaller grains (effect iii). Because the spontaneous polarization of a $Bi_4Ti_3O_{12}$ crystal is in the *a*-*c* lattice plane (*Aea*2, the standard setting of S.G. 41), more grains with *c*-axis oriented along ***v*** will give high remanent polarization with the applied electric field (Fig 4.58). Cosubstitution also results in higher volume of grain boundaries because of the smaller grains, in which the remanent polarization may be suppressed by compensated charge and large mechanical stresses resulting from grain boundaries,[43] thereby preventing domain reversal with external fields,[43] and causing degradation of ferroelectric performance in terms of polarization, electric leakage current, dielectric strength, etc.[188]

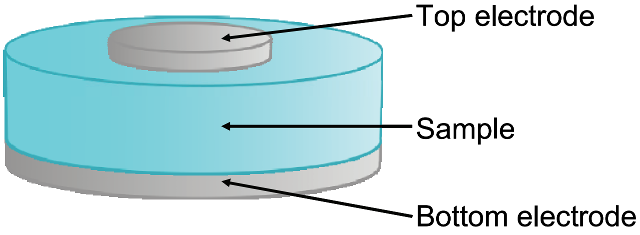

Fig 4.58 Sample configuration for the ferroelectric *P–E* hysteresis measurement.

Effects (i) and (ii) have positive correlations with P_r, and there is a negative correlation between P_r and the effect (iii). The evolution of $2P_r$ with donor cosubstitution levels (Fig 4.56b), low leakage current (Fig 4.54 and 4.55) and low polarization fatigue (Fig 4.57) can be explained with the consideration of these positive and negative effects. Initially, the positive effects (i) and (ii) play the dominate role of the donor cosubstitution. The negative effect (iii) is subordinate to the positive effects (i) and (ii). This results in a pronounced increase of $2P_r$ with donor cosubstitution levels (Fig 4.56b). However, as the donor cosubstitution level increases, a compromise is achieved between the positive and negative effects, and the $2P_r$ reaches its maximum value. Meanwhile, it also results in low leakage current (Fig 4.54, 4.55) and low polarization fatigue (Fig 4.57). With further increase of the donor cosubstitution level, the negative effect (iii) gradually becomes the dominating effect. Consequently, the $2P_r$ steps down (Fig 4.56b).

4.4.6 Summary

$Bi_{3.25}La_{0.75}Ti_{3-x}M_xO_{12}$, ($BLTM_x$, M = Mo, W, Nb, V, x = 0.0–0.12) ferroelectric nanoparticles and ceramics have been prepared using a modified citrate-gel method, giving several advantages in terms of low crystallization temperature, phase purity, feasibility, and high ferroelectric performance etc. The carbonized amorphous precursor has been found to directly crystallize into the $Bi_4Ti_3O_{12}$ structure at 450 °C. The prepared $BLTM_x$ ceramics show a dependence on the cosubstituted donor and cosubstitution level, with respect to the texture factor ($f = I_{(002)} / (I_{(002)} + I_{(060)})$), microstructure (grain shape and size), and ferroelectric properties (P_r). The decrease of grain size, both in the length and thickness of the platelet-like grains, might be attributed to the slow transport of oxygen ions because of the decrease of oxygen vacancies with donor cosubstitution.[184] The considerable variations in the microstructure of the $BLTM_x$ ceramics cosubstituted with the same valence donors are attributed to the subtle differences in the donor cation size. Because a smaller cation is expected to have a higher mobility than a larger one, thereby resulting in larger grains. The possible presence of low-valent vanadium ions (V^{4+}) could be another reason for the larger grain size of the $BLTV_x$ ceramics than that of $BLTNb_x$ ceramics. The increase of the texture factor f with the donor cosubstitution level is probably a result of the decrease of grain size. The P_r of the $BLTM_x$ ceramics correlates strongly with the cosubstitution level and microstructures. The maximum P_r (about 16 μC cm^{-2}) is achieved at an optimum cosubstitution level (x = 0.025 for M^{6+}, x = 0.03 for M^{5+}). The dynamic leakage current compensation indicates little leakage current contributions to the *P*-*E* hysteresis loops, which is consistent with the static leakage current measurement results. The decrease in the $\pm P_r$ after 4.19×10^8 accumulative switching cycles is less than 7 % in $BLTW_{0.025}$ ceramics, implying the low polarization fatigue of the prepared ceramics. The well-saturated hysteresis loop, low leakage current, and low polarization fatigue render the prepared $BLTM_x$ ferroelectric ceramics are promising for practical applications.

The presented modified citrate-gel method can be readily used to prepare other kind of lanthanoid cation and donor (Nb^{5+}, V^{5+}, Mo^{6+}, W^{6+}) cosubstituted $Bi_4Ti_3O_{12}$ ceramics just by replacing La^{3+} with other cations such as Pr^{3+}, Nd^{3+}, etc. Because the metal species used in this work are common constitutes of bismuth layer-structured perovskite oxides, the reported citrate-gel method is expected to be applicable for the synthesis of other kind of bismuth layer-structured materials and other multicomponent oxides.

4.5 Synthesis of $BaMgF_4$ Nanoparticles

This section presents the preliminary results of the synthesis of $BaMgF_4$ nanoparticles using a hydrothermal method, DMSO mediated coprecipitation method, high temperature surfactant method, and microemulsion method. The products were characterized by XRD and SEM.

4.5.1 Hydrothermal Synthesis

Typical synthesis conditions and products of the hydrothermal synthesis are listed in Table 4.8. It was observed that long reaction time is required to obtain the pure $BaMgF_4$ phase. As seen in Table 4.8, products synthesized at 180 °C for 6 h (BMF1-3) contained BaF_2, even though the reaction temperature was much higher than that of BMF1-1 and 1-2. The product from the direct coprecipitation at 60 °C contained BaF_2, and other unidentified impurity phases.

The XRD pattern of the product obtained from hydrothermal synthesis at 130 °C for 17 h using either DEG or water can be well indexed to the $BaMgF_4$ phase without any detectable impurities, such as BaF_2, MgF_2, or $BaCO_3$ (Fig 4.59). The obtained $BaMgF_4$ particles from synthesis BMF1-1 mainly contained nanocubes with a size about 60 nm, as observed in the SEM image (Fig 4.60). However, larger particles with size over hundred nanometer were also observed.

Table 4.8 Typical hydrothermal synthesis conditions of $BaMgF_4$

No.	$(Ba^{2+} + Mg^{2+})$: mL	(F^-): mL	Temp: °C	Time: h	Phase
BMF1-1	DEG: 20	H_2O: 2	130	17	$BaMgF_4$
BMF1-2	H_2O: 20	H_2O: 2	130	18	$BaMgF_4$
BMF1-3	H_2O: 20 + DEG: 5	H_2O: 2	180	6	$BaMgF_4$, BaF_2

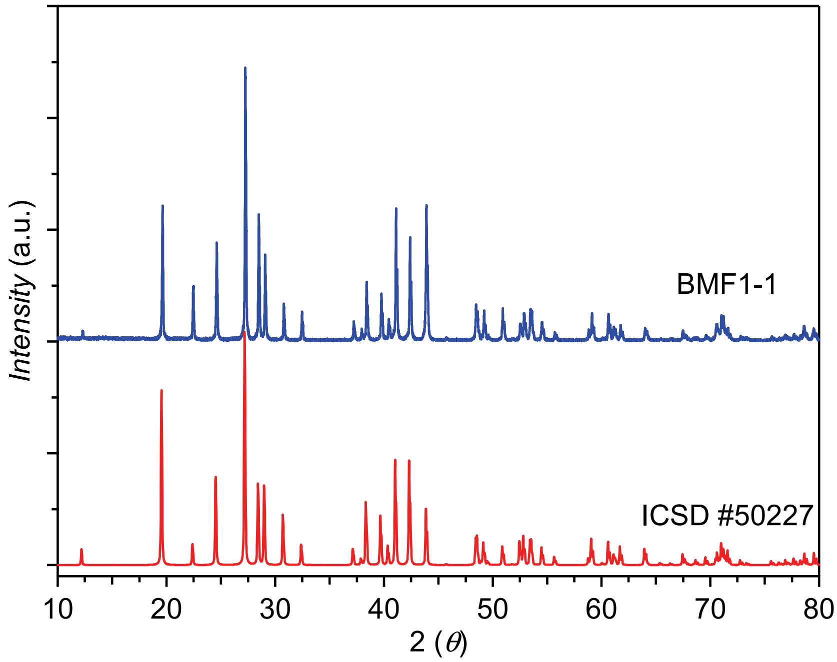

Fig 4.59 XRD pattern of the BMF1-1.

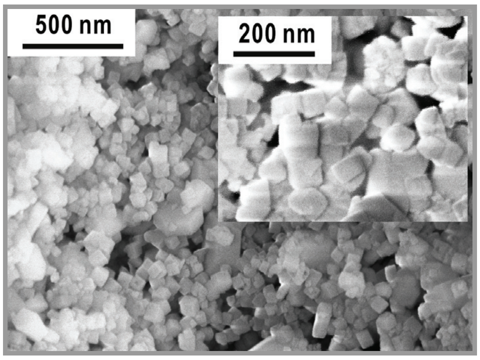

Fig 4.60 SEM images of BMF1-1.

4.5.2 High Temperature Surfactant Method

The synthesis conditions and products of the high temperature surfactant method are listed in Table 4.9. All the synthesized products mainly contained $BaMgF_4$, except one small peak at about 28° in 2θ from an unidentified impurity was observed in the XRD pattern in the product of BMF2-1 and 2-2 (Fig 4.61). All the other diffraction peaks can be well attributed to the $BaMgF_4$ phase. The $BaMgF_4$ particles produced have different size and shape, as observed by SEM (Fig 4.62). As seen in Fig 4.62a, BMF2-1 mainly contains particles with size about 100 nm. Sheet like particles with a size over 200 nm were observed in BMF2-2. However, hexagonal pillars about 200 nm in length and 100 to 150 nm in width were found in BMF2-3. The particles of BMF2-4 were about 200–300 nm, and some particles were cubes (Fig 4.62d inset).

Table 4.9 Synthesis conditions and products of high temperature surfactant method*

No.	Co-surfactant (g)	SS[a] /mL	NH_4F[b] /mL	Temp /°C	Time /h	Phase
BMF2-1	n-butanol: 4.0	4.0	4.0	150	24	$BaMgF_4$[c]
BMF2-2	n-butanol: 4.0	2.0	2.0	150	1	$BaMgF_4$[c]
BMF2-3	Hexanol: 8.4	2.0	2.0	90	24	$BaMgF_4$
BMF2-4	Hexanol: 9.0 Oleic acid: 1.0	2.0	2.0	80 & 115	18 & 1	$BaMgF_4$

* SS: stock solution, 14 g of diphenyl ether and 6.0 g of CTAB was used for all the synthesis; a 0. 25 M of $Ba(NO_3)_2$ and 0. 25 M of $Mg(NO_3)_2$ aqueous solution; b 1.0 M water solution, c XRD pattern has one unindexed peak.

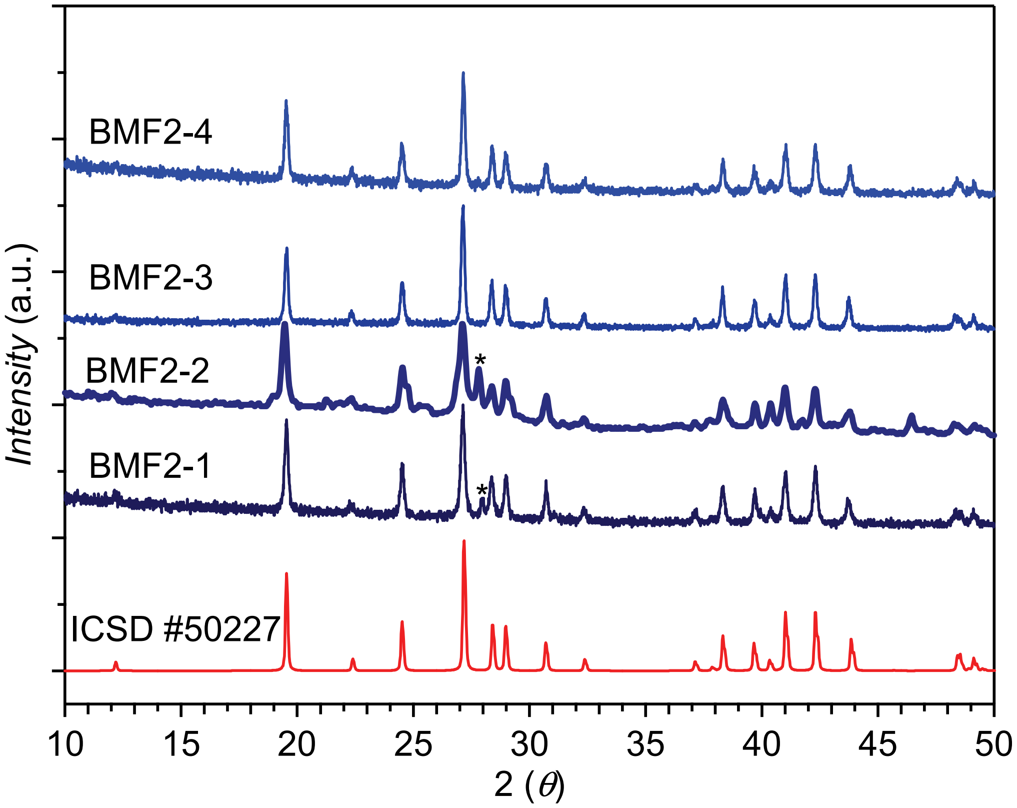

Fig 4.61 XRD patterns of BMF2-x, x = 1–4, * peaks from unindexed impurity.

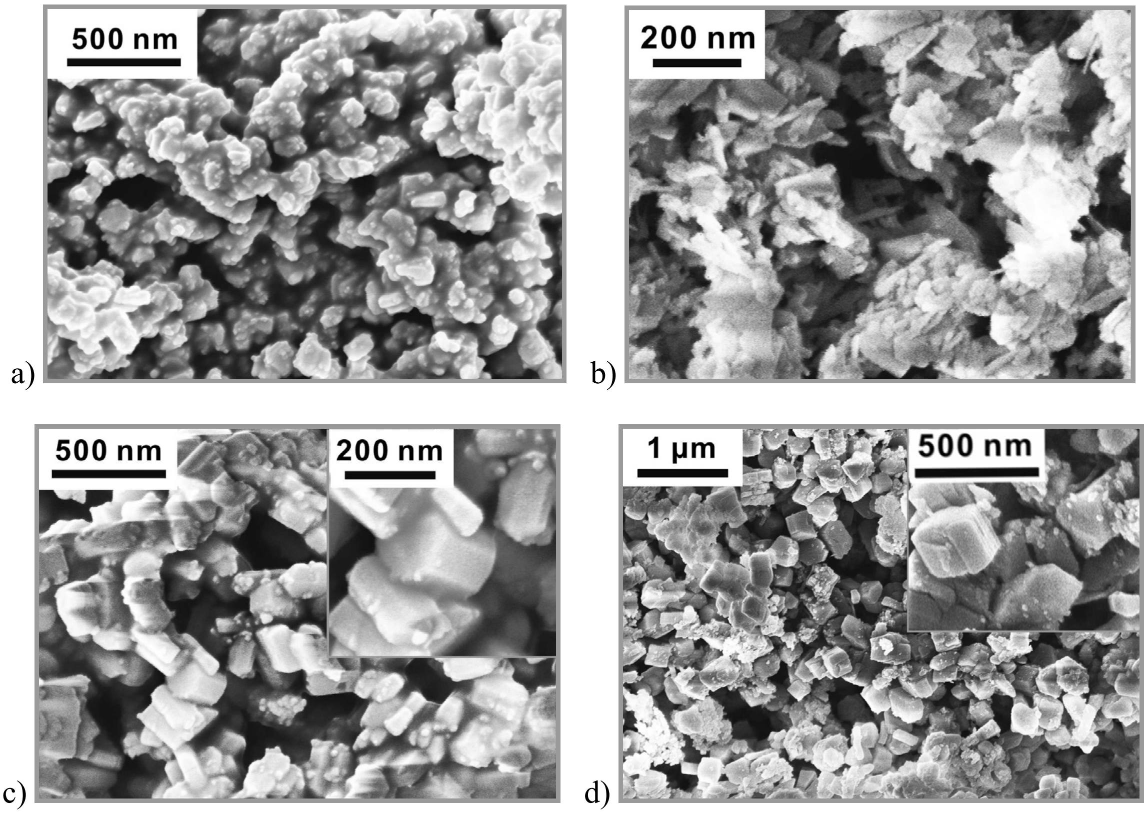

Fig 4.62 SEM images of BMF2-1 (a), 2-2 (b), 2-3 (c), and 2-4 (d), insets: high magnification.

Table 4.10 Synthesis conditions and products of the DMSO mediated coprecipitation.*

Number	DMSO (mL)	Water : HOAc (mL)	Temp (°C)	Time	Product
BMF3-1	40	10 : 0	150	30 min	$BaMgF_4$
BMF3-2	50	10 : 0	150	10 min	$BaMgF_4$
BMF3-3	40	10 : 0	150	5 min	$BaMgF_4$
BMF3-4	40	15 : 0	150	5 min	$BaMgF_4$
BMF3-5	40	10 : 0	150	1 min	$BaMgF_4$
BMF3-6	40	15 : 5	150	5 min	$BaMgF_4$
BMF3-7	50	5 : 0	160	5 min	amorphous
BMF3-8	40	10 : 10	120	5 min	amorphous
BMF3-9	50	30 : 0	120	5 min	amorphous

*1.0 mmol of $Ba(NO_3)_2$ and 1.0 mmol of $Mg(NO_3)_2{\cdot}6H_2O$ were dissolved DMSO, and 4.0 mmol NH_4F was dissolved in water and HOAc.

4.5.3 DMSO Mediated Coprecipitation Method

The synthesis conditions and products are listed in Table 4.10. It can be seen that high quantity of water and high temperature are necessary to obtain crystalline $BaMgF_4$. Synthesis at 150 °C for 1 min gave crystalline $BaMgF_4$ particles (BMF3-5). However, amorphous products were obtained for the synthesis at 120 °C for 5 min (BMF3-8, 3-9). Moreover, water was found to be important to form crystalline $BaMgF_4$. Using 5.0 mL of water produced an amorphous product (BMF3-7), even though the high reaction temperature was 160 °C.

4.5.4 $BaMgF_4$/Polymer Composites

For the preparation of $BaMgF_4$/polymer composites (seen in section 3.4.6.4), the synthesized $BaMgF_4$ particles were mixed with TMPTA (and/or BDMA, monomer) and TPO (initiator). The mixture was injected between tow glass slides with a spacer and polymerized in a UV box.

The prepared composites were characterized by XRD and UV/Vis spectroscopy. As seen in Fig 4.63, the (021) and (111) diffraction peaks of $BaMgF_4$ were observed in the $BaMgF_4$/TMPTA composite containing 0.5 wt% $BaMgF_4$. The intensity of the diffraction peaks attributed to $BaMgF_4$ increases with the $BaMgF_4$ loading level, and almost all the diffraction peaks belonging to $BaMgF_4$ were observed in the composite containing 2.0 wt% $BaMgF_4$. These observed diffraction peaks confirm the presence of crystalline $BaMgF_4$ particles in the final $BaMgF_4$/polymer composites. Fig 4.64 shows the UV/Vis spectra of the $BaMgF_4$/TMPTA composites. The transmittance for the composites containing 0.5 % $BaMgF_4$ is about 80 % at a wavelength of 800 nm. However, the transmittance decreased at shorter wavelength and was less than 50 % at a wavelength of 400 nm. The transmittance decreases significantly with the increase of the $BaMgF_4$ content. The transmittance for the composites containing 2.0 % $BaMgF_4$ was below 50 % in the visible range.

Diffraction peaks attributed to $BaMgF_4$ were also observed in the $BaMgF_4$/BDMA composite containing about 1.0 wt% $BaMgF_4$ (Fig 4.65). The $BaMgF_4$/BDMA composite has a higher transmittance at a wavelength above 450 nm than that of $BaMgF_4$/TMPTA composite with the same loading level (Fig 4.66). This was because in the preparation of $BaMgF_4$/BDMA composite, oleic acid was used for size selection (section 3.4.6.4), thereby only fine particles were loaded in the final composites.

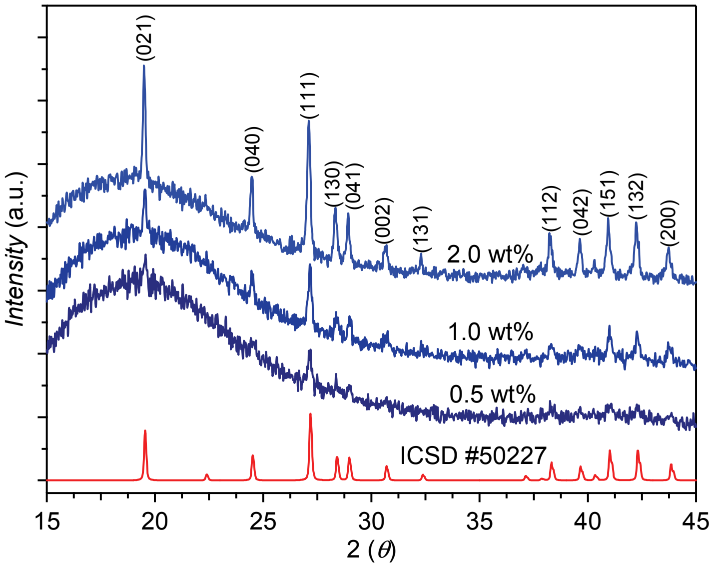

Fig 4.63 XRD patterns of the BMF/TMPTA composites with thickness of 1.5 mm.

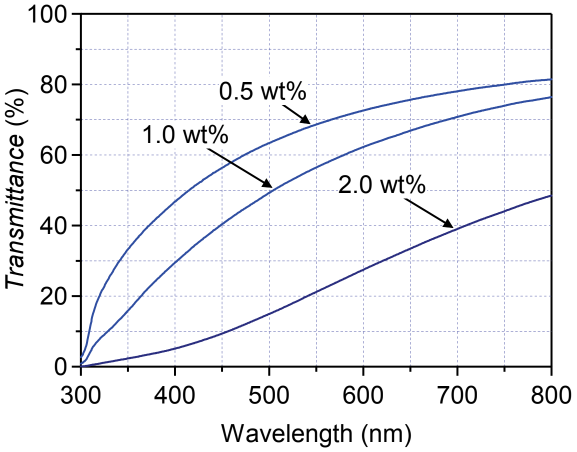

Fig 4.64 UV/Vis Spectra of the BMF/TMPTA composites with thickness of 1.5 mm.

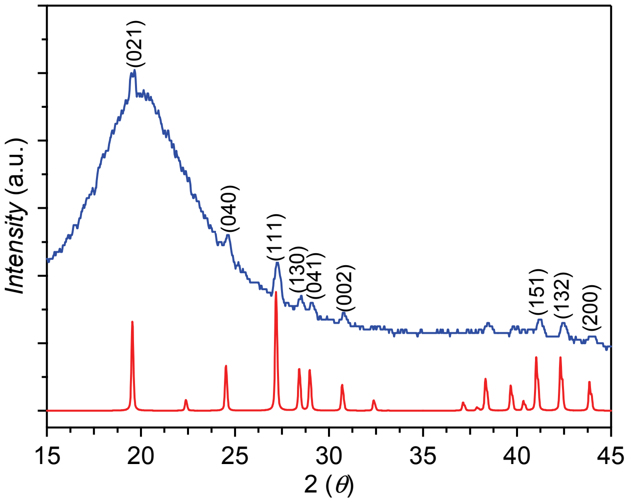

Fig 4.65 XRD pattern of a $BaMgF_4$/BDMA composite (1.0 wt%) with thickness of 1.5 mm.

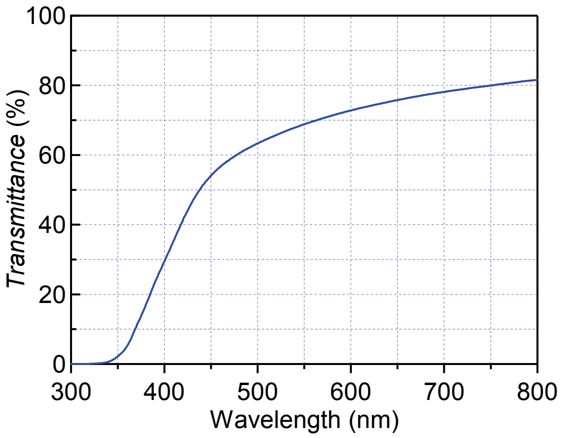

Fig 4.66 UV/Vis spectrum of a $BaMgF_4$/BDMA composite (1.0 wt%) with thickness of 1.5 mm.

4.5.5 Summary

Several synthesis methods were used to prepare $BaMgF_4$ nanoparticles. Crystalline $BaMgF_4$ nanoparticles with size about 60 nm have been prepared by a hydrothermal method using DEG as solvent. However, larger particles with size over hundred nanometer were also observed. The DMSO mediated coprecipitation yielded pure crystalline $BaMgF_4$ at 150 °C for 5 min. By a high temperature surfactant method, $BaMgF_4$ powders with different morphology were prepared. Pure crystalline $BaMgF_4$ was obtained from a synthesis at 90 °C for 24 h, and from a two step heating process, at 80 °C for 18 h and then at 115 °C for 1 h.

Two kinds of $BaMgF_4$/polymer composites were prepared. The observed diffraction peaks confirm the presence of crystalline $BaMgF_4$ particles in the final $BaMgF_4$/polymer composites. The transmittance for the $BaMgF_4$/TMPTA composites containing 0.5 % $BaMgF_4$ is about 80 % at a wavelength of 800 nm. However, the transmittance decreased at shorter wavelength and was less than 50 % at a wavelength of 400 nm. Improved transmittance was achieved by the use of oleic acid for size selection in the preparation of the $BaMgF_4$/BDMA composite.

5. Conclusion and Outlook

In conclusion, $BaTiO_3$ nanocrystals, $Bi_4Ti_3O_{12}$ nanostructured microspheres, and cosubstituted $Bi_4Ti_3O_{12}$ nanoparticles and ceramics were prepared using solvothermal, hydrothermal and citrate-gel method. The ferroelectric properties of the prepared cosubstituted $Bi_4Ti_3O_{12}$ ceramics were studied using P–E hysteresis loop, leakage, and fatigue measurements.

Using an oil/water two-phase solvothermal method, oil soluble $BaTiO_3$ nanocrystals with a mean size of 3.7 nm were prepared. The $BaTiO_3$ nanocrystals are among the smallest isolated $BaTiO_3$ nanocrystals reported so far. According to XRD and TEM studies the materials have a high phase purity, crystallinity, and uniform crystallite size. More important, $BaTiO_3$ nanocrystals synthesized by the two-phase approach can be dispersed in conventional organic solvents to form highly transparent dispersions. The high hydrophobicity and dispersibility results from the grafted surfactant molecules on the surface of the $BaTiO_3$ nanocrystals. The latter is important to form the uniform nanocrystals with small size, the highly transparent dispersions, and the homogeneous transparent nanocomposites. Even though cubic $BaTiO_3$ is not ferroelectric, the synthesized $BaTiO_3$ nanocrystals are interesting candidates for the investigation of size effects in nanoscale dielectrics, and in the fabrication of novel nanostructures using spin-coating methods for integrated electrooptic and high dielectric applications. The developed oil/water two-phase method in principle is applicable to synthesize other kind of nanocrystals through chemical reaction between metal surfactant complexes in oil phase and a mineralizer in water phase.

Nanostructured microspheres consisting of crystalline $Bi_4Ti_3O_{12}$ were prepared by a hydrothermal synthesis method using precursor powder from a DEG mediated coprecipitation. By changing the synthesis conditions, such as precursor quantity, mineralizer concentration, and reaction time, the morphologies could be tailored from 20 nm granular nanoparticles to nano-platelets with different thickness. XRD and SEM results show a higher degree of crystallinity for increasing NaOH concentration and reaction time. The formation of the nanostructured microspheres can be explained by a dissolution and subsequent recrystallization process. Since several complex oxides have important electric, magnetic, and electro-optical properties, the synthesis of nanostructured complex oxides will provide new opportunities for the exploration of structure- or morphology-dependent properties.

$Bi_{3.25}Pr_{0.75}Ti_{2.97}V_{0.03}O_{12}$ and $Bi_{3.25}La_{0.75}Ti_{3-x}M_xO_{12}$, (BLTM$_x$, M = Mo, W, Nb, V, x = 0.0–0.12) ferroelectric nanoparticles and ceramics were synthesized using a modified citrate-gel method that has a crystallization temperature as low as 450 °C. The carbonized amorphous precursor was directly transformed into crystalline $Bi_4Ti_3O_{12}$. The synthesized nanoparticles were spherical ranging from 30 to 100 nm. Except Nb^{5+}, other donor cations were introduced using the corresponding oxides that have advantages in terms of high purity, low cost, and wide availability. In general, the presented modified citrate-gel method is applicable for the synthesis of other bismuth layer-structured materials or other kind of multi-component oxides.

The Rietveld refinement in the orthorhombic space group $Aea2$ for the as-prepared Pr^{3+} and V^{5+} cosubstituted $Bi_4Ti_3O_{12}$ resulted in a convergent refinement (R_{wp} = 5.01 %). The $Bi_{3.25}Pr_{0.75}Ti_{2.97}V_{0.03}O_{12}$ ceramic prepared from the as-synthesized powder consisted of randomly arranged platelets with a thickness of about 200 nm. The $Bi_{3.25}Pr_{0.75}Ti_{2.97}V_{0.03}O_{12}$

ceramic has $2P_r$ and $2E_c$ values measured at 300 kV/cm as high as 35 µC/cm^2 and 148 kV/cm respectively. The observed linear relationship between P_{max}/P_r and E_{max} was interpreted as an ideal and a four components ferroelectric capacitor model for the calculation of the field independent dielectric constant and nonremanent polarization. The $Bi_{3.25}Pr_{0.75}Ti_{2.97}V_{0.03}O_{12}$ ceramic shows ohmic conductivity with current density below 1.0 µA/cm^2. No significant decrease of P_r was observed after switching over 10^8 cycles. The well saturated hysteresis loop, low leakage, and low polarization fatigue is promising for applications in devices.

The texture, microstructure, and ferroelectric properties of the prepared $Bi_{3.25}La_{0.75}Ti_{3-x}M_xO_{12}$, (BLTM$_x$, M = Mo, W, Nb, V, x = 0.0–0.12) ceramics show great dependence on the cosubstituted donor and cosubstitution level. The decrease of grain size with x was observed that could be explained by the slow transport of oxygen ions. The former might be related to the change of grain orientations in the ceramic platelets. The P_r of the BLTM$_x$ ceramics correlates strongly with the cosubstitution level and microstructures. The maximum P_r (about 16 µC cm^{-2}) is achieved at an optimum cosubstitution level (x = 0.025 for M^{6+}, x = 0.03 for M^{5+}). At these substitution levels, the BLTM$_x$ ceramics have well saturated hysteresis loop, low leakage current, and low polarization fatigue, rendering them as competitive lead-free ferroelectric materials for practical applications.

Several synthesis methods were used to prepare $BaMgF_4$ nanoparticles. Crystalline $BaMgF_4$ nanoparticles with a size about 60 nm were prepared by a hydrothermal method using DEG as solvent. However, larger particles with size over hundred nanometer were also observed. The DMSO mediated coprecipitation yielded pure crystalline $BaMgF_4$ at 150 °C for 5 min. By a high temperature surfactant method, $BaMgF_4$ powders with different morphology were obtained. Pure crystalline $BaMgF_4$ was obtained from a synthesis at 90 °C for 24 h, and from a two step heating process, at 80 °C for 18 h and then at 115 °C for 1 h.

Two kinds of $BaMgF_4$/polymer composites were prepared. The observed diffraction peaks confirm the presence of crystalline $BaMgF_4$ particles in the final $BaMgF_4$/polymer composites. The transmittance for the $BaMgF_4$/TMPTA composites containing 0.5 % $BaMgF_4$ is about 80 % at a wavelength of 800 nm. However, the transmittance decreased as the wavelength reduced and it was less than 50 % at a wavelength of 400 nm. Improved transmittance was achieved by the use of oleic acid for size selection in the preparation of the $BaMgF_4$/BDMA composite.

The present studies can be extended to relate topics not explored yet, which are suggested for future research.

$BaTiO_3$ single nanocrystal electric properties may be studied using scanning probe microscopy. The $BaTiO_3$ single nanocrystal optical properties can be explored using the single particle spectroscopy. Using the developed oil/water two-phase method, other kind of nanocrystals may be synthesized, such as $SrTiO_3$, ZnS, etc. The recrystallization process observed in the formation of $Bi_4Ti_3O_{12}$ nanostructured microspheres may be used to grow oriented $Bi_4Ti_3O_{12}$ films by hydrothermal treatment of the amorphous film on a substrate. Preparation and characterization of $Bi_{3-y}Ln_yTi_{3-x}M_xO_{12}$, (Ln = Pr^{3+}, Nd^{3+}, etc., M = Mo, W, Nb, V) could be interesting, especially concerning the microstructure and ferroelectric properties of ceramics. A comparison of the grain size and microstructures of pure and/or substituted $Bi_4Ti_3O_{12}$ ceramics prepared in oxidative and reductive atmospheres will provide a better understanding of the role of oxygen vacancies in the grain growth.

References

1. Scott, J. F. *Science* **2007,** 315, 954-959.
2. Muralt, P. *J. Micromech. Microeng.* **2000,** 10, 136-146.
3. Lang, S. B. *Phys. Today* **2005**, 31-36.
4. Damjanovic, D. *Rep. Prog. Phys.* **1998,** 61, 1267-1324.
5. Scott, J. F., *Overview.* In *Ferroelectric Random Access Memories*, Ishiwara, H.; Okuyama, M.; Arimoto, Y., Eds. Springer: Berlin Heidelberg, 2004; pp 3-16.
6. Kotecki, D. E.; Baniecki, J. D.; Shen, H.; Laibowitz, R. B.; Saenger, K. L.; Lian, J. J.; Shaw, T. M.; Althavale, S. D.; Jr., C. C.; Duncombe, P. R.; Gutsche, M.; Kunkel, G.; Park, Y.-J.; Wang, Y.-Y.; Wise, R. *IBM J. Res. Develop.* **1999,** 43, 367-382.
7. Sugibuchi, K.; Kurogi, Y.; Endo, N. *J. Appl. Phys.* **1975,** 46, 2877-2881.
8. Fu, H.; Bellaiche, L. *Phys. Rev. Lett.* **2003,** 91, 257601-4.
9. Dawber, M.; Rabe, K. M.; Scott, J. F. *Rev. Mod. Phys.* **2005,** 77, 1083-1130.
10. Herrig, H.; Hempelmann, R. *Mater. Lett.* **1996,** 27, 287-292.
11. Herrig, H.; Hempelmann, R. *Nanostruct. Mater.* **1997,** 9, 241-244.
12. O'Brien, S.; Brus, L.; Murray, C. B. *J. Am. Chem. Soc.* **2001,** 123, 12085-12086.
13. Niederberger, M.; Pinna, N.; Polleux, J.; Antonietti, M. *Angew. Chem. Int. Ed.* **2004,** 43, 2270-2273.
14. Niederberger, M.; Garnweitner, G.; Pinna, N.; Antonietti, M. *J. Am. Chem. Soc.* **2004,** 126, 9120-9126.
15. Subbarao, E. C.; Banavar, J.; Bhalla, A. S.; Cross, L. E.; Kurtz, S. K.; Newnham, R. E.; Roy, R. *Phase Transitions* **1990,** 22, 157-166.
16. Cummins, S. E.; Cross, L. E. *J. Appl. Phys.* **1968,** 39, 2268-2274.
17. Irie, H.; Miyayama, M.; Kudo, T. *J. Appl. Phys.* **2001,** 90, 4089-4094.
18. Si, J.; Desu, S. B. *J. Appl. Phys.* **1993,** 73, 7910-7913.
19. Wang, H.; Fu, L. W.; Shang, S. X. *J. Appl. Phys.* **1993,** 73, 7963-7965.
20. Yamaguchi, M.; Nagatomo, T.; Omoto, O. *Jpn. J. Appl. Phys.* **1997,** 36, 5885-5888.
21. Yamaguchi, M.; Nagatomo, T. *Jpn. J. Appl. Phys.* **1998,** 37, 5166-5170.
22. Joshi, P. C.; Krupanidhi, S. B.; Mansingh, A. *J. Appl. Phys.* **1992,** 72, 5517-5519.
23. Noguchi, Y.; Miwa, I.; Goshima, Y.; Miyayama, M. *Jpn. J. Appl. Phys.* **2000,** 39, L1259-L1262.
24. Noguchi, Y.; Miyayama, M. *Appl. Phys. Lett.* **2001,** 78, 1903-1905.
25. Uchida, H.; Okada, I.; Matsuda, H.; Iijima, T.; Watanabe, T.; Funakubo, H. *Integr. Ferroelec.* **2003,** 52, 41-54.
26. Noguchi, Y.; Soga, M.; Takahashi, M.; Masaru, M. *Jpn. J. Appl. Phys.* **2005,** 44, 6998-7022.

27. Park, B. H.; Hyun, S. J.; Bu, S. D.; Noh, T. W.; Lee, J.; Kim, H. D.; Kim, T. H.; Jo, W. *Appl. Phys. Lett.* **1999,** 74, 1907-1909.
28. Park, B. H.; Kang, B. S.; Bu, S. D.; Noh, T. W.; Lee, J.; Jo, W. *Nature* **1999,** 401, 682-684.
29. Kang, B. S.; Park, B. H.; Bu, S. D.; Kang, S. H.; Noh, T. W. *Appl. Phys. Lett.* **1999,** 75, 2644-2646.
30. Lee, H. N.; Hesse, D.; Zakharov, N.; Gösele, U. *Science* **2002,** 296, 2006-2009.
31. Chon, U.; Jang, H. M.; Kim, M. G.; Chang, C. H. *Phys. Rev. Lett.* **2002,** 89, 087601-087604.
32. Lin, W.-T.; Ko, C.-Y. *J. Crystal Growth* **2006,** 293, 365-369.
33. Li, W.; Yin, Y.; Su, D.; Zhu, J. *J. Appl. Phys.* **2005,** 97, 084102-9.
34. Ohki, H.; Wang, X.; Ishiwara, H. *Jpn. J. Appl. Phys.* **2005,** 44, 964-967.
35. Uchida, H.; Yoshikawa, H.; Okada, I.; Matsuda, H.; Iijima, T.; Watanabe, T.; Funakubo, H. *Jpn. J. Appl. Phys.* **2002,** 41, 6820-6824.
36. Uchida, H.; Yoshikawa, H.; Okada, I.; Matsuda, H.; Iijima, T.; Watanabe, T.; Kojima, T.; Funakubo, H. *Appl. Phys. Lett.* **2002,** 81, 2229-2231.
37. Uchida, H.; Okada, I.; Matsuda, H.; Iijima, T.; Watanabe, T.; Funakubo, H. *Jpn. J. Appl. Phys.* **2004,** 43, 2636-2639.
38. Ahn, C. W.; Lee, H. J.; Kim, I. W.; Lee, J. S.; Lee, W. K. *Ferroelectr.* **2006,** 331, 129-134.
39. Tang, Q.-Y.; Kan, Y.-M.; Li, Y.-G.; Zhang, G.-J.; Wang, P.-L. *Solid State Comm.* **2007,** 142, 1-5.
40. Ahn, C.; Lee, H.; Kang, S.; Kim, I.; Choi, M.; Lee, J. *J. Electroceram.* **2006,** 17, 169-172.
41. *IEEE Trans. Ultrason. Ferroelectr. Freq. Control* **2003,** 50, 1613-1646.
42. Haeni, J. H.; Irvin, P.; Chang, W.; Uecker, R.; Reiche, P.; Li, Y. L.; Choudhury, S.; Tian, W.; Hawley, M. E.; Craigo, B.; Tagantsev, A. K.; Pan, X. Q.; Streiffer, S. K.; Chen, L. Q.; Kirchoefer, S. W.; Levy, J.; Schlom, D. G. *Nature* **2004,** 430, 758.
43. Lines, M. E.; Glass, A. M., *Principles and Applications of Ferroelectrics and Related Materials*. Oxford University: Oxford, 1977.
44. Valasek, J. *Phys. Rev.* **1921,** 17, 475-481.
45. Busch, G.; Scherer, P. *Naturwiss.* **1935,** 23, 737-738.
46. Roberts, S. *Phys. Rev.* **1947,** 71, 890-895.
47. von Hippel, A.; Breckenridge, R. G.; Chesley, F. G.; Tisza, L. *Ind. Eng. Chem.* **1946,** 38, 1097-1109.
48. von Hippel, A. *Rev. Mod. Phys.* **1950,** 22, 221-237.
49. Shirane, G.; Hoshino, S.; Suzuki, K. *Phys. Rev.* **1950,** 80, 1105-1106
50. Uitert, L. G. V.; Egerton, L. *J. Appl. Phys.* **1961,** 32, 959-959.
51. Subbarao, E. C. *Phys. Rev.* **1961,** 122, 804-807.

52. Matthias, B. T.; Remeika, J. P. *Phys. Rev.* **1949,** 76, 1886-1887.
53. Kepler, R. G. *Annu. Rev. Phys. Chem.* **1978,** 29, 497-518.
54. Scott, J. F.; Zubko, P. In *Electret effects in ferroelectric thin films*, 12th International Symposium on Electrets 2005; pp 113-116.
55. Klapper, H.; Hahn, T., *Point-Group Symmetry and Physical Properties of Crystals.* In *International Tables for Crystallography*, Hahn, T., Ed. Springer: Dordrecht, 2006; Vol. A, pp 804-808.
56. Waser, R.; Böttger, U.; Grossmann, M., *Static and Dynamic Properties of Domains.* In *Ferroelectric Random Access Memories*, Ishiwara, H.; Okuyama, M.; Arimoto, Y., Eds. Springer: Berlin Heidelberg, 2004; Vol. 93, pp 31-45.
57. Böttger, U., *Dielectric Properties of Polar Oxide.* In *Polar Oxide: Properties, Characterization, and Imaging*, Waser, R.; Böttger, U.; Tiedke, S., Eds. Wiley-VCH: Weinheim, 2005; pp 11-38.
58. Tagantsev, A. K.; Stolichnov, I.; Colla, E. L.; Setter, N. *J. Appl. Phys.* **2001,** 90, 1387-1402.
59. Warren, W. L.; Tuttle, B. A.; Dimos, D. *Appl. Phys. Lett.* **1995,** 67, 1426-1428.
60. Jiang, Q. Y.; Subbarao, E. C.; Cross, L. E. *J. Appl. Phys.* **1994,** 75, 7433-7443.
61. Park, C. H.; Chadi, D. J. *Phys. Rev. B* **1998,** 57, R13 961-R13 964.
62. Scott, J. F.; Dawber, M. *Appl. Phys. Lett.* **2000,** 76, 3801-3803.
63. Verdier, C.; Morrison, F. D.; Lupascu, D. C.; Scott, J. F. *J. Appl. Phys.* **2005,** 97, 024107-6.
64. Goodenough, J. B. *Rep. Progr. Phys.* **2004,** 67, 1915-1993.
65. Goldschmidt, V. M. *Trans. Farad. Soc.* **1929,** 25, 0253-0282.
66. Bhalla, A. S.; Guo, R.; Roy, R. *Mat. Res. Innovat.* **2000,** 4, 3-26.
67. Goldschmidt, V. M. *Naturwiss.* **1926,** 14, 477-485.
68. Megaw, H. D. *Proc. Phys. Soc.* **1946,** 58, 133-152.
69. The phase transition temperature can be hysteretic, and can depend on the boundary conditions. Typical values are given.
70. Swartz, S. L. *IEEE Trans. Electr. Insulat.* **1990,** 25, 935-987.
71. Cross, L. E., *Ferroelectric ceramics: tailoring properties for specific applications.* Birkhauser Verlag: Basel Switzerland; Boston, MA, USA, 1993; p 1-85.
72. Collaboration: Authors and editors of the volumes, I. H. I. E., *BaTiO3 crystal structure, lattice parameters.* In *Ternary Compounds, Organic Semiconductors*, Springer: 2000; pp 1-6.
73. Merz, W. J. *Phys. Rev.* **1949,** 76, 1221-1225.
74. Shirane, G.; Pepinsky, R.; Frazer, B. C. *Acta Cryst.* **1956,** 9, 131-140.
75. Aurivillius, B. *Arkiv Kemi* **1950,** 1, 499-512.
76. Aurivillius, B. *Arkiv Kemi* **1950,** 1, 463-480.
77. Aurivillius, B. *Arkiv Kemi* **1951,** 2, 519-527.

78. Yokoi, A.; Ogawa, H. *Mater. Sci. Eng., B* **2006,** 129, 80-85.
79. Mercurio, D.; Trolliard, G.; Hansen, T.; Mercurio, J. P. *Int. J. Inorg. Mater.* **2000,** 2, 397-406.
80. Withers, R. L.; Thompson, J. G.; Rae, A. D. *J. Solid State Chem.* **1991,** 94, 404-417.
81. Noguchi, Y.; Murata, K.; Miyayama, M. *Appl. Phys. Lett.* **2006,** 89, 242916-3.
82. Wu, Y.; Cao, G. *J. Mater. Res.* **2000,** 15, 1583-1590.
83. Ogawa, H.; Yokoi, A.; Taketani, H. *Jpn. J. Appl. Phys.* **2005,** 44, 7003-7007.
84. Irie, H.; Masaru, M. *Appl. Phys. Lett.* **2001,** 79, 251-253.
85. Yan, H.; Zhang, H.; Ubic, R.; Reece, M. J.; Liu, J.; Shen, Z.; Zhang, Z. *Adv. Mater.* **2005,** 17, 1261-1265.
86. de Araujo, C. A. P.; Cuchiaro, J. D.; McMillan, L. D.; Scott, M. C.; Scott, J. F. *Nature* **1995,** 374, 627-629.
87. Yamada, M.; Iizawa, N.; Yamaguchi, T.; Sakamoto, W.; Kikuta, K.; Yago, T.; Hayashi, T.; Hirano, S.-i. *Jpn. J. Appl. Phys.* **2003,** 42, 5222-5226.
88. Duiker, H. M.; Beale, P. D.; Scott, J. F.; de Araujo, C. A. P.; Melnick, B. M.; Cuchiaro, J. D.; McMillan, L. D. *J. Appl. Phys.* **1990,** 68, 5783-5791.
89. Mihara, T.; Watanabe, H.; Araujo, C. A. P. d. *Jpn. J. Appl. Phys.* **1994,** 33, 5281-5286.
90. Wolfe, R. W.; Newnham, R. E. *J. Electrochem. Soc.* **1969,** 116, 832-835.
91. Yi, I.-S.; Miyayama, M. *Jpn. J. Appl. Phys.* **1997,** 36, L1321-L1324.
92. Watanabe, T.; Funakubo, H.; Osada, M.; Noguchi, Y.; Miyayama, M. *Appl. Phys. Lett.* **2002,** 80, 100-102.
93. Ravez, J. *J. Phys. III France* **1997,** 7, 1129-1144.
94. Flocken, J.; Mo, Z.; Mei, W. N.; Hardy, J. R.; Hatch, D. M. *Phys. Rev. B* **1994,** 49, 5811-5816.
95. Weber, M. J., *Handbook of Optical Materials*. CRC Press LLC: 2003.
96. Eibschütz, M.; Holmes, L.; Guggenheim, H. J.; Cox, D. E. *Phys. Rev. B* **1972,** 6, 2677-2683.
97. Voronova, V.; Shiran, N.; Gektin, A.; Nesterkina, V.; Shimamura, K.; Ichinose, N. *Phys. Stat. Sol. (c)* **2005,** 2, 543-546.
98. Waser, R.; Smyth, D. M., *Defect chemistry, conduction, and breakdown mechanism of perovskite-structure titanates.* In *Ferroelectric Thin Films: Synthesis and Basic Properties*, Araujo, C. P. d.; Scott, J. F.; Taylor, G. W., Eds. Gordon and Breach: Amsterdam, 1996; pp 47-92.
99. Cohen, R. E. *Nature* **1992,** 358, 136-138.
100. Mehta, R. R.; Silverman, B. D.; Jacobs, J. T. *J. Appl. Phys.* **1973,** 44, 3379-3385.
101. Dawber, M.; Scott, J. F. *Jpn. J. Appl. Phys.* **2002,** 41, 6848-6851.
102. Wang, X.; Zhuang, J.; Peng, Q.; Li, Y. *Nature* **2005,** 437, 121-124.
103. Kockrick, E.; Krawiec, P.; Schnelle, W.; Geiger, D.; Schappacher, F. M.; Pötgen, R.; Kaskel, S. *Adv. Mater.* **2007,** 19, 3021-3026.

104. Shrout, T. R.; Swartz, S. L. In *Processing of ferroelectric and related materials: a review*, Proceedings of the Eighth IEEE International Symposium on Applications of Ferroelectrics, Piscataway, N. J., 1992; IEEE: pp 80-88.

105. Flaschen, S. S. *J. Am. Chem. Soc.* **1955,** 77, 6194-6194.

106. Qi, J. Q.; Wang, Y.; Chen, W. P.; Li, L. T.; Chan, H. L. W. *J. Solid State Chem.* **2005,** 178, 279-284.

107. Pithan, C.; Hennings, D.; Waser, R. *Int. J. Appl. Ceram. Technol.* **2005,** 2, 1-14.

108. Siemons, M.; Weirich, T.; Mayer, J.; Simon, U. *Z. Anorg. Allg. Chem.* **2004,** 630, 2083-2089.

109. Cushing, B. L.; Kolesnichenko, V. L.; O'Connor, C. J. *Chem. Rev.* **2004,** 104, 3893-3946.

110. Du, Y.; Fang, J.; Zhang, M.; Hong, J.; Yin, Z.; Zhang, Q. *Mater. Lett.* **2002,** 57, 802-806.

111. Pileni, M. P. *J. Phys. Chem.* **1993,** 97, 6961-6973.

112. Sakabe, Y.; Yamashita, Y.; Yamamoto, H. *J. Eur. Ceram. Soc.* **2005,** 25, 2739-2742.

113. Pithan, C.; Shiratori, Y.; Waser, R.; Dornseiffer, J.; Haegel, F.-H. *J. Am. Ceram. Soc.* **2006,** 89, 2908-2916.

114. Leonard, K. J.; Sathyamurthy, S.; Paranthaman, M. P. *Chem. Mater.* **2005,** 17, 4010-4017.

115. Xie, L.; Ma, J.; Zhao, Z.; Tian, H.; Zhou, J.; Wang, Y.; Tao, J.; Zhu, X. *Colloid Surf. A Physicochem. Eng. Asp.* **2006,** 280, 232-236.

116. Byrappa, K.; Yoshimura, M., *Handbook of Hydrothermal Technology*. William Andrew: Norwich, New York, 2001; p 1-52.

117. Feng, S.; Xu, R. *Acc. Chem. Res.* **2001,** 34, 239-247.

118. Rabenau, A. *Angew. Chem. Int. Ed.* **1985,** 24, 1026-1040.

119. Dutta, P. K.; Gregg, J. R. *Chem. Mater.* **1992,** 4, 843-846.

120. Xia, C.-T.; Shi, E.-W.; Zhong, W.-Z.; Guo, J.-K. *J. Eur. Ceram. Soc.* **1995,** 15, 1171-1176.

121. Xia, C.-T.; Shi, E.-W.; Zhong, W.-Z.; Guo, J.-K. *J. Crystal Growth* **1996,** 166, 961-966.

122. Chen, H.-J.; Chen, Y.-W. *Ind. Eng. Chem. Res.* **2003,** 42, 473-483.

123. Testino, A.; Buscaglia, M. T.; Buscaglia, V.; Viviani, M.; Bottino, C.; Nanni, P. *Chem. Mater.* **2004,** 16, 1536-1543.

124. Shi, Y.; Cao, C.; Feng, S. *Mater. Lett.* **2000,** 46, 270.

125. Xu, H.; Bowman, K. J.; Slamovich, E. B. *J. Am. Ceram. Soc.* **2003,** 86, 1815-1817.

126. Yang, Q.; Li, Y.; Yin, Q.; Wang, P.; Cheng, Y.-B. *J. Eur. Ceram. Soc.* **2003,** 23, 161-166.

127. Pookmanee, P.; Uriwilast, P.; Phanichpant, S. *Ceram. Int.* **2004,** 30, 1913-1915.

128. Walton, R. I. *Chem. Soc. Rev.* **2002,** 31, 230-238.

129. Sale, F. R. In *The citrate-gel processing of electronic and magnetic ceramics*, IEE Colloquium on Sol-gel Materials for Device Applications, London, UK, 1998; IEE: Vol.412, pp 4/1-4/7.

130. Schwartz, R. W. *Chem. Mater.* **1997,** 9, 2325-2340.

131. Dhage, S. R.; Khollam, Y. B.; Dhespande, S. B.; Potdar, H. S.; Ravi, V. *Mater. Res. Bull.* **2004,** 39, 1993-1998.

132. Murugan, A. V.; Navale, S. C.; Ravi, V. *Mater. Lett.* **2006,** 60, 1023-1025.

133. Murugan, A. V.; Gaikwad, A. B.; Samuel, V.; Ravi, V. *Ceram. Int.* **2007,** 33, 569-571.

134. Gaikwad, S. P.; Pasricha, R.; Ravi, V. *Mater. Sci. Eng. B* **2005,** 117, 159-161.

135. Gaikwad, S. P.; Samuel, V.; Pasricha, R.; Ravi, V. *Mater. Lett.* **2004,** 58, 3729-3731.

136. Gaikwad, S. P.; Samuel, V.; Pasricha, R.; Ravi, V. *Bull. Mater. Sci.* **2005,** 28.

137. Simões, A. Z.; Aguiar, E. C.; Ries, A.; Longo, E.; Varela, J. A. *Mater. Lett.* **2007,** 61, 588-591.

138. Pechini, M. P. US Patent No.3,330,697, 1967.

139. Chu, R. Q.; Xu, Z. J.; Zhu, Z. Q.; Li, G. R.; Yin, Q. R. *Mater. Sci. Eng., B* **2005,** 122, 106-109.

140. Liu, W. L.; Xia, H. R.; Han, H.; Wang, X. Q. *J. Mater. Sci.* **2005,** 40, 1827-1829.

141. Langford, J. I.; Wilson, A. J. C. *J. Appl. Cryst.* **1978,** 11, 102-113.

142. Amelinckx, S.; Dyck, D. v.; Landuyt, J. v.; Tendeloo, G. v., *Electron Microscopy: Principles and Fundamentals*. VCH Verlagsgesellschaft mbH: Weinheim, Germany, 1997.

143. Goodhew, P. J.; Humphreys, J.; Beanland, R., *Electron Microscopy and Analysis*. Third ed.; Taylor & Francis: London and New York, 2001.

144. Liu, J., *Scanning Transmission Electron Microscopy of Nanoparticles.* In *Characterization of Nanophase Materials*, Wang, Z. L., Ed. Wiley-VCH: Weinheim, 2000; pp 81-132.

145. Moseley, H. G. J. *Phil. Mag.* **1913,** 26, 1024-1034.

146. Wang, Z. L. *Adv. Mater.* **2003,** 15, 1497-1514.

147. Ma, H.; Shieh, K.-J.; Qiao, T. X. *Nature and Science* **2006,** 4, 14-22.

148. Prume, K.; Schmitz, T.; Tiedke, S., *Electrical Characterization of Ferroelectrics.* In *Polar Oxide: Properties, Characterization, and Imaging*, Waser, R.; Böttger, U.; Tiedke, S., Eds. Wiley-VCH: Weinheim, 2005; pp 53-75.

149. Sawyer, C. B.; Tower, C. H. *Phys. Rev.* **1930,** 35, 269-273.

150. Narendar, Y.; Messing, G. L. *Chem. Mater.* **1997,** 9, 580-587.

151. Nanda, J.; Sapra, S.; Sarma, D. D.; Chandrasekharan, N.; Hodes, G. *Chem. Mater.* **2000,** 12, 1018-1024.

152. Larson, A. C.; Dreele, R. B. V. *Gerneral Structure Analysis System (GSAS)*; Los Alamos National Analysis System: 2004.

153. Toby, B. H. *J. Appl. Crystallogr.* **2001,** 34, 210-21.

154. Brust, M.; Walker, M.; Bethell, D.; Schiffrin, D. J.; Whyman, R. *J. Chem. Soc., Chem. Commun.* **1994,** 7, 801-802.

155. Pan, D.; Zhao, N.; Wang, Q.; Jiang, S.; Ji, X.; An, L. *Adv. Mater.* **2005,** 17, 1991-1995.

156. Doeuff, S.; Henry, M.; Sanchez, C.; Livage, J. *J. Non-Cryst. Solids* **1987,** 89, 206-216.

157. Schubert, U.; Arprac, E.; Glaubitt, W.; Helmerich, A.; Chau, C. *Chem. Mater.* **1992,** 4, 291-295.

158. Aronoff, Y. G.; Chen, B.; Lu, G.; Seto, C.; Schwartz, J.; Bernasek, S. L. *J. Am. Chem. Soc.* **1997,** 119, 259-262.

159. Max, J. J.; Chapados, C. *J. Phys. Chem. A* **2004,** 108, 3324-3337.

160. Yin, J. S.; Wang, Z. L. *Phys. Rev. Lett.* **1997,** 79, 2570-2573.

161. Sanchez, C.; Livage, J.; Henry, M.; Babonneau, F. *J. Non-Cryst. Solids* **1988,** 100, 65-76.

162. Dunuwila, D. D.; Gagliardi, C. D.; Berglund, K. A. *Chem. Mater.* **1994,** 6, 1556-1562.

163. Zhang, Z.; Shao, X.; Yu, H.; Wang, Y.; Han, M. *Chem. Mater.* **2005,** 17, 332-336.

164. Lisoni, J. G.; Millán, P.; Vila, E.; Vidales, J. L. M. d.; Hoffmann, T.; Castro, A. *Chem. Mater.* **2001,** 13, 2084-2091.

165. Hervoches, C. H.; Lightfoot, P. *Chem. Mater.* **1999,** 11, 3359-3364.

166. Chon, U.; Shim, J. S.; Jang, H. M. *J. Appl. Phys.* **2003,** 93, 4769-4775.

167. Garg, A.; Barber, Z. H.; Dawber, M.; Scott, J. F.; Snedden, A.; Lightfoot, P. *Appl. Phys. Lett.* **2003,** 83, 2414-2416.

168. Jeon, M. K.; Kim, Y. I.; Nahm, S. H.; Woo, S. I. *J. Phys. Chem. B* **2005,** 109, 968-972.

169. Shannon, R. *Acta Crystallogr., Section A* **1976,** 32, 751-767.

170. Sasaki, A.; Chiba, T.; Mamiya, Y.; Otsuki, E. *Jpn. J. Appl. Phys.* **1999,** 38, 5564–5567.

171. Takenaka, T.; Maruyama, K.-i.; Sakata, K. *Jpn. J. Appl. Phys.* **1991,** 30, 2236-2239.

172. Babooram, K.; Ye, Z.-G. *Chem. Mater.* **2006,** 18, 532-540.

173. Phintilie, L.; Alexe, M. *J. Appl. Phys.* **2005,** 98, 124103-8.

174. Evans, J. T.; Bullington, J. A. In *A ferroelectric capacitor simulation model*, IEEE 7th International Symposium on Applications of Ferroelectrics, 1990; pp 692-697.

175. Azurmendi, N.; Caro, I.; Caballero, A. C.; Jardiel, T.; Villegas, M. *J. Am. Ceram. Soc.* **2006,** 89, 1232-1236.

176. Kim, S. K.; Miyayama, M.; Yanagida, H. *Mater. Res. Bull.* **1996,** 31, 121-131.

177. Chen, M.; Liu, Z. L.; Wang, Y.; Wang, C. C.; Yang, X. S.; Yao, K. L. *Physica B: Condens. Matter* **2004,** 352, 61-65.

178. Sedlar, M.; Sayer, M. *Ceram. Int.* **1996,** 22, 241-247.

179. Du, H.; Wohlrab, S.; Kaskel, S. *J. Phys. Chem. C* **2007,** 111, 11095-11103.

180. Chang, T.-L.; Lin, W.-T. *Appl. Sur. Sci.* **2005,** 245, 376-383.

181. Hardy, A.; D'Haen, J.; Goux, L.; Wouters, D. J.; Van Bael, M. K.; Van den Rul, H.; Mullens, J. *Chem. Mater.* **2007,** 19, 2994-3001.

182. Hong, S. H.; Horn, J. A.; Trolier-McKinstry, S.; Messing, G. L. *J. Mater. Sci. Lett.* **2000,** 19, 1661-1664.

183. Zhou, Z.; Dong, X.; Chen, H.; Yan, H. *J. Am. Ceram. Soc.* **2006,** 85, 1756-1760.

184. Shimanskij, A. F.; Drofenik, M.; Kolar, D. *J. Mater. Sci.* **1994,** 29, 6301-6305.

185. Hwang, H.-i.; Park, J.-s.; Auh, K.-h., *Ceramic Transactions*. Am. Ceram. Soc.: Westerville, 1998; Vol. 100, p 267-276.

186. Ezhilvalavan, S.; Xue, J. M.; Wang, J. *J. Phys. D: Appl. Phys.* **2002,** 35, 2254-2259.

187. Meyer, R.; Waser, R.; Prume, K.; Schmitz, T.; Tiedke, S. *Appl. Phys. Lett.* **2005,** 86, 142907-3.

188. Lee, J.-S.; Joo, S.-K. *Appl. Phys. Lett.* **2002,** 81, 2602-2604.

List of Symbols

Symbols	Meaning	SI Unit
A	Area	meter^2
C	Capacitance	farad
d	Thickness	meter
d_{ijk}	Piezoelectric charge (or strain) coefficient	meter·volt^{-1} = coulomb·newton^{-1}
D	Electric displacement	coulomb·meter^{-2}
E	Electric field	volt·meter^{-1}
E_c	Coercive field	volt·meter^{-1}
E_{dep}	Depolarization field	volt·meter^{-1}
E_{max}	Maximum electric field	volt·meter^{-1}
ε_0	Dielectric permittivity of vacuum	farad·meter^{-1}
ε_r	Relative dielectric constant	
ε_{fe}	Small signal ε_r of a ferroelectric[a]	
i	Current	ampere
J	Current density	ampere·meter^{-2}
p_i	Pyroelectric coefficient	coulomb· meter^{-2}·kelvin^{-1}
P	Dielectric polarization	coulomb·meter^{-2}
P_{max}	Maximum dielectric polarization	coulomb·meter^{-2}
P_r	Remanent polarization	coulomb·meter^{-2}
P_s	Spontaneous polarization	coulomb·meter^{-2}
Q	Charge	coulomb
Θ	Curie–Weiss temperature	kelvin
R	Electric resistance	ohm
t	Time	second
T	Temperature	kelvin
T_c	Curie point	kelvin
V	Electric voltage	volt
χ	Dielectric susceptibility	

a relative dielectric constant measured at a much smaller electric field compared to that required to switch remanent polarization in a ferroelectric.

Biographic Note

Personal Information

Family name: Du, Given name: Hongchu

Birth: Oct.16, 1976 in Xihua, Henan, China

Nationality: Chinese

Education

Oct.2004 –Feb. 2008

Ph.D. in **Chemistry**, Institute of Inorganic Chemistry, Dresden University of Technology

Sept.2001–Jul.2004

M.Sc. in **Chemical Technology**, Graduate School of Chinese Academy of Sciences, Institute of Process Engineering, Chinese Academy of Sciences

Sept.1995–Jun.1999

B.Sc. in **Material Chemistry**, School of Materials Science and Technology, China University of Geosciences, Beijing

Employment Experience

Jul. 1999–Aug.2001

Research assistant (full time) in Key Laboratory of Rear Earth Chemistry and Physics, Changchun Institute of Applied Chemistry, Chinese Academy of Sciences

Publication List

Peer Reviewed Journal Articles

1. **Du, H**.; Tang, L.; Kaskel, S., "Synthesis, Microstructure, and Ferroelectric Properties of $Bi_{3.25}La_{0.75}Ti_{3-x}M_xO_{12}$ (M = Mo, W, Nb, V) Ceramics", (submitted to *J. Phys. Chem.*)
2. Wohlrab, S.; **Du, H**.; Weiß, M.; Kaskel, S., "Foam-derived multiferroic $BiFeO_3$ nanoparticles and integration into transparent polymer nanocomposites". *J. Exp. Nanoscience* **2008**, 3, 1-15.
3. **Du, H.**; Wohlrab, S.; Weiß, M.; Kaskel, S., "Preparation of $BaTiO_3$ Nanocrystals using a Two Phase Solvothermal Method". *J. Mater. Chem*. 2007, 17, 4605-4610.
4. **Du, H.**; Wohlrab, S.; Kaskel, S., "Synthesis, Structure, and Properties of $Bi_{3.25}Pr_{0.75}Ti_{2.97}V_{0.03}O_{12}$ Ferroelectric Ceramics". *J. Phys. Chem*. C 2007, 111, (29), 11095-11103.
5. **Du, H.**; Wohlrab, S.; Kaskel, S., "Synthesis of Nanostructured Bismuth Titanate Microspheres". *J. Nanosci. Nanotechnol*. 2006, 6, (7), 2110-2116.
6. Wohlrab, S.; Weiss, M.; **Du, H.**; Kaskel, S., "Synthesis of $MNbO_3$ Nanoparticles (M = Li, Na, K)". *Chem. Mater*. 2006, 18, (18), 4227-4230.
7. **Du, H.**; Yuan, F.; Huang, S.; Li, J.; Zhu, Y., "A new reaction to ZnO nanoparticles". *Chem. Lett*. 2004, 33, (6), 770-771.

B. Patents

1. Kaskel, S.; Wohlrab, S.; **Du, H.** (2006): Transparente, ferroelektrische Nanopartikel enthaltende Polymerkomposite und Dispersionen, Verfahren zur Herstellung und Verwendung. German Patent, No. DE102006046078A1 dated 09.22.2006.
2. 朱永法, **杜红初**, 田 野. (2003): 油分散性二硫化钼的制备方法. 中国专利, CN03148389.5 日期 2003-07-02. [Zhu, Y.; **Du, H.**; Tian, Y. (2003): A Preparation Method for Oil Dispersible Molybdenum Disulfide. Chinese Patent, No. CN03148389.5 dated 07.02.2003.]
3. **杜红初**,袁方利,黄淑兰,李晋林. (2003): 一种纳米氧化锌的制备方法. 中国专利, CN03146588.9 日期 2003-07-08.[**Du, H.**; Yuan, F.; Huang, S.; Li, J. (2003): A Preparation Method for Zinc Oxide Nanoparticles. Chinese Patent, No. CN03146588.9 dated 2003-07-08.]

A1, **A3–5** and **B1** have partially evolved from this dissertation.

Versicherung

Hiermit versichere ich, dass ich die vorliegende Arbeir ohne unzulässige Hilfe Dritter und ohne Benutzung anderer als der angegebenen Hilfsmittel angefertigt habe; die aus fremden Quellen direkt oder indirekt übernommenen Gedanken sind als solche kenntlich gemacht. Die Arbeit wurde bisher weder im Inland noch im Ausland in gleicher oder ähnlicher Form einer anderen Prüfungsbehörde vorgelegt.

Die vorliegende Arbeit wurde am Institut für Anorganische Chemie der Techinische Universität Dresden unter wissenschaftlichen Betreung von Herrn Prof. Dr. Stefan Kaskel im zeitraum von Oktober 2004 bis September 2007 angefertigt.

Dresden, den 22.11.2007 Hongchu Du